Master's Thesis

Óscar Martínez Medina

Finite element model verification of a Compression-After-Impact test device for thin-walled composite plates

Óscar Martínez Medina

Finite element model verification of a Compression-After-Impact test device for thin-walled composite plates

Masterarbeit eingereicht im Rahmen der Masterprüfung

im Studiengang Flugzeugbau
am Department Fahrzeugtechnik und Flugzeugbau
der Fakultät Technik und Informatik
der Hochschule für Angewandte Wissenschaften Hamburg

Erstprüfer/in: Prof. Dr.-Ing. Dipl.-Kfm. Markus Linke
Zweitprüfer/in : Prof. Dr.-Ing. Jens Baaran

Abgabedatum: 16.09.2019

Zusammenfassung

Óscar Martínez Medina

Thema der Bachelorthesis
Finite-Elemente-Modellüberprüfung einer Compression-After-Impact Prüfvorrichtung für dünnwandige Compositplatten

Stichworte

Finite-Elemente-Modellierung, dünnwandige Platten, Verbundwerkstoff, Kompressions-Nachschlag-Gerät, Verifikation, implizites Verfahren, freie Gleitkante, seitliche Abstützungen, Verbinder, Reibung

Kurzzusammenfassung

Diese Masterarbeit verifiziert ein Finite-Elemente-Modell eines CAI-Testgeräts für dünnwandige kohlefaserverstärkte Kunststoffplatten. Simulationen werden vom einfachsten bis zum komplexesten Finite-Elemente-Modell berechnet. Um die Unterschiede zwischen den einzelnen Modellen zu analysieren, werden bei einem CAI-Test die wichtigsten Merkmale der Probe ermittelt. Darüber hinaus wird auch der Einfluss der einfach abgestützten Kanten des CAI-Testgeräts auf den Spannungszustand innerhalb der dünnwandigen Platte untersucht.

Óscar Martínez Medina

Title of the paper
Finite element model verification of a Compression-After-Impact test device for thin-walled composite plates

Keywords
Finite Element Modeling, thin-walled plates, composite material, Compression-After-Impact device, verification, implicit procedure, free sliding edge, lateral supports, connectors, friction

Abstract

This master thesis verify a finite element model from a CAI test device, for thin-walled carbon fiber reinforced plastic panels. Simulation are computed from the simplest finite element model to the most complex one. In order to analyze the differences between each model, main characteristics from the specimen are obtained, when it is under a CAI test. Furthermore, influence of the simply supported edges of the CAI test device on the stress state within the thin-walled plate is also studied.

Acknowledgements

First, I would like to express my gratitude to Universitat Politècnica de València (UPV) for its excellent Msc degree program that I received in Spain. In addition, UPV gave me the opportunity to live this fantastic experience writing my final Msc thesis abroad, in an amazing city like Hamburg.

Moreover, I am so grateful to have had Prof. Dr.-Ing. Dipl.-Kfm. Markus Linke as supervisor for my thesis. Mr. Markus Linke has shown me his professionalism and his great way of being. I also want to mention to Aurelio José Olivares Ferrer, a PhD student who works in the Department of Vehicle Technology and Aircraft Construction together with Prof. Linke. Aurelio offered me essential advised and technical help during my Msc thesis at HAW Hamburg, I am sure that this thesis it would not be as successful as it is without his help.

Finally, I would like acknowledge to my brother Ángel, and my parents Ángel and Fina, for their unconditional love and for their emotional and economic support that, all of them, offered me during my time in Hamburg writing this thesis.

CONTENTS

LIST OF FIGURES

LIST OF TABLES

LIST OF SYMBOLS

Acronym	Naming
CAI	Compression-After-Impact test
CFRP	Carbon Fiber Reinforced Polymer
BVID	Barely Visible Impact Damage
FE-Model	Finite Element Model
FEM	Finite Element Method
CAD	Computer-Aided Design
CLT	Classical Laminate Theory
W	Woven
UD	Unidirectional
LSs	Lateral Supports from CAI test device frame
DoF	Degrees of freedom
CKST	Classical Kirchhoff Shell Theory
OoP	Out-of-plane
C	Contact
NC	Non-Contact
HSN	Hashin

Symbols	Unit	Naming
x, y, z	[m]	Laminate global coordinate system
u, v, w	[m]	Laminate global displacements
u^0, v^0, w^0	[m]	Laminate mid-surface plane displacement
ε_x	[-]	Strain in the laminate principal direction
ε_y	[-]	Strain in the laminate transverse direction
ε_z	[-]	Strain in the laminate through-thickness direction
γ_{xy}	[-]	In-plane shear strain in the laminate orientation
γ_{xz}	[-]	Out-of-plane shear strain in the laminate principal direction
γ_{yz}	[-]	Out-of-plane shear strain in the laminate transverse direction
t	[mm]	Plate thickness
a	[mm]	Length of the sample plate
b	[mm]	Width of the sample plate
σ_x	[Pa]	Stress in the laminate principal direction
σ_y	[Pa]	Stress in the laminate transverse direction
σ_z	[Pa]	Stress in the laminate through-thickness direction
τ_{xy}	[Pa]	In-plane shear stress in the laminate orientation
τ_{xz}	[Pa]	Out-of-plane shear stress in the laminate principal direction
τ_{yz}	[Pa]	Out-of-plane shear stress in the laminate transverse direction
Φ_k	[º]	Oriented reference system of each ply
K_x, K_y, K_{xy}	[m^{-1}]	Middle surface curvatures of laminates
$\{\varepsilon^0\}$	[-]	Deformations of the middle surface
$\{\bar{\varepsilon}\}$	[-]	Strains in the ply reference system
$\{\bar{\sigma}\}$	[Pa]	Stresses in the ply reference system
$\{N\}$	[N/m]	Membrane forces
$\{M\}$	[N]	Momentums
$[A], [B], [D]$	[-]	Stiffness matrices of the laminate
$[\bar{Q}]_k$	[Pa]	Stiffness matrix of ply k in the ply reference system
$[T]_k$	[-]	Rotational matrix of ply k
$[S]_k$	[N^{-1} m^2]	Flexibility matrix of ply k
$[R]$	[-]	Reuter matrix

$\varepsilon_1, \varepsilon_2, \varepsilon_3$	[-]	Strains in the ply local coordinate system
σ_1, σ_2	[Pa]	Stresses in the ply local coordinate system
τ_{12}	[Pa]	In-plane shear stress in the ply orientation
τ_{13}	[Pa]	Out-of-plane shear stress in the ply principal direction
τ_{23}	[Pa]	Out-of-plane shear stress in the ply transverse direction
γ_{12}	[-]	In-plane shear strain in the ply orientation
γ_{13}	[-]	Out-of-plane shear strain in the ply principal direction
γ_{23}	[-]	Out-of-plane shear strain in the ply transverse direction
$\{\hat{\sigma}\}$	[Pa]	Effective stress tensor
$\hat{\sigma}_{11}, \hat{\sigma}_{22}, \hat{\tau}_{12}$	[Pa]	Components from the effective stress tensor
α	[-]	Hashin damage model parameter
X^T	[Pa]	Ply tensile strength in the fiber direction
X^C	[Pa]	Ply compression strength in the fiber direction
Y^T	[Pa]	Ply tensile strength in the transverse direction
Y^C	[Pa]	Ply compression strength in the transverse direction
S^L	[Pa]	Ply compression strength in the transverse direction
S^T	[Pa]	Ply tensile strength in the transverse direction
[M]	[-]	Damage operator. Hashin's theory
μ	[-]	Friction coefficient between two surfaces
F_c	[N]	Coulomb friction force
$\dot{\gamma}_i$	[-]	Slip rate in direction i
E_{1f}	[Pa]	Elastic modulus of fiber material in the fiber direction
E_{2f}	[Pa]	Elastic modulus of fiber material in the transverse direction
ρ	[kg/m^3]	Density of a ply
ρ_f	[kg/m^3]	Density of the fiber material
$\nu_{12,f}$	[-]	In-plane Poisson's ratio of fiber material
$G_{12,f}$	[Pa]	In-plane shear modulus of fiber material
$\sigma_{f,F}$	[Pa]	Failure stress of the fiber material in the fiber direction
E_m	[Pa]	Elastic modulus of matrix material
ρ_m	[kg/m^3]	Density of the matrix material
ν_m	[-]	Poisson's ratio of matrix material
G_m	[Pa]	Shear modulus of matrix material

$V_{f,UD}$	[-]	Fiber volume ratio of unidirectional plies
$V_{f,W}$	[-]	Fiber volume ratio of woven plies
E_1	[Pa]	Elastic modulus in the ply direction
E_2	[Pa]	Elastic modulus in the ply transverse direction
ν_{12}	[-]	In-plane Poisson's ratio in the ply orientation
G_{12}	[Pa]	In-plane shear modulus of fiber material
G_{13}	[Pa]	OoP shear modulus of fiber material. Longitudinal direction
G_{23}	[Pa]	OoP shear modulus of fiber material. Transverse direction
σ_{plate}	[Pa]	Failure stress of the CAI test
σ_{11}	[Pa]	Uniaxial stress in the length direction of the plate

1. INTRODUCTION

1.1.   Initial situation

Composite materials are widely used around the world. Higher stiffness, resistance and lightness were sought using composite materials for decades in this industry [1]. They are typically used in aerospace and automotive industry. A good example is the aircraft model A350-900 XWB that is composed by 53% of composite materials. In particular, CFRP play an essential role in those industries. Carbon fiber is commonly used to reinforce composite materials to produce higher stiffness and lightweight. Once bound with a polymer (such as epoxy) carbon fiber creates a composite. Properties of the carbon fiber composite are affected by the carbon fiber reinforcement, the polymer resin matrix that binds the carbon fiber together, and any additives introduced to the resin [2].

When composites are used in those industries named above, they can be subjected during their lifetime to various impacts resulting of circumstances such as dropped tools, handling accidents or hail impacts. Furthermore, these materials are sensitive to impact loads [3], as they absorb impact energy mainly through fracture behavior, rather than elasticity and plasticity. Knowledge about damage initiation and propagation in layered carbon/epoxy structures, usually called Barely Visible Impact Damage (BVID) is therefore a major subject of interest for many years in aerospace industry [4]. In some low-energy impact cases, damage is hardly visible on the surface, but more severe damage may still exist underneath. Therefore, different kinds of non-destructive testing (NDT) techniques have been adopted [5].

Due to the damages caused by low speed impacts [3], composites can present a significant decrease in its mechanical properties. For a composite component, this strength reduction has to be considered during the design, in order to establish a secure range of material damage tolerance.

For this reason, Compression-After-Impact (CAI) tests are carried out. This test is valid for multidirectional continuous fiber reinforced composite laminates which are symmetric and balanced with respect to the test direction [6]. A uniaxial compression test is performed using a balanced, symmetric laminated plate, which has been damaged and inspected prior to the application of compressive force. The thickness of the specimen plays an important role in the test, its values has to be in the range of 4-6 mm, otherwise the results obtained from the standard CAI test are invalid and they can generate wrong range of failure. It is even more important for non-damaged and thin specimens because, in the frame of the device are located free sliding edges on the lateral sides of the samples and, the influence of those, has to be consider because they can produce the rupture of the plate. However, the adequate results are reached when the rupture appears because of the compression displacement that occurs during the test performance. In this case, the results would not be valid because, they do not represent the real compression resistance that the specimen has. However, it does not occur in the case of the CAI modified frame [7], the influence of the free sliding edge on CAI testing of thin-walled undamaged composite plates was reduced.

1.2.   Problem description and objectives

The aim of this master thesis is to verify a FE-model of a Compression-After-Impact test device, combining the new version of lateral supports developed at HAW Hamburg lightweight laboratory [7], with the old version width plate (see CAD sketches in chapter 3. FE-Model build up).

Model veification will be carried out with finite elements simulations using Abaqus/CAE (Dassault Systemes, Vélizy-Villacoublay, France) as a software. For this verification, the computations will be focused on the influence of the LSs from the frame of a CAI device when they are in contact with the specimen while compression test is carried out [8] (apart from others main measured parameters such as failure stress). For this reason, parameters such as friction coefficient between both surfaces will be considered.

This influence is important because where is produced the plate rupture depends mainly on the free sliding edge where the LSs are located. The model verification has especial interests specially to predict future experimental test results with a similar frame of the CAI test device.

Furthermore, composite material samples are composed by carbon fiber with epoxy as a matrix, which are used to compute their damage evolution and failure.

Finally, to validate the FE-model, the differences in the damage results from the models computed in Abaqus, using the new frame version of the CAI test device, will be analyzed.

1.3.   Thesis structure and solution strategy

This Master Thesis is divided in five sections. Follows the Introduction, section 2 is composed by the theoretical framework that is behind all the simulations. However, in the case of section 3, the CAD and FE model build up is described passing through all the models created along the thesis. Furthermore, results obtained from each simulation will be analyzed in section 4 presenting from the simplest FE model to the most complex one in order to verify them. Finally, a brief conclusion and an explanation about the work that would be interesting to carry out in the future in this topic will be found in section 5.

The strategy adopted to verify the FE-model follows the next steps:

1. Analyze characteristic parameters from the CAI test.

    ➢ Failure stress of the CAI test
    ➢ Shortening of the specimen
    ➢ OoP deflection of the specimen
    ➢ Uniaxial stress in the length direction of the plate
    ➢ Specimen damage
    ➢ Reaction force distribution on the sliding edge of the specimen (caused by the contact between specimen and LSs)

2. Evaluate those parameter for different FE-models (from the simplest to the most complex model)

   ➢ 2D sample plate
   ➢ 3D sample plate
   ➢ CAI device assembly using a 2D plate as a specimen
   ➢ CAI device assembly using a 3D plate as a specimen
   ➢ CAI device assembly using a 3D plate considering friction behavior between specimen and LSs
   ➢ CAI device assembly with a 3D sample plate model, taking into account the influence of the LSs screws (modeled as connector elements)

2. STATE OF ART

Along this section, typical standard CAI test device will be described, as well as the theoretical framework used in this thesis.

Furthermore, in order to define the main mechanical properties of a laminate, the Classical Laminate Theory (CLT) is presented. It is important to introduce that, to analyze the composite material failure, Hashin's criteria is selected to carry out the computations. The reason why this failure criterion is adopted for this thesis is because, its algorithm, Abaqus can offer a large variety of outputs data from this failure criteria. Furthermore, Hashin's theory will be described along this chapter (Subchapter 2.3). It is also relevant to study the laminate interface to notice if delaminations occur.

In addition, to analyze the influence of the lateral supports (from the CAI test device), a theoretical contact model approach and friction theories between two bodies (applied in *Abaqus Standard*) are described.

Finally, with regard to FEM computations, an explanation about finite element procedures is also included.

2.1.   Compression-After-Impact

The measuring principle involves pre-damaging a test plate, which was tested previously using ultrasound to detect existing delaminations or imperfections [1], and then measuring the residual strength by means of a compression test as it is shown in *Figure 1*:

a) Impact test configuration   b) Non-destructive testing and   c) Compression test
                                     dent depth measurement
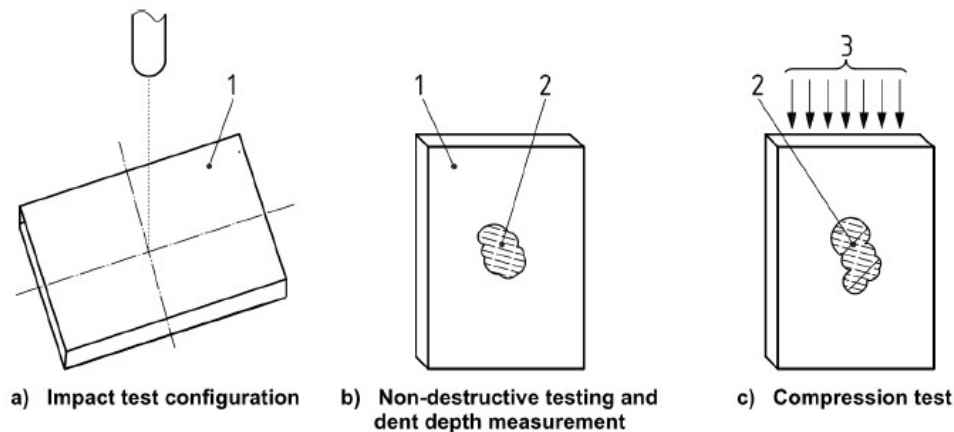
Figure 1. Process of the compression-after-impact test (e.g., standards [6])

To quantify the impact damaged in a composite plate, there are several standardized test methods [6], in which the residual compressive strength is measured. Several characteristic from the standard device are presented as follows:

- ➢ Specimen dimensions are 150 mm x 100 mm (length x width)
- ➢ Specimen thickness between 4 to 6 mm
- ➢ Maximum compression load is limited to 250 kN
- ➢ Frame of the device composed by stainless steel
- ➢ Applicability in a wide range of temperatures (-70 to 300 °C)

They are classified in two groups with regards to the type of frame used in the CAI test:

- o **Frame for ISO 18352 [32], Airbus AITM 1-0010 [25], EN 6038 [33]:** The upper and lower ends of the specimen are clamped. The sides are simply supported with linear contact.

Figure 2. CAI test device from Zwick/Roell GmbH company according to ISO, Airbus, EN [35]

- o **Frame for ASTM D 7137 [6], Boeing BSS 7260 [42], DIN 65561 [34], SACMA SRM 2R-94 [26]:** All four sides are simply supported. The fixture base and load plates are applied directly to the ends of the specimen.
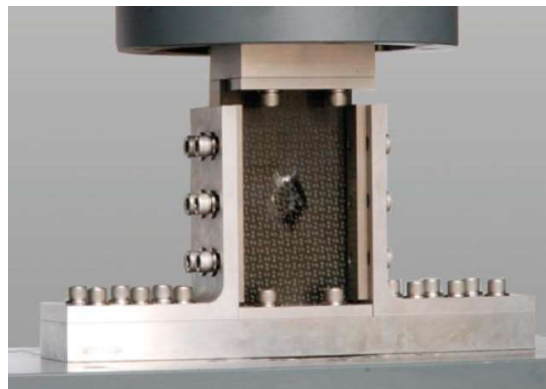
Figure 3. CAI test device from Zwick/Roell GmbH company according to ASTM, Boeing, DIN, SACMA [36]

To obtain a reliable design and maintenance of any composite structure, it is a priority a better understanding of the composite materials behavior under compression pressure when they suffer an impact, even if it is with low speed.

In order to visualize how the acceptable plate failure modes for CAI tests are, *Figure 4* below shows several modes, which can be combined with minor end crushing at a point along the compressively loaded edges of the specimen. In the case the end crushing is sufficiently notable or important, the test won't be acceptable. In addition, CAI test is only carried out when there is non-excessive bending on the plate.
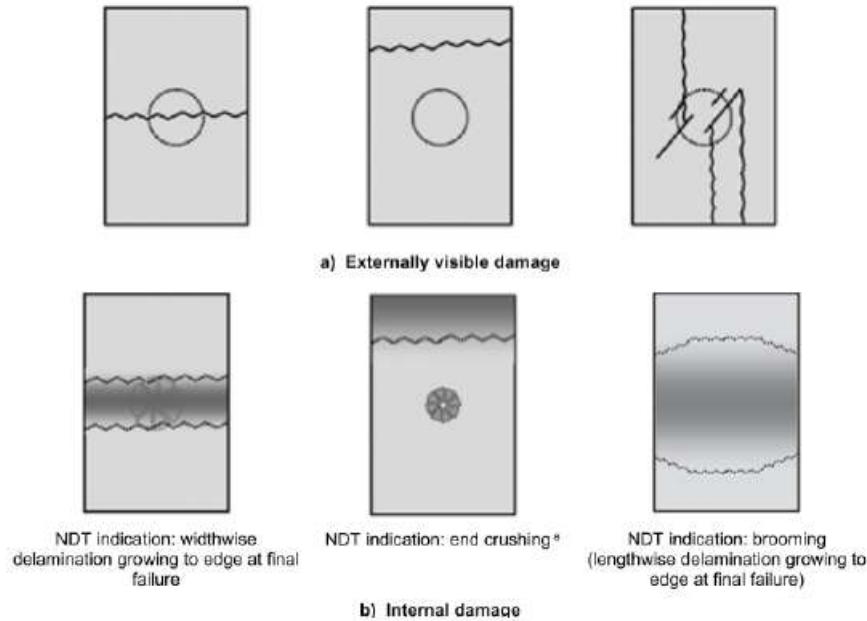
Figure 4. Acceptable failure modes examples in compression-after-impact tests [32]

The laminate thickness plays a key role in this test because stability issues and large stresses appear if the specimen is thin (thickness less than 4 mm approximately). Global buckling occurs before the failure load and, because of that, stresses concentration takes part in the sample plate. The high stress values are induced by the upper clamp causing end crushing and the failure load value is reached sooner that it was expected. Hence, a new test device frame was developed at HAW Hamburg lightweight laboratory [7], those crushing are avoided and thin specimens reach coherent results when this new CAI frame version is used.

2.2. Classical Laminate Theory

It is the simplest model can be studied and it has several limitations when it is applied. However, CLT reaches stiffness and mechanical resistance tendencies correctly. Through this theory [2], it is possible to study different plies orientations in a laminate. The classical laminate theory is a direct extension of the classical plate theory for isotropic and homogeneous material as proposed by Kirchhoff –Love. Nevertheless, the extension of this theory to laminates requires some modifications to take into account the inhomogeneity in thickness direction.

The assumptions this theory adopts are:

- Materials homogeneous and transversely isotropic.

- The in-plane strains ε_x, ε_y, and γ_{xy}, are small compared with the unity (each ply responds to the lineal Hooke's law).

- The displacements u, v, and w are small compared to the plate thickness (ensure linearity). Tangential displacements u and v are linear functions of the z coordinate.

- The plate is an orthotropic laminate perfectly bonded together with an infinitesimal interfaces (continuum displacements through the thickness).

- The plate thickness (t), is constant and much smaller than the plate edges (a and b).

- The laminates are in a state of plane stress ($\sigma_z = 0$).

- The transverse normal strain ε_z is negligible.

- Any straight line normal to the laminate middle surface remains straight. Therefore, transverse shear strains γ_{xz} and γ_{yz} are negligible. This is valid for pure bending or lengths greater than 10 times the laminate thickness.

- Transverse shear stresses τ_{xz} and τ_{yz} vanish on the plate surfaces defined by $z = \pm\, t/2$.

The last two hypotheses constitute the Kirchoff's hypothesis.

2.2.1. Problem description

In order to illustrate the terminology from the list of symbols, *Figure 5* is presented as follows:
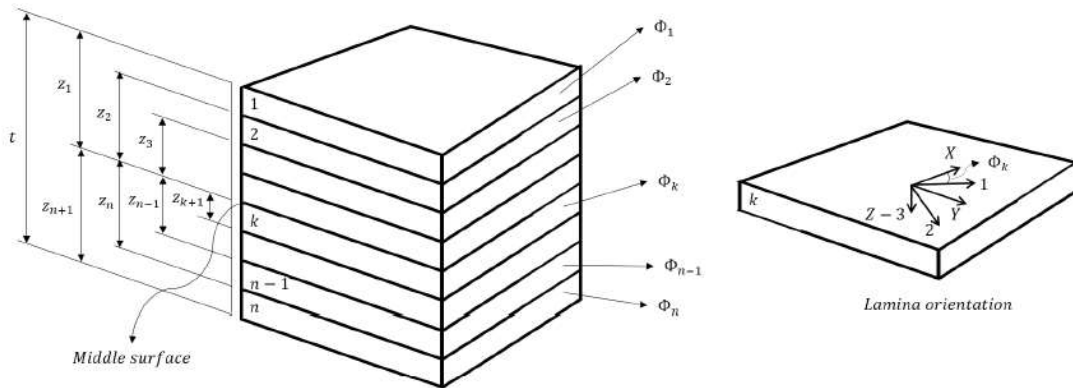
Figure 5. Laminated plate geometry and layer numbering system. Coordinate system of the laminas [2]

2.2.2. Strain-Displacement relations

The deformations and the notations, used in the case of the classical laminate theory, are illustrated in *Figure 6*.
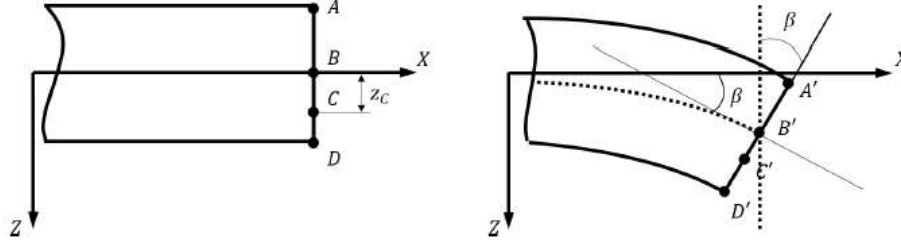
Figure 6. Representation of plate deformation in the case of the classical laminate theory [2]

As it was mentioned in the CLT assumptions, w is not dependent to z and ABCD line is transformed in A'B'C'D':

$$w(x,y) = w^0(x,y) \tag{1}$$

Furthermore, x displacement is a straight line, hence:

$$u(x,y,z_c) = u^0(x,y) - z_c \sin\beta \tag{2}$$

In addition, small displacements hypothesis is taking into account:

$$\sin\beta \cong \tan\beta = \frac{\partial w^0}{\partial x} \tag{3}$$

And, the x e y displacement are:

$$u(x,y,z) = u^0(x,y) - z\frac{\partial w^0}{\partial x} \tag{4}$$

$$v(x,y,z) = v^0(x,y) - z\frac{\partial w^0}{\partial y} \tag{5}$$

Moreover, it is possible to relate displacements with deformations applying Cauchy equations:

$$\varepsilon_x = \frac{\partial u}{\partial x} \qquad \varepsilon_y = \frac{\partial v}{\partial y} \qquad \gamma_{xy} = \frac{\partial v}{\partial x} + \frac{\partial u}{\partial y} \qquad [6] \quad [7] \quad [8]$$

Replacing:

$$\varepsilon_x = \frac{\partial u^0}{\partial x} - z\frac{\partial^2 w^0}{\partial x^2} = \varepsilon_x^0 - z\frac{\partial^2 w^0}{\partial x^2} \tag{9}$$

$$\varepsilon_y = \frac{\partial v^0}{\partial y} - z\frac{\partial^2 w^0}{\partial y^2} = \varepsilon_y^0 - z\frac{\partial^2 w^0}{\partial y^2} \tag{10}$$

$$\gamma_{xy} = \frac{\partial v^0}{\partial x} + \frac{\partial u^0}{\partial y} - 2z\frac{\partial^2 w^0}{\partial x\partial y} = \gamma_{xy}^0 - 2z\frac{\partial^2 w^0}{\partial x\partial y} \tag{11}$$

Rewriting those parameters in matrix structure and denominating the mid-plane curvatures as K_x, K_y, K_{xy}:

$$\begin{Bmatrix} \varepsilon_x \\ \varepsilon_y \\ \gamma_{xy} \end{Bmatrix} = \begin{Bmatrix} 0 \\ \varepsilon_x \\ 0 \\ \varepsilon_y \\ 0 \\ \gamma_{xy} \end{Bmatrix} + z \begin{Bmatrix} K_x \\ K_y \\ K_{xy} \end{Bmatrix} \qquad \begin{Bmatrix} K_x \\ K_y \\ K_{xy} \end{Bmatrix} = \begin{Bmatrix} -\dfrac{\partial^2 w^0}{\partial x^2} \\[6pt] -\dfrac{\partial^2 w^0}{\partial y^2} \\[6pt] -2\dfrac{\partial^2 w^0}{\partial x \partial y} \end{Bmatrix} \qquad \text{[12] [13] [14]}$$

Expression simplify:

$$\{\bar{\varepsilon}\} = \{\varepsilon^0\} + z\{K\} \qquad \text{[15]}$$

2.2.3. Definitions of Stress and Moment Resultant

Once the expression below is reached, can be presented as follows:

$$\{\bar{\sigma}\} = [\bar{Q}]\{\bar{\varepsilon}\} = [\bar{Q}](\{\varepsilon^0\} + z\{K\}) \qquad \text{[16]}$$

In the composite laminated plate analysis by static equilibrium equations, the forces and moments resultants per unit length are given as:

$$\left(N_x, N_y, N_{xy}\right) = \int_{-t/2}^{t/2} \left(\sigma_x^k, \sigma_y^k, \tau_{xy}^k\right) dz \qquad \text{[17]}$$

$$\left(M_x, M_y, M_{xy}\right) = \int_{-t/2}^{t/2} \left(\sigma_x^k, \sigma_y^k, \tau_{xy}^k\right) z\, dz \qquad \text{[18]}$$
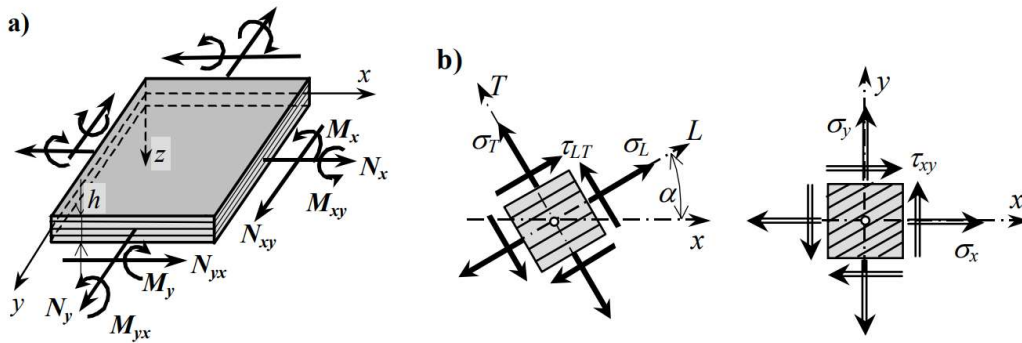
Figure 7. a) Definition of in-force and moment resultants for a plate, b) Stress components in lamina respect to the lamina principal (L, T)-axes and the laminated plate (x, y)-coordinate system [39]

With matrix notation:

$$\{N\} = \begin{Bmatrix} N_x \\ N_y \\ N_{xy} \end{Bmatrix} = \int_{-t/2}^{t/2} \{\bar{\sigma}\}\, dz = \sum_{k=1}^{n} \int_{z_k}^{z_{k+1}} \{\bar{\sigma}\}\, dz \qquad [19]$$

$$\{M\} = \begin{Bmatrix} M_x \\ M_y \\ M_{xy} \end{Bmatrix} = \int_{-t/2}^{t/2} \{\bar{\sigma}\}\, z\, dz = \sum_{k=1}^{n} \int_{z_k}^{z_{k+1}} \{\bar{\sigma}\}\, z\, dz \qquad [20]$$

Replacing stresses:

$$\{N\} = \sum_{k=1}^{n} [\bar{Q}]_k \left[\int_{z_k}^{z_{k+1}} \{\varepsilon^0\}\, dz + \int_{z_k}^{z_{k+1}} z\, \{K\}\, dz \right] \qquad [21]$$

$$\{M\} = \sum_{k=1}^{n} [\bar{Q}]_k \left[\int_{z_k}^{z_{k+1}} \{\varepsilon^0\}\, z\, dz + \int_{z_k}^{z_{k+1}} z^2\, \{K\}\, dz \right] \qquad [22]$$

The equations above can be expressed as:

$$\{N\} = [A]\{\varepsilon^0\} + [B]\{K\} \qquad [23]$$

$$\{M\} = [B]\{\varepsilon^0\} + [D]\{K\} \qquad [24]$$

2.2.4. Laminate stiffness. Matrixes and vectors definition

Matrixes [A], [B] and [D] from last section define the stiffness of the laminate:

$$A_{ij} = \sum_{k=1}^{n} \left[(\bar{Q}_{ij})_k \int_{z_k}^{z_{k+1}} dz \right] = \sum_{k=1}^{n} \left[(\bar{Q}_{ij})_k\, (z_{k+1} - z_k) \right] \qquad [25]$$

$$B_{ij} = \sum_{k=1}^{n} \left[(\bar{Q}_{ij})_k \int_{z_k}^{z_{k+1}} z\, dz \right] = \frac{1}{2} \sum_{k=1}^{n} \left[(\bar{Q}_{ij})_k\, (z_{k+1}^2 - z_k^2) \right] \qquad [26]$$

$$D_{ij} = \sum_{k=1}^{n} \left[(\bar{Q}_{ij})_k \int_{z_k}^{z_{k+1}} z^2\, dz \right] = \frac{1}{3} \sum_{k=1}^{n} \left[(\bar{Q}_{ij})_k\, (z_{k+1}^3 - z_k^3) \right] \qquad [27]$$

Each of the elements computed above are located in the next matrixes:

$$[A] = \begin{bmatrix} A_{11} & A_{12} & A_{16} \\ A_{12} & A_{22} & A_{26} \\ A_{16} & A_{26} & A_{66} \end{bmatrix}$$

[28]

$$[B] = \begin{bmatrix} B_{11} & B_{12} & B_{16} \\ B_{12} & B_{22} & B_{26} \\ B_{16} & B_{26} & B_{66} \end{bmatrix}$$

[29]

$$[D] = \begin{bmatrix} D_{11} & D_{12} & D_{16} \\ D_{12} & D_{22} & D_{26} \\ D_{16} & D_{26} & D_{66} \end{bmatrix}$$

[30]

The A_{ij} are extensional stiffnesses with A_{16} and A_{26} representing shear-extension coupling, the B_{ij} are bending-extension coupling stiffnesses, and the D_{ij} are bending stiffnesses with D_{16} and D_{26} representing bend-twist coupling. The presence of B_{ij} implies coupling between bending and extension of a laminate.

In the case of this thesis, an orthotropic laminate is used, therefore [B] is null in all its elements and several matrix components from matrix [A] and [D] are null too. Null elements from matrix [A] avoid the coupling between lineal and angular in-plane deformations. On the other hand, null elements in [D] matrix ignore the coupling between the bending and torsional deformations.
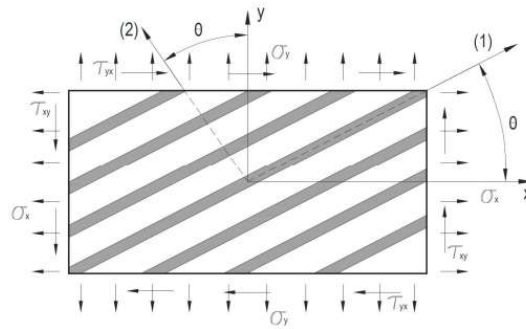
Figure 8. The generally orthotropic lamina [2]

Hence, now appearance of the reduced matrices is:

$$[A] = \begin{bmatrix} A_{11} & A_{12} & 0 \\ A_{12} & A_{22} & 0 \\ 0 & 0 & A_{66} \end{bmatrix}$$

[31]

$$[B] = \begin{bmatrix} 0 & 0 & 0 \\ 0 & 0 & 0 \\ 0 & 0 & 0 \end{bmatrix}$$

[32]

$$[D] = \begin{bmatrix} D_{11} & D_{12} & 0 \\ D_{12} & D_{22} & 0 \\ 0 & 0 & D_{66} \end{bmatrix} \qquad [33]$$

Moreover, it is essential to calculate the strain in the global coordinate system and then, be able to compute the stresses in each ply in their local system.

$$\{\bar{\varepsilon}\}_i = \{\varepsilon^0\} + z_i \{K\} \qquad [34]$$

In addition, in each ply there are stresses which can be divided in two sections, one of them is as follows:

$$\{\bar{\sigma}\}_i = [\bar{Q}]_i \{\bar{\varepsilon}\}_i \qquad [35]$$

$$\{\sigma\}_i = [T]_i \{\bar{\sigma}\}_i \qquad [36]$$

$$\{\varepsilon\}_i = [S]_i \{\sigma\}_i \qquad [37]$$

Where [S] is the flexibility matrix, and the other section is:

$$\{\bar{\sigma}\}_i = [T]_i^{-1} \{\sigma\}_i \qquad [38]$$

$$\{\sigma\}_i = [Q]_i \{\varepsilon\}_i \qquad [39]$$

$$\{\varepsilon\}_i = [R][T]_i[R]^{-1} \{\bar{\varepsilon}\}_i \qquad [40]$$

Finally, the strain and stress tensors, in global (left) and local (right) coordinate system, are presented as:

$$\{\bar{\varepsilon}\}_i = \begin{Bmatrix} \varepsilon_x \\ \varepsilon_y \\ \gamma_{xy} \end{Bmatrix} \qquad \{\varepsilon\}_i = \begin{Bmatrix} \varepsilon_1 \\ \varepsilon_2 \\ \gamma_{12} \end{Bmatrix} \qquad [41] \quad [42]$$

$$\{\bar{\sigma}\}_i = \begin{Bmatrix} \sigma_x \\ \sigma_y \\ \tau_{xy} \end{Bmatrix} \qquad \{\sigma\}_i = \begin{Bmatrix} \sigma_1 \\ \sigma_2 \\ \tau_{12} \end{Bmatrix} \qquad [43] \quad [44]$$

2.3.   Lamina failure criteria: Hashin

The initiation capability of the material damage for fiber-reinforced materials follows the next indications:

a) Requires that the behavior of the undamaged material is linearly elastic.

b) Is based on Hashin's theory (Hashin and Rotem, 1973, and Hashin, 1980)

c) Considers four different failure modes: fiber tension, fiber compression, matrix tension, and matrix compression.

d) Can be used in combination with the damage evolution model.

Damage initiation refers to the onset of degradation at a material point. In Abaqus the damage initiation criteria for fiber-reinforced composites are based on Hashin's theory [18]. These criteria consider four different damage initiation mechanisms: fiber tension, fiber compression, matrix tension, and matrix compression.

The initiation criteria have the following general forms in Abaqus Standard [11]:

Fiber stress ($\hat{\sigma}_{11} \geq 0$):

$$F_f^t = \left(\frac{\hat{\sigma}_{11}}{X^T}\right)^2 + \alpha\left(\frac{\hat{\tau}_{12}}{S^L}\right)^2 \qquad [45]$$

Fiber compression ($\hat{\sigma}_{11} < 0$):

$$F_f^c = \left(\frac{\hat{\sigma}_{11}}{X^C}\right)^2 \qquad [46]$$

Matrix stress ($\hat{\sigma}_{22} \geq 0$)

$$F_m^t = \left(\frac{\hat{\sigma}_{22}}{Y^T}\right)^2 + \left(\frac{\hat{\tau}_{12}}{S^L}\right)^2 \qquad [47]$$

Matrix compression ($\hat{\sigma}_{22} < 0$):

$$F_m^c = \left(\frac{\hat{\sigma}_{22}}{2S^T}\right)^2 + \left[\left(\frac{Y^C}{2S^T}\right)^2 - 1\right]\frac{\hat{\sigma}_{22}}{Y^C} + \left(\frac{\hat{\tau}_{12}}{S^L}\right)^2 \qquad [48]$$

The different parameters in the above equations mean:

X^T: denotes the longitudinal tensile strength

X^C: denotes the longitudinal compressive strength

Y^T: denotes the transverse tensile strength

Y^C: denotes the transverse compressive strength

S^L: denotes the longitudinal shear strength

S^T: denotes the transverse shear strength

α: is a coefficient that determines the contribution of the shear stress to the fiber tensile initiation criterion

$\hat{\sigma}_{11}, \hat{\sigma}_{22}, \hat{\tau}_{12}$: are components of the effective stress tensor, $\hat{\sigma}$, that is used to evaluate the initiation criteria and which is computed from:

$$\{\hat{\sigma}\} = [M]\{\sigma\}$$

[49]

Where $\{\sigma\}$ is the true stress and $[M]$ is the damage operator:

$$[M] = \begin{bmatrix} \dfrac{1}{(1-d_f)} & 0 & 0 \\ 0 & \dfrac{1}{(1-d_m)} & 0 \\ 0 & 0 & \dfrac{1}{(1-d_s)} \end{bmatrix}$$

[50]

d_f, d_m and d_s are internal (damage) variables that characterize fiber, matrix, and shear damage respectively, which are derived from damage variables d_f^t, d_f^c, d_m^t and d_m^c, corresponding to the four modes previously discussed, as follows:

$$d_f = \begin{cases} d_f^t & if \ \hat{\sigma}_{11} \geq 0 \\ d_f^c & if \ \hat{\sigma}_{11} < 0 \end{cases}$$

[51]

$$d_m = \begin{cases} d_m^t & if \ \hat{\sigma}_{22} \geq 0 \\ d_m^c & if \ \hat{\sigma}_{22} < 0 \end{cases}$$

[52]

$$d_s = 1 - (1-d_f^t)(1-d_f^c)(1-d_m^t)(1-d_m^c)$$

[53]

In the case that there is no damage initiation, matrix *[M]* is equal to the identity matrix, hence:

$$\{\hat{\sigma}\} = \{\sigma\}$$

[54]

Once damage initiation and evolution has occurred for at least one mode, the damage operator becomes significant in the criteria for damage initiation of other modes. The effective stress, $\hat{\sigma}$, is intended to represent the stress acting over the damaged area that effectively resists the internal forces.

On the other hand, with regard to post-damage initiation behavior, it is used for cases in which a damage evolution model has been specified. Prior to damage initiation the material is linearly elastic, with the stiffness matrix of a plane stress orthotropic material. Thereafter, the response of the material is computed from:

$$\{\sigma\} = [C_d]\{\varepsilon\}$$

[55]

In *expression 56*, ε is the strain and C_d is the damaged stiffness matrix, which has the form:

$$C_d = \frac{1}{D}\begin{bmatrix} (1-d_f)E_1 & (1-d_f)(1-d_m)v_{21}E_1 & 0 \\ (1-d_f)(1-d_m)v_{12}E_2 & (1-d_m)E_2 & 0 \\ 0 & 0 & (1-d_s)GD \end{bmatrix} \quad [56]$$

Where $D = 1 - \left(1-d_f\right)(1-d_m)v_{12}v_{21}$ [57]

2.4. Interface delamination model

Delamination is one of the most common types of damage in laminated fibre-reinforced composites due to their relatively weak interlaminar strengths. Delamination can form during any moment of the life of the structure: manufacturing, transport, mounting and service.

Delamination modeling is not presented along this project, however, as it was mentioned above, it is a type of damage and, for that reason it is interesting to remark several categories of delamination [29]. Its causes can be differentiated in two categories: the first category includes delamination due to curved sections, such as curved segments, tubular sections, cylinders and spheres, and pressurized containers. In all of these cases, the normal and shear stresses at the interface of two adjacent plies can originate the loss of adhesion and the initiation of an interlaminar crack. The second category includes abrupt changes of section, such as ply drop-offs, unions between stiffeners and thin plates, free edges, and bonded and bolted joints. Furthermore, it is possible to add a third category related to temperature and moisture effects. The difference between the thermal coefficients of matrix and reinforcement results in differential contractions between the plies during the curing process of the laminate. The residual stresses originated by these differential contractions might be a source of delamination. Moreover, delaminations occur between the fiber and the matrix in a laminate composite material, this region is named "interface" and it can be defined as a cohesive element.
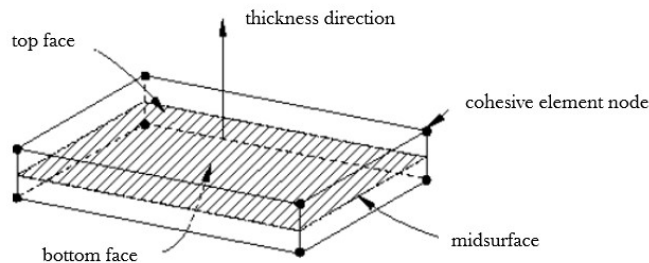
Figure 9. Spatial representation of a three-dimensional cohesive element [11]

The connectivity of cohesive elements follows the same behavior as continuum elements, but it is useful to consider of cohesive elements as being composed of two faces separated by a thickness. The relative motion of the bottom and top faces

measured along the thickness direction represents opening or closing of the interface. The relative change in position of the bottom and top faces measured in the plane orthogonal to the thickness direction quantifies the transverse shear behavior of the cohesive element. Stretching and shearing of the midsurface of the element (the surface halfway between the bottom and top faces) are associated with membrane strains in the cohesive element; however, it is assumed that the cohesive elements do not generate any stresses in a purely membrane response. It is shown in *Figure 10*:
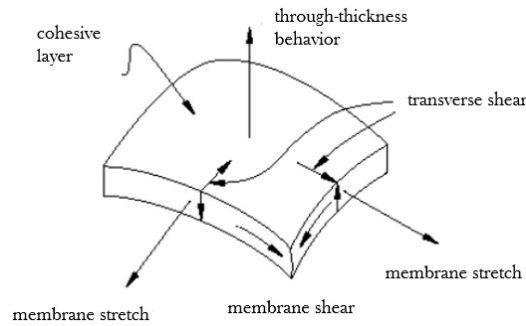
Figure 10.Deformation modes of a cohesive element [11]

In addition, there are two types of delamination to consider: internal delaminations and near-surface delamination [41]. In the case of the internal delamination, it occurs in the inner ply interfaces of the laminate and can be due to the interaction of matrix cracks and ply interfaces. Delaminations originated by transverse matrix cracks in plies orthogonal to the tensile load, are common examples of this type of delamination.
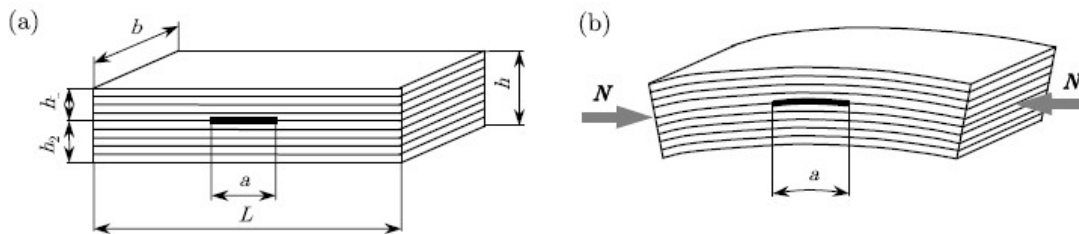
Figure 11. Internal delamination: (a) disposition across the laminate and (b) effect on the overall stability [29]

On the other hand, near-surface delaminations, as the name indicates, originate near the surface of the laminate and represent a more complex scenario than internal delaminations. The deformation of the delaminated part is less influenced by the deformation of the rest of the laminate. Therefore, the deformation of the near-surface delaminated part does not necessary follow the deformation of the rest of the laminate. Consequently, not only the growth of the near-surface delamination has to be taken into account but also its local stability.

2.5.   Theoretical and numerical methods for contacts calculation

Contact concept is notary important along this project because, as in the objectives was mentioned, the aim of this work is focus on the lateral supports influence in the CAI test device and obviously, to reproduce accurately the reality, is a necessity to consider the

contact effect between the lateral supports and the thin laminate plate [8]. When two solid surfaces are loaded together, there will always be some distortion of each of them. Deformations may be purely elastic or may involve some additional plastic, and so permanent, changes in shape. Such deflections and modifications in the surface profiles of the components can be viewed at two different scales (macroscopic scale or microscale). Consider, for example, the contact between a heavily loaded roller and the inner and outer races in a rolling element bearing. The degree of flattening of the rollers can be expressed as a proportion of their radii, at a relatively macroscopic scale. On the other hand, since on the microscale no real surface, such as those of either the roller or the race, can be truly smooth, it follows that when these two solid bodies are pushed into contact they will touch initially at a discrete number of points or asperities. Classical contact mechanics assumes the deforming materials to be isotropic and homogeneous; in principle, its results can be applied both to global contacts and to those between interacting asperities.

With regard to theoretical approaches [37], Hertzian method is useful to compute the contacts between two curved bodies, is based on the following assumptions:

- o   The surfaces are continuous, smooth, nonconforming and frictionless.
- o   The size of the contact area is small compared to the size of the bodies. The strains associated with the deformations are small.
- o   Each solid can be considered to behave as an elastic half-space in the vicinity of the contact zone.
- o   The gap "h" between the undeformed surfaces can be approximated by an expression of the form:

$$h = Ax^2 + By^2 \qquad\qquad [58]$$

where "x" and "y" are orthogonal coordinates lying in the common tangent plane to the two surfaces.

Furthermore, many contact problems will not fall into the preceding categories and require modeling by some numerical means. Common problems of this sort are those that involve friction and partial slip, complex geometry, nonlinearity of elastic properties, or plasticity. For this thesis, finite element method is carried out to reproduce the contact effect. Concerning FEM, the contacting bodies are divided into an array of either two-dimensional axisymmetric or planar elements or three-dimensional brick elements. A set of gap or contact elements is defined between the surface nodes, which are likely to come into contact during loading. Typically, contact problems involve loads distributed over small areas of contact. This results in rapid changes in stress in the elements surrounding the contact. Therefore, the mesh in this region must be refined adequately to describe these high stress gradients.

Abaqus provides several contact formulations. Each formulation is based on a choice of a contact discretization, a tracking approach, and assignment of "master" and "slave" roles to the contact surfaces.

2.5.1. Discretization of contact pair surfaces in Abaqus

Abaqus applies conditional constraints at various locations on interacting surfaces to simulate contact conditions. The locations and conditions of these constraints depend on the contact discretization used in the overall contact formulation. This software offers two contact discretization options: a traditional "node-to-surface" discretization and a true "surface-to-surface" discretization [11].

- Node-to-surface contact discretization:

With traditional node-to-surface discretization the contact conditions are established such that each "slave" node on one side of a contact interface effectively interacts with a point of projection on the "master" surface on the opposite side of the contact interface. Thus, each contact condition involves a single slave node and a group of nearby master nodes from which values are interpolated to the projection point.
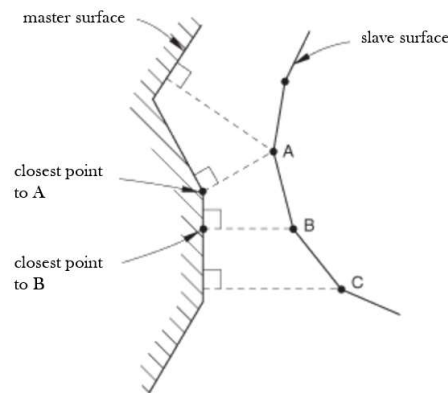
Figure 12. Node-to-surface contact discretization [11]

Traditional node-to-surface discretization has the following characteristics:

- o The slave nodes are constrained not to penetrate into the master surface; however, the nodes of the master surface can, in principle, penetrate into the slave surface.
- o The contact direction is based on the normal of the master surface.
- o The only information needed for the slave surface is the location and surface area associated with each node. The direction of the slave surface normal and slave surface curvature are not relevant. Thus, the slave surface can be defined as a group of nodes.
- o Node-to-surface discretization is available even if a node-based surface is not used in a contact pair definition.

- Surface-to-surface contact discretization

Surface-to-surface discretization considers the shape of both the slave and master surfaces in the region of contact constraints. Surface-to-surface discretization has the following key characteristics:

- o The surface-to-surface formulation enforces contact conditions in an average sense over regions nearby slave nodes rather than only at individual slave nodes. The averaging regions are approximately centered on slave nodes, so each contact constraint will predominantly consider one slave node but will also

consider adjacent slave nodes. Some penetration may be observed at individual nodes. However, large, undetected penetrations of master nodes into the slave surface do not occur with this discretization.

- o The contact direction is based on an average normal of the slave surface in the region surrounding a slave node.
- o Surface-to-surface discretization is not applicable if a node-based surface is used in the contact pair definition.

In general, surface-to-surface discretization provides more accurate stress and pressure results than node-to-surface discretization if the surface geometry is reasonably well represented by the contact surfaces.

Since node-to-surface discretization simply resists penetrations of slave nodes into the master surface, forces tend to concentrate at these slave nodes. This concentration leads to spikes and valleys in the distribution of pressure across the surface. Surface-to-surface discretization resists penetrations in an average sense over finite regions of the slave surface, which has a smoothing effect. As the mesh is refined, the discrepancies between the discretization are reduced, but for a given mesh, refinement the surface-to-surface approach tends to provide stresses that are more accurate.

2.6. Friction calculation theories

Once the contact methods have been described it is interesting to study in which manner friction behavior in the contacts can affect to the bodies involved. When surfaces are in contact, they usually transmit shear as well as normal forces across their interface. There is generally a relationship between these two force components. The relationship, known as the friction between the contacting bodies, is usually expressed in terms of the stresses at the interface of the bodies. The procedure used for friction behavior along this project is based Coulomb model, which is described in subsection below.

2.6.1. Coulomb friction model

It is a common friction model used to describe the interaction of contacting surfaces. The model characterizes the frictional behavior between the surfaces using a coefficient of friction, μ. The Coulomb friction force Fc [38] is a force of constant magnitude, acting in the direction opposite to motion:
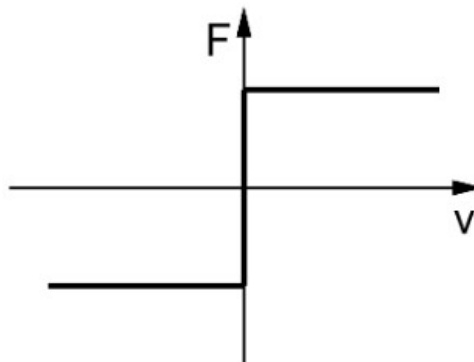
Figure 13. Coulomb friction characteristic [38]

It can be expressed as:

$$F_c = \mu F_N \hspace{6cm} [59]$$

Where F_N is the normal load between two contact surfaces.

An extended version of the **classical isotropic Coulomb friction model** is provided in Abaqus [11] for use with all contact analysis capabilities. The extensions include an additional limit on the allowable shear stress, anisotropy, and the definition of a "secant" friction coefficient.

The standard Coulomb friction model assumes that, no relative motion occurs if the equivalent frictional stress is less than the critical stress (τ_{crit}). It is proportional to the contact pressure (p), in the form $\tau_{crit} = \mu\, p$, where μ can be defined as a function of the contact pressure, the slip rate ($\dot{\gamma}_{eq}$), the average surface temperature, at the contact point and the average field variables at the contact point. Rate-dependent friction cannot be used in a static Riks analysis since velocity is not defined. Hence, equivalent stress is formed by:

$$\tau_{eq} = \sqrt{\tau_1^2 + \tau_2^2} \hspace{5cm} [60]$$

In Abaqus it is possible to put a limit on the critical stress:

$$\tau_{crit} = \min(\mu p, \tau_{max}) \hspace{4.5cm} [61]$$

If the equivalent stress is at the critical stress ($\tau_{eq} = \tau_{crit}$), slip can occur. If the friction is isotropic, the direction of the slip and the frictional stress coincide, which is expressed in the form:

$$\frac{\tau_i}{\tau_{eq}} = \frac{\dot{\gamma}_i}{\dot{\gamma}_{eq}} \hspace{5.5cm} [62]$$

where $\dot{\gamma}_i$ is the slip rate in direction i and $\dot{\gamma}_{eq}$ is the magnitude of the slip velocity,

$$\dot{\gamma}_{eq} = \sqrt{\dot{\gamma}_1^2 + \dot{\gamma}_2^2} \hspace{5cm} [63]$$

For this project, an isotropic friction behavior is used, however, the same laws can be used for anisotropic friction after some simple transformations.

2.7. Finite elements analysis procedures

The finite element method (FEM) has become the most popular method in both research and industrial numerical simulations. Several algorithms, with different computational costs, are implemented in the finite element codes, ABAQUS [11], [12], [13]. Understanding the nature of these procedures is very helpful for choosing the right algorithm for a particular problem [40].

2.7.1. Implicit analysis

Implicit methods have been used in all the simulation in this thesis. Those approaches can be used for static and dynamic analysis, in this case, only the static one is adopted.

Eigenvalue buckling analysis procedure

In the case of buckling, an eigenvalue analysis is computed. The procedure for it in Abaqus [11]:

- It is generally used to estimate the critical (bifurcation) load of "stiff" structures
- It is a linear perturbation procedure
- It can be the first step in an analysis of an unloaded structure, or it can be performed after the structure has been preloaded.
- It can be used in the investigation of the imperfection sensitivity of a structure
- It works only with symmetric matrices (hence, unsymmetric stiffness contributions such as the load stiffness associated with follower loads are symmetrized)
- It cannot be used in a model containing substructures

In an eigenvalue buckling problem, the loads for which the model stiffness matrix becomes singular are searched, so that the problem has nontrivial solutions:

$$K^{MN} \, v^M = 0 \qquad\qquad [64]$$

K^{MN} is the tangent stiffness matrix when the loads are applied, and the v^M are nontrivial displacement solutions. The buckling loads are computed relative to the base state of the structure and omit the material non-linearity, remaining the elastic properties.

In addition, an incremental loading pattern Q^N is defined in the eigenvalue buckling prediction step. The magnitude of this loading is not important; it will be scaled by the load multipliers, λ_i, found in the eigenvalue problem:

$$(K_0^{NM} + \lambda_i K_\Delta^{NM})v_i^M = 0 \qquad\qquad [65]$$

Where

- K_0^{NM} is the stiffness matrix corresponding to the base state, which includes the effects of the preloads, P^N (if any)
- K_Δ^{NM} is the differential initial stress and load stiffness matrix due to the incremental loading pattern, Q^N
- λ_i are the eigenvalues
- v_i^M are the buckling mode shapes (eigenvectors)
- *M* and *N* refer to degrees of freedom M and N of the whole model
- *i* refers to the "ith" buckling mode

Finally, in order to select the eigenvalue extraction method, Abaqus offers the Lanczos and the subspace iteration eigenvalue extraction methods.

The Lanczos method is generally faster when a large number of eigenmodes is required for a system with many degrees of freedom. The subspace iteration method may be faster when only a few (less than 20) eigenmodes are needed. For this thesis, the subspace iteration method is adopted because of only the first eigenmode value is needed. This mode is the most critical as it can be observed in Chapter 4.

Riks method

One of the static methods applied along the computations of this thesis is the Riks method [11].

This procedure:

- is generally used to predict unstable, geometrically nonlinear collapse of a structure
- can include nonlinear materials and boundary conditions
- often follows an eigenvalue buckling analysis to provide complete information about a structure's collapse
- can be used to speed convergence of ill-conditioned or snap-through problems that do not exhibit instability

Geometrically nonlinear static problems sometimes involve buckling or collapse behavior, where the load-displacement response shows a negative stiffness and the structure must release strain energy to remain in equilibrium. Several approaches are possible for modeling such behavior. In simple cases linear eigenvalue analysis may be sufficient for design evaluation but, if there is concern about geometric nonlinearity prior to buckling, or unstable post-buckling response, a load-deflection (Riks) analysis must be performed to investigate the problem further.

If the Riks step is a continuation of a previous history, any loads that exist at the beginning of the step and are not redefined are treated as "dead" loads with constant magnitude. A load whose magnitude is defined in the Riks step is referred to as a "reference" load. All prescribed loads are ramped from the initial (dead load) value to the reference values specified.

The loading during a Riks step is always proportional. The current load magnitude, P_{total}, is defined with *expression 66*:

$$P_{total} = P_0 + \lambda(P_{ref} - P_0)$$
[66]

Where P_0 is the "dead load", P_{ref} is the reference load vector, and λ is the "load proportionality factor." The load proportionality factor is found as part of the solution.

2.7.2. Explicit dynamic analysis

In spite of there is no necessity to compute an explicit dynamic procedure [11] to reach successful results along this project, it is very interesting to study how it works mathematically because this type of analysis plays a key role for simulations where are involved in a particular assembly elements such as springs. Moreover, this analysis is also common for dynamics simulations (e.g. crash simulation in a vehicle).

- Numerical implementation

$$\dot{u}^N_{(i+\frac{1}{2})} = \dot{u}^N_{(i-\frac{1}{2})} + \frac{\Delta t_{(i+1)} + \Delta t_{(i)}}{2} \ddot{u}^N_{(i)}$$
[67]

$$u^N_{(i+1)} = u^N_{(i)} + \Delta t_{(i+1)} \dot{u}^N_{(i+\frac{1}{2})}$$
[68]

Where u^N is a degree of freedom (a displacement or rotation component) and the subscript i refers to the increment number in an explicit dynamics step.

- Stability

$$\Delta t \leq \frac{2}{w_{max}}$$
[69]

- Dilatational wave speed

$$c_d = \sqrt{\frac{\hat{\lambda} + 2\hat{\mu}}{\rho}}$$
[70]

Where ρ is the density of the material.

In an isotropic elastic material, the effective Lamé's constants can be defined in terms of Young's modulus, E, and Posisson's ratio, ν, by:

$$\hat{\lambda} = \lambda_0 = \frac{E\,\nu}{(1+\nu)(1-2\nu)}$$
[71]

and

$$\hat{\mu} = \mu_0 = \frac{E}{2(1 + v)} \qquad [72]$$

- Computational cost

The computer time involved in running a simulation using explicit time integration with a given mesh is proportional to the time period of the event. The time increment based on the element-by-element stability estimate can be expressed as follows:

$$\Delta t \leq \min \left(L_e \sqrt{\frac{\rho}{\hat{\lambda} + 2\hat{\mu}}} \right) \qquad [73]$$

Where the minimum is taken over all elements in the mesh, and L_e is a characteristic length associated with an element.

The drawback of the explicit method is that it is conditionally stable. The stability limit for an explicit operator is that the maximum time increment must be less than a critical value of the smallest transition times for a dilatational wave to cross any element in the mesh. Secondly, the nature of the explicit method limits it to the analysis of short transient problems.

3. FE-MODEL BUILD UP

Along this section, materials used and model creation process are going to be described. An implementation of a realistic model is the key to obtain accurate results. Therefore, a theoretical approach to define elastic properties of the laminate, using micromechanical models, are taken from reference [10] Chapter 2. "Mechanical properties calculation of the composite panel".

## 3.1.	Description of the materials used

Material used along this project has composed by carbon fiber with epoxy as a matrix. The laminate different types of plies from this composite material: Woven and Unidirectional (UD) carbon fiber orientation. Furthermore, the company ClipCarbono (La Coruña, Spain) has provided the samples tested in the experimental part.
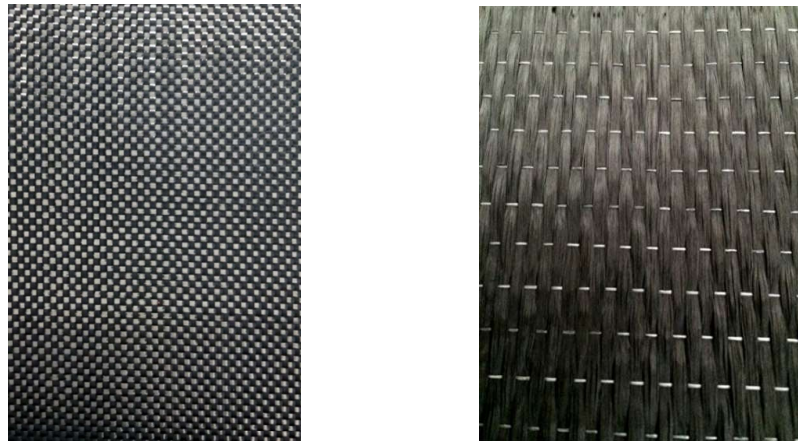
Figure 14. Woven CFRP laminate (left), UD CFRP laminate (right)

For the old version of the device frame, the laminate Tsai identification code is $[0_W, 0_{UD}, 90_{UD}, 0_{UD}, 90_{UD}, 0_{UD}, 90_{UD}]_S$. Furthermore, as *Table 1* shows, the thickness of each ply is:

Fiber direction	Thickness [mm]
Woven	0,202
UD	0,144

Table 1. Ply thickness for the two types of fiber configuration [10]

It concludes that total thickness reach 2,132 mm

It is important to take into account that mechanical properties values are not available for the real specimens; however, there are information from carbon fiber and epoxy resin, which are perfectly valid.

Carbon fiber has an orthotropic behavior, for this reason is necessary to know mechanical parameters in more than one direction.

$E_{1,f}$ **[GPa]**	230
$E_{2,f}$ **[GPa]**	15
ρ **[kg/m^3]**	1800
$\nu_{12,f}$ **[-]**	0.3
$G_{12,f}$ **[GPa]**	9
$\sigma_{f,F}$ **[MPa]**	4400
$\varepsilon_{max,f}$ **[-]**	0.018

Table 2. Carbon fiber properties [10]

In addition, the prepeg layers and its resin are an isotropic material. Therefore, in order to define the elastic mechanical behavior, only the Young's modulus (E) and Poisson's ratio (ν) are needed. Furthermore, the unique parameter computed is shear modulus which is shown with *expression 74*:

$$G = \frac{E}{(2\,(1+\nu))}$$ [74]

Those parameter values are exposed in *Table 3*:

E_m **[GPa]**	3.8
ρ_m **[kg/m^3]**	1250
ν_m **[-]**	0.38
G_m**[GPa]**	1.38

Table 3. Epoxi resin properties [10]

Properties values from the two last tables will be useful to compute the rest of the mechanical parameters. Those are essential to reach precise results when analytical procedures are used. Moreover, the company TEIJIN CARBON EUROPE GMBH (Wuppertal, Germany) manufactured both materials.

3.2. Mechanical properties of UD and Woven plies

The entire laminate is composed by 14 plies with two different orientations: 0º and 90º following the next sequence:

Ply	Material	t [mm]	Φ [º]
1	Woven	0.202	0
2	UD	0.144	0
3	UD	0.144	90
4	UD	0.144	0
5	UD	0.144	90
6	UD	0.144	0
7	UD	0.144	90
8	UD	0.144	90
9	UD	0.144	0
10	UD	0.144	90
11	UD	0.144	0
12	UD	0.144	90
13	UD	0.144	0
14	Woven	0.202	0

Table 4. Old plies classification. Laminate material, thickness and orientation [10]

More details about the configuration of the plies for the laminate are illustrated in *Figure 15:*
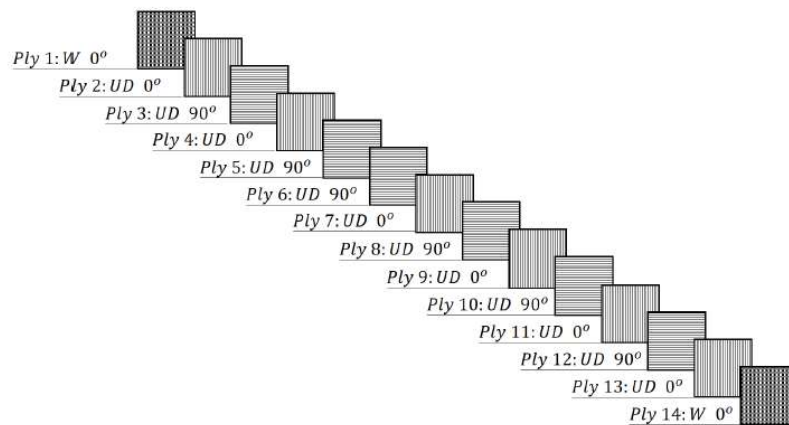

Figure 15. Ply stacking sequence [10]

As it can be found in Ferrer O., José A. (2018) [10], the best fitting found with the experimental results has been for:

$$V_{f,UD} = 0{,}58 \qquad [75]$$

$$V_{f,W} = 0{,}55 \qquad [76]$$

Where micromechanical models were applied to obtain those properties values for a laminate plate.

Summary table:

Mechanical properties. Composite panel		
	UD	Woven
E_1 [GPa]	135	70.18
E_2 [GPa]	8.4	70.18
ν_{12} [-]	0.334	0.058
ν_{21} [-]	0.0208	0.058
G_{12} [GPa]	3.51	4.05
G_{13} [GPa]	3.51	3.18
G_{23} [GPa]	2.68	3.18

Table 5. Mechanical properties values for each laminate type [10]

3.3.   Description of the CAI test device models

CAI test device is composed by different components in its framework, such as supports (lateral, upper and lower part) as an assembly. Apart from the framework of the device, the test procedure requires a sample plate, which is also modeled in order to be able to reproduce its damage, and the main test characteristic that the sample has (shortening, reaction force in its normal direction caused by its LSs…) during the software simulation. Several CAD models are presented for the sample, as well as the LSs. It is essential to take into account that simulations have been carried out for a **combination of**:

a) CAI width frame of the Old version device
b) LSs from the new version CAI test frame, developed at HAW lightweight laboratory [7].

Finally, boundary conditions visualization and contact definition between the bodies from the assembly is also described.

3.3.1.   OLD VERSION CAI TEST DEVICE FROM HAW HAMBURG

As the CAI test device that Airbus used [35], the lower part is clamped in all its areas. This device (Old version CAI test device from HAW Hamburg) has several construction details in its upper part.

Due to the necessity (in all the CAI test devices) of a free area on the upper part of the device, a gap of 4 mm approximately is stablished to allow the compression, when the test is carried out. Furthermore, sliding edges are located 5 mm per side.
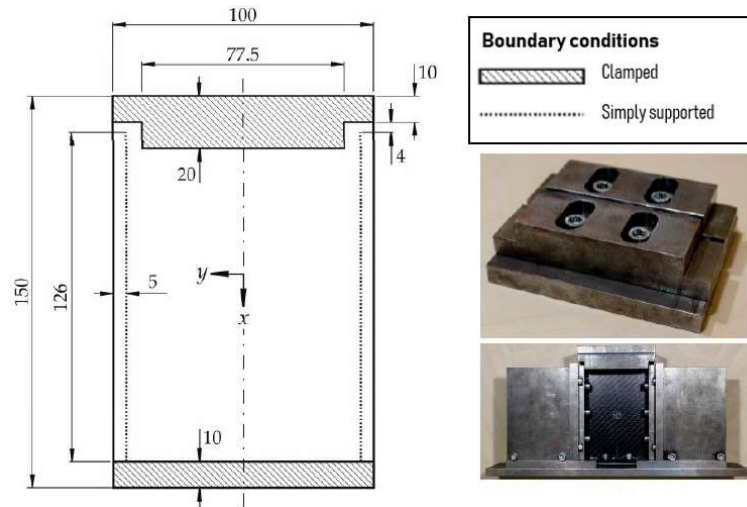

Figure 16. Old CAI test device frame developed at HAW Hamburg lightweight laboratory [8]

3.3.2. NEW VERSION OF LATERAL SUPPORTS DEVELOPED AT HAW HAMBURG

Several sketches are shown to clarify the LSs geometry and the forces that they are submitted.
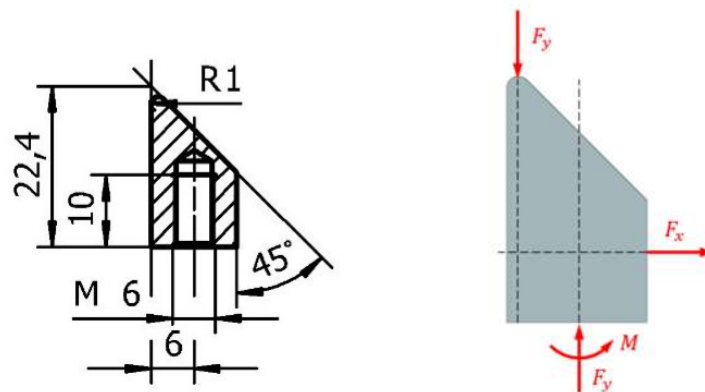

Figure 17. 2D detailed sketch from the LSs cross section (left), CAD model of LSs (right) [7]

3.3.3. FE-MODELS DESCRIPTION

In addition, the following models will be created to reach the aim of this thesis:

a) 2D plate FE-model

Three 2D FE-models will be computed along chapter 4, the differences between them are listed as follows:

    i.   **Model 1.** 2D model with 90 mm width plate.
    ii.   **Model 2.** 2D model with 100 mm width plate. (Influence of width plate)
    iii.   **Model 3.** CAI device assembly. 2D model with 100 mm width plate, contact applied between specimen and LSs.

b) 3D plate FE-model

As in the case of 2D FE-models, three 3D FE-models are created:

    iv.   **Model 4.** 3D model with 100 mm width plate.
    v.   **Model 5.** CAI device assembly. 3D model considering contact applied between specimen and LSs.
    vi.   **Model 6.** CAI device assembly. 3D sample plate model. LSs with screws modeled. The following FE-models can be distinguished depending on the screws attachment behavior:

- **Model 6.1.** Rigid connection
- **Model 6.2.** Linear stiffness behavior in connectors (without preload)
- **Model 6.3.** Non-linear stiffness behavior in connectors (with preload)

For a better understanding, a summary table with all the FE-models used along this thesis is presented in the *Table 6*:

	Plate [-]	Width plate [mm]	LSs [-]	Screws [-]
Model 1	2D	90	x	x
Model 2	2D	100	x	x
Model 3	2D	100	✓	x
Model 4	3D	100	x	x
Model 5	3D	100	✓	x
Models 6.1, 6.2, 6.3	3D	100	✓	✓

Table 6. Introduction table with all the CAD models

3.3.4. COMPOSITE PLATE

The sample used in the CAI test is made by CFRP. In addition, its Young's modulus, amount of plies, plies thickness, poisson's ratio and laminate configuration are defined as an input in Abaqus.

From the simplest model (2D) to the complex one is the modeled procedure has been followed along this thesis. It allows observing clearly the main differences between models in each single step.

- 2D PLATE

As it was mentioned, the first step is the simplest model (2D shell geometry) with 1920 structured quad elements in its mesh (S4R). As *Figure 18* shows, there are partitions along the X-dimension on the plate, they represent the location of the lateral supports from the CAI test device. In the case of the 2D plate model, boundary conditions for the lateral supports will be defined along those partitions (5 mm from each lateral side).
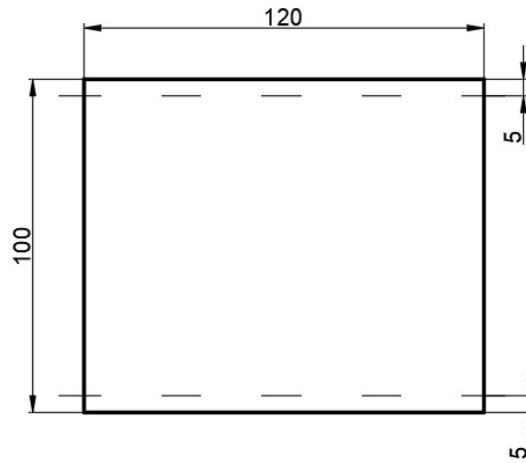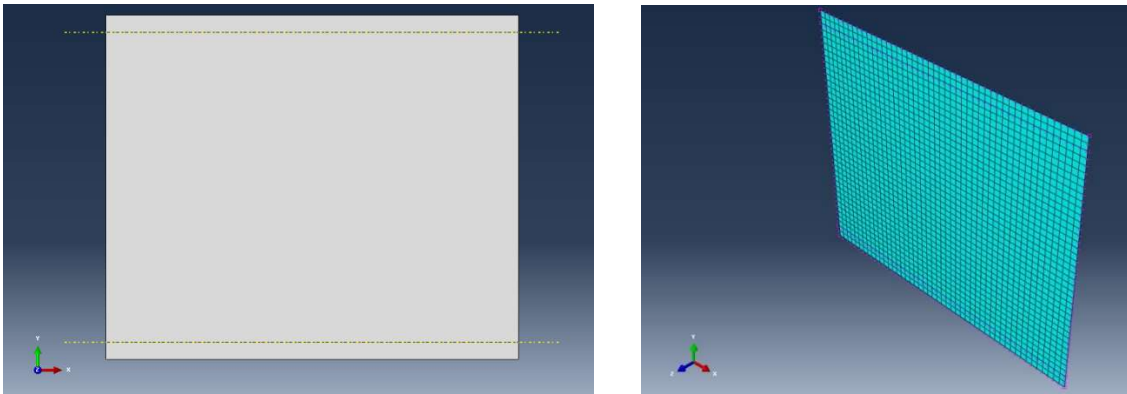
Figure 18. Dimension of the sample plate

Figure 19. Shell body representation (left), 2D mesh (right)

- 3D PLATE

To obtain 3D plate, a thickness is applied in the previous model (t = 2.132 mm). It means there are two long surfaces in this case (external and internal side) and, with regard to the mesh, hexahedron are created instead of quad elements. In addition, boundary conditions from the lateral supports have to be applied for both sides of the sample in this case. Now the 3D plate mesh presents hexahedron (SC8R) shapes instead of quads.
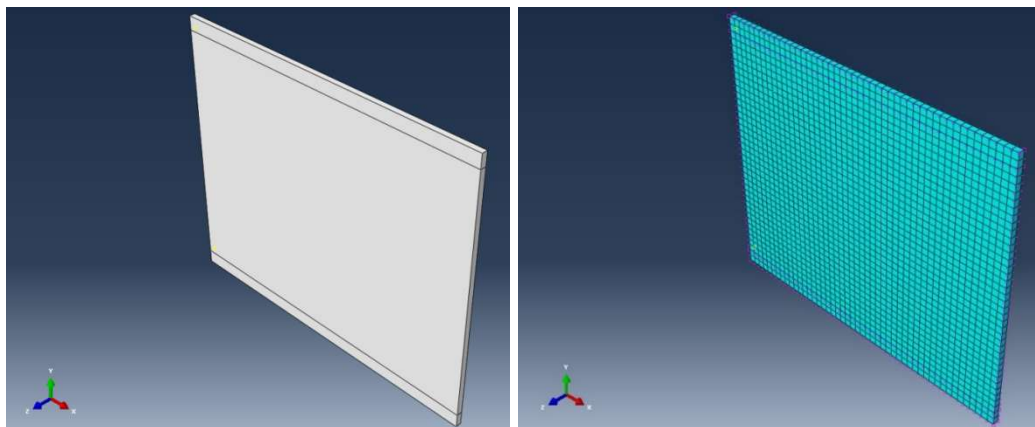

Figure 20. 3D plate model. Geometry (left) and 3D Mesh (right)

3.3.5. LATERAL SUPPORTS

In the case of the lateral supports models, several cross section shapes have been tested as a CAD model. A 3D mesh for the lateral supports is also needed, in this case the elements selected will be (C3D8R), this element type are adequate for 3D stress in an isotropic solid and they are hexahedrons.

- DIFFERENT LATERAL SUPPORT SHAPES

- **Flat and rounded tip**

As a first lateral support prototype, *Figure 21* shows a flat tip in its cross section, this presents several advantages in its implementation because of its simplicity. On the one hand, with the flat tip model is significantly easy to create the geometry and, therefore, establish the contact between LSs and plate. However, it is not possible to model the cross section in this way because in a flat tip appears bending moments and it does not represent with accuracy the reality.
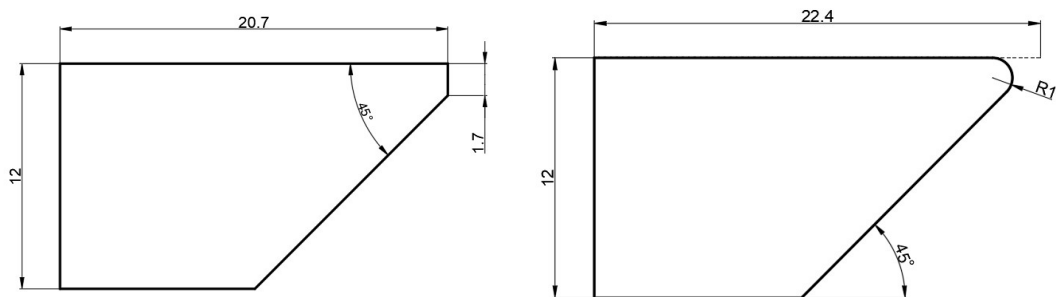

Figure 21. Flat (left) and Rounded (right) tip

On the other hand, rounded tip geometry is more realistic; nevertheless, it has an important drawback that is the penetration in the sample part when the simulation is carried out. In a first approach, the contact is properly stablished but, after several time steps, the rounded part starts to penetrate into the plate.
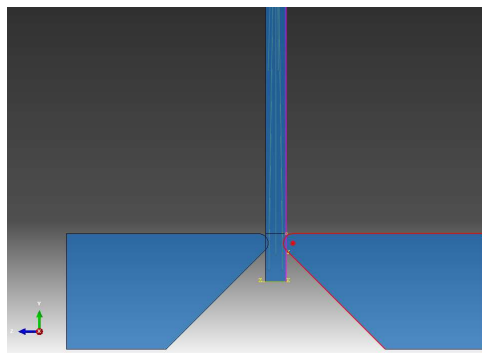

Figure 22. Lateral support penetration

- **Pyramid-shaped**

Pyramidal shape for the cross section allows a great accuracy in the contact definition along the edges on the plate (where the LS are located). A preliminary model was created (*Figure 23 - left*) however, due to several difficulties that they will be shown in section 4. (Results discussion and model verification), it was necessary to implement a new model; similar to the previous one but around three times bigger, to counter the LSs deformation during the simulation.
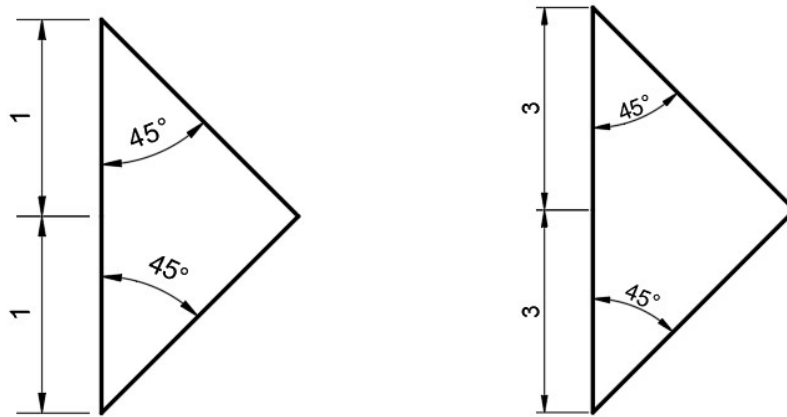
Figure 23. Pyramidal cross section shape for lateral supports. Simplification (left) and normal (right)

The cross section from the left picture was created as a preliminary model because it allows a less amount of elements in its mesh and therefore, the solver is faster when the simulations are computed. However, when LSs does not have their boundary conditions on their own body (e.g. Assembly model with screws) significant deformations appear on them, inducing not proper results when the simulation is carried out. Therefore, a bigger cross section (three times higher) is created to avoid such a deformation.

- LATERAL SUPPORTS. SCREWS MODEL

Due to the real device framework presents screws in its lateral supports to hold the sample in the proper position when the CAI test is carried out, connectors elements from ABAQUS with preload applied are positioned on LSs CAD model to reach a more realistic approach. As it follows, configuration of the connectors can be observed in *Figure 26* for the CAD model assembly.

LSs composed by two parts:
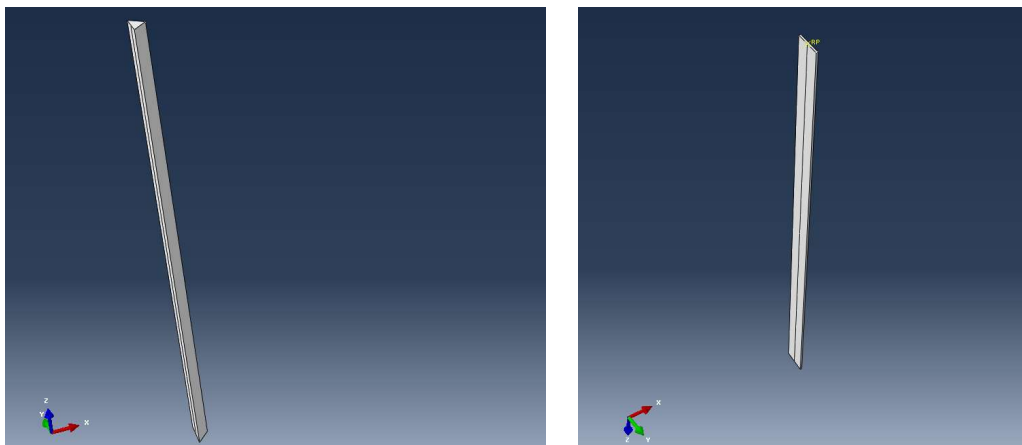
- Deformable tip and rigid flat body

Figure 24. Deformable body as a lateral support (left), rigid flat part (right)

The rigid part will be attached at the bottom of the deformable body in order to avoid deformations along the LSs when the boundary conditions are applied on the connector

elements (screws model). When a screw is modeled, it has to be connect in its extreme to a two different nodes (it does not consider all the face) from the mesh, that is why significant deformations can be appear if LSs do not present a rigid part.

- Lateral support. Screw separation and LSs assembly

Figure 25. Lateral support sketch (left). CAD lateral support assembly model (right)

- CAI CAD Model assembly

As it can be observed in *Figure 26,* six screws are modeled as a connector element with uniaxial behavior.

Figure 26. Screws modeled on the lateral supports

3.3.6. BOUNDARY CONDITIONS

The following point provide some useful insights into the boundary conditions definition, for the sample plate as well as the LSs.
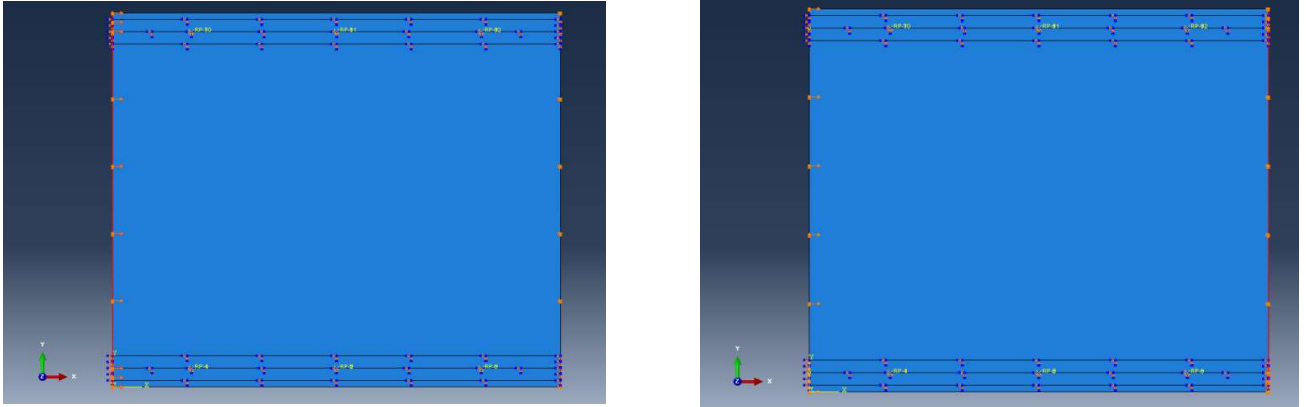
- SAMPLE PLATE

Figure 27. Upper part of the plate (left), lower part (right)

Boundary conditions applied on the plate are located on the upper and lower part.

- Upper part displacement in X direction (1 mm). Movement in Y and Z fixed
- Lower part completely clamped

- LATERAL SUPPORTS

Concerning LSs, different boundary conditions are applied depending on the their location in the assembly. In the case of the left picture below, all the DoF are fixed however, for the ones that are positioned in the opposite side, displacement in Z-direction is allow because of the springs implementation on them.
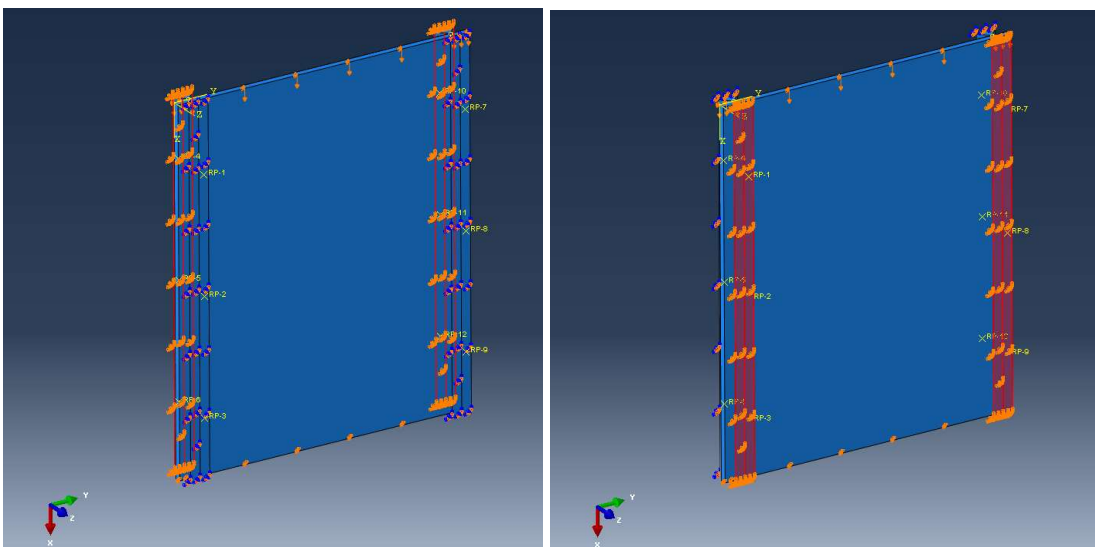

Figure 28. Lateral supports with all the DoF fixed (left), movement only fixed in X and Y direction (right)

3.3.7. RIGID AND DEFORMABLE LATERAL SUPPORT BODIES

- RIGID (IDEALIZATION)

As a rigid body, it needs a reference point in which the boundary conditions are applied. A rigid body as to be modeled as a surface in Abaqus, to be able to introduce it in the assembly.
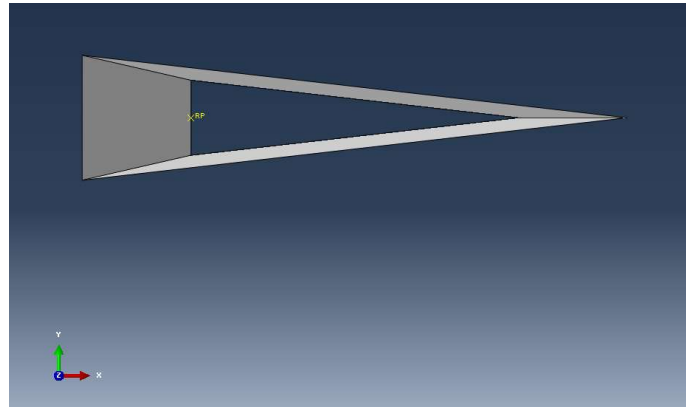

Figure 29. Top view LS as rigid body

- DEFORMABLE
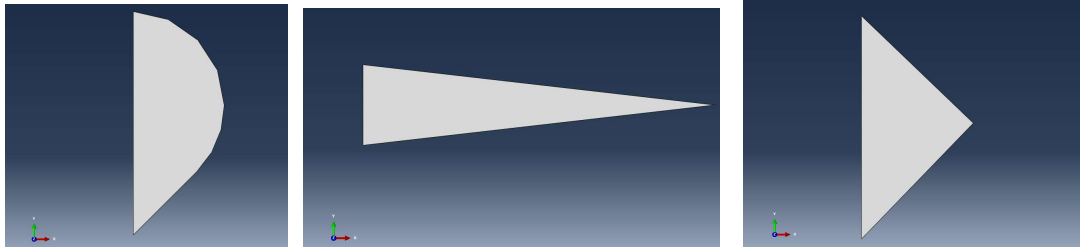
Below, three different tip shapes were modeled:

Figure 30. Different cross sections for LSs. Rounded tip (left), slender sharp tip (middle) and sharp tip (right)

Several issues were found during the CAD assembly implementation:

- Rounded tip shape (real tip shape). Penetrations were presented into the sample plate while simulations were computed.
- Slender sharp tip shape. Large deformation appeared during the simulations.

Finally, LSs sharp tip is considered when simulations are carried out in assembly FE-models (see in 3.3.3. FE-models description).

4. RESULTS DISCUSSION AND MODEL VERIFICATION

As it has been mentioned in section "1. Introduction", the aim of this project is to verify a FE model of the CAI test device from HAW Hamburg. Furthermore, the influence of the lateral supports from the CAI test device play a key role in the test results, because of that, simulations with different LSs models will be carried out.

To reach this goal, results from several FE models will be analyzed along this section, starting with an easier and ending with models that are more complex.

4.1. Analytical calculation

Before any CAD model presentation, it is necessary to carried out a mesh dependency study, in order to proof which mesh will be accurate enough to compute all the future computation in the CAI device model. Therefore, analytical calculation is carried out for buckling analysis, obtaining the critical stress value where the plate reaches the first buckling mode (m=1).

In order to contrast theoretical and FEM results for buckling analysis, is interesting to study a simple model as could be an aluminum plate simply supported in all its sides. Its main geometrical characteristic are:

Plate geometry. Model 1	
a [mm]	120
b [mm]	90
t [mm]	2.132

Table 7. Sample plate dimensions. Model 1

Mechanical properties are also needed for buckling analysis:

Mechanical properties. Aluminum	
E [GPa]	70
ν [-]	0.33

Table 8. Mechanical properties Aluminum. Buckling analysis

As it was presented in Section 3 "FE-Model build up", critical buckling stress for simply supported isotropic plates, under uniaxial compression, can be expressed as:

$$\sigma_{cr} = \frac{N_{cr}}{t} = \frac{\pi^2 \cdot D \cdot (m^2 + \alpha^2)^2}{t \cdot b^2 \cdot m^2 \cdot \alpha^2} \tag{77}$$

Where D is:

$$D = \frac{E \cdot t^3}{12 \cdot (1 - \nu^2)} = \frac{70 \; 10^9 \cdot (2{,}132 \cdot 10^{-3})^3}{12 \cdot (1 - 0{,}33^2)} = 63{,}44 \; N \; m \tag{78}$$

For the first buckling mode (m = 1):

$$\sigma_{cr} = \frac{\pi^2 \cdot 63{,}44 \cdot (1^2 + (\frac{120}{90})^2)^2}{2{,}132 \cdot 90^2 \cdot 1^2 \cdot (\frac{120}{90})^2} = 157{,}361 \frac{N}{mm^2} = 157{,}361 \, MPa \qquad [79]$$

For m = 2:

$$\sigma_{cr} = \frac{\pi^2 \cdot 63{,}44 \cdot (2^2 + (\frac{120}{90})^2)^2}{2{,}132 \cdot 90^2 \cdot 2^2 \cdot (\frac{120}{90})^2} = 170{,}206 \frac{N}{mm^2} = 170{,}206 \, MPa \qquad [80]$$

- Composite plate. Carbon fiber. Four sides simply supported.

In the same way as the isotropic plate, for a composite material with orthotropic behavior, mathematical expressions bellow are computed, as well as the mechanical properties of the composite plate [10].

Laminate stiffness values:

$$B_x = D_{11} = 64{,}48 \, N \, m \qquad [81]$$

$$B_y = D_{22} = 50{,}78 \, N \, m \qquad [82]$$

$$B_{xy} = D_{12} + 2D_{66} = 2{,}75 + 2 \cdot 3{,}04 = 8{,}83 \, [N \cdot m] \qquad [83]$$

$$\sigma_{cr} = \frac{1}{t} \cdot \left(\frac{\pi}{b}\right)^2 \cdot \left[B_x \cdot \left(\frac{m}{\alpha}\right)^2 + 2 \cdot B_{xy} + B_y \cdot \left(\frac{\alpha}{m}\right)^2 \right] \qquad [84]$$

For m = 1:

$$\sigma_{cr} = \frac{1}{2{,}132} \cdot \left(\frac{\pi}{90}\right)^2 \cdot \left[64{,}48 \cdot \left(\frac{1}{\left(\frac{120}{90}\right)}\right)^2 + 2 \cdot 8{,}83 + 50{,}78 \cdot \left(\frac{\left(\frac{120}{90}\right)}{1}\right)^2 \right] \qquad [85]$$
$$= 82{,}416 \, MPa$$

For m = 2:

$$\sigma_{cr} = \frac{1}{2{,}132} \cdot \left(\frac{\pi}{90}\right)^2 \cdot \left[64{,}48 \cdot \left(\frac{2}{\left(\frac{120}{90}\right)}\right)^2 + 2 \cdot 8{,}83 + 50{,}78 \cdot \left(\frac{\left(\frac{120}{90}\right)}{2}\right)^2 \right] \qquad [86]$$
$$= 105{,}907 \, MPa$$

Critical value for the first buckling mode (m = 1) is used in both cases because it is clearly lower than the value from m = 2.

4.2.   Mesh dependency and 2D models comparison

A mesh dependency study has been carried out to verify the models which are going to be used along the thesis. This has involved computing buckling simulations as well as post-buckling analysis.

4.2.1. Buckling

Aluminum and a composite plate under simply supported conditions have been computed. Due to aluminum plate simplicity, it is interesting to realize a comparison between theoretical and FE method as a first approach. To help the explanation, numerical results are shown in a table as well as in a graph.

Aluminum Plate. All its sides simply supported (Shell 2D. Width: 90 mm, Length: 120 mm)

- ▪ Theoretical Stress value = 157,36 MPa

N° Elements	Buckling stress [MPa]	Model vs Theorical Value [%]	FEM Variation Values [%]
48	165,49	5,17	-
192	159,02	1,05	3,91
768	157,47	0,07	0,97
3072	157,08	0,18	0,24

Table 9. Mesh dependency study for a shell aluminum plate simply supported. Buckling critical stress values

As *Table 9* shows, variation values from FEM decreases from 12 elements used in the model mesh, reaching a value of 0.24 % when 3072 elements take part of the body mesh. Furthermore, same tendency is followed in the case of FEM and theoretical method comparison.

Aluminum Plate Classical Kirchhoff Shell Theory (Shell 2D. Width: 90 mm, Length: 120 mm)

- ▪ Theoretical Stress value = 157,36 MPa

N° Elements	Buckling stress [MPa]	Model vs Theorical Value [%]	FEM Variation Values [%]
48	151,16	3,94	-
192	155,76	1,02	3,04
768	156,95	0,26	0,77
3072	157,26	0,07	0,19

Table 10. Mesh dependency study for a shell aluminum with boundary conditions from CKST. Buckling critical stress values
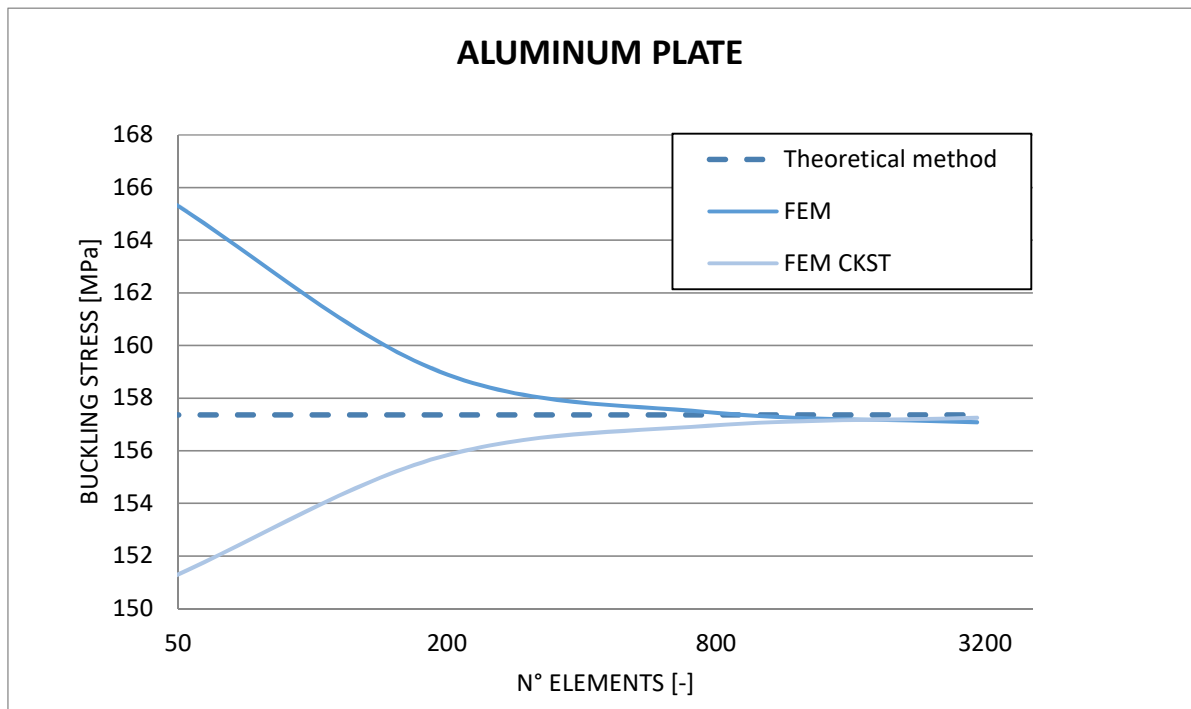
Figure 31. Buckling stress values comparison for aluminum plate. Mesh dependency.

Figure 31 shows that stress values, which belong to 1000 elements or higher, does not present a significant variation.

This is because, Classical Kirchhoff Shell Theory is applied to obtain the values using the analytical method, and however, when FEM computation was applied for thin shell elements in *Figure 31*, the boundary conditions considered were not according to the CKST (quads elements does not reproduce properly the assumptions from CKST). In contrast, FEM CKST curve (using triangles elements in its mesh "STRI3") is faithful to the boundary conditions from this analytical theory, and it can be observed that, the buckling values does not intersect with the theoretical ones.

Classical Kirchhoff Shell Theory assumptions are given as follows:

1. Dimensions in the normal direction from the mid-plane of the plate remain straight and normal to the midsurface. (Only adequate for small thickness shells)
2. Small stress σ_z can be neglected.
3. Hypothesis about small displacements and deformations and linear behavior are also applied.

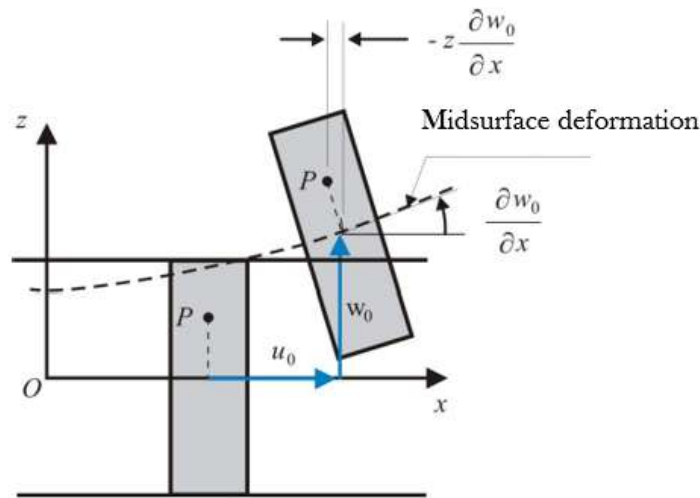To illustrate those assumptions, *Figure 32* is shown:

Figure 32. Classical Kirchhoff shell theory

Composite Plate. All its sides simply supported (Shell 2D. Width: 90 mm, Length: 120 mm)

Secondly, composite plate is a slightly more complex model than the aluminum one. It is analyzed also for a buckling calculation reaching the following results:

- Theoretical Stress value = 82,42 MPa

N° Elements	Buckling stress [MPa]	Model vs Theoretical Value [%]	FEM Variation Values [%]
48	85,98	4,33	-
192	82,55	0,16	3,99
768	81,73	0,84	0,99
3072	81,53	1,08	0,25

Table 11. Mesh dependency study for a shell composite plate simply supported

In the case of the composite plate, buckling stress values follow the same tendency as the aluminum plate. However, the unique difference is that buckling stress values reached are lower than the aluminum ones. This occurs because aluminum stiffness is higher. Notice that, in the two graphs above, buckling stress values for a large element amount used are lower in the case of FEM than the theoretical ones because again (using quads) does not reproduce properly the CKST assumptions.

Composite Plate Classical Kirchhoff Shell Theory (Shell 2D. Width: 90 mm, Length: 120 mm)

Summary table in accordance with CKST assumptions:

- Theoretical Stress value = 82,42 MPa

N° Elements	Buckling stress [MPa]	Model vs Theoretical Value [%]	FEM Variation Values [%]
48	79,92	3,03	-
192	81,76	0,80	2,29
768	82,25	0,20	0,60
3072	82,38	0,05	0,15

Table 12. Mesh dependency study for a shell composite plate. Boundary conditions CKST
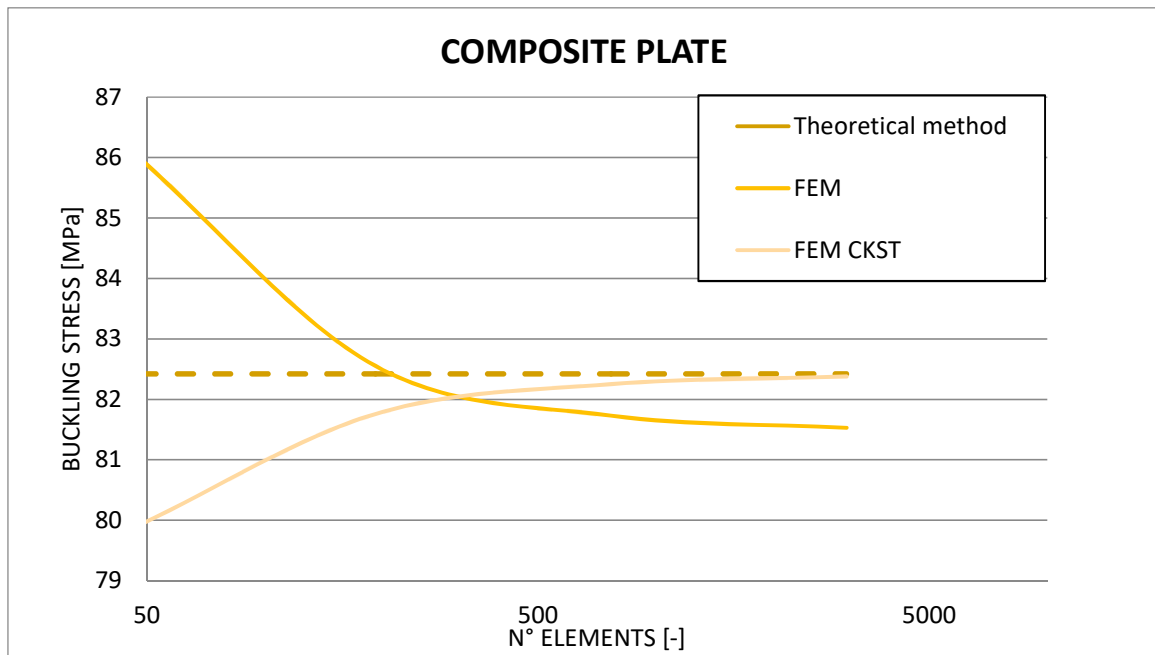
Figure 33. Buckling stress values comparison for CFRP. Mesh dependency.

4.2.2. Post- buckling

Post-buckling mesh dependency study is realized to notice the influence of the mesh refinement in post-buckling values, such as the maximum compression value that the CAI device performs over the sample plate.

Composite Plate (Boundary Conditions: Old Test Device from HAW. Shell 2D Width: 90 mm)

N° Elements	Uniaxial compression [MPa]	Shortening [mm]	Out-of-plane deflection [mm]	Variation Failure values [%]	Variation shortening values [%]	Variation Z deflection values [%]
192	276,349	0,886	5,927	-	-	-
768	261,676	0,814	5,545	5,308	8,148	6,444
3072	270,061	0,861	5,737	3,202	5,803	3,471
12288	266,052	0,843	5,657	1,485	2,113	1,399

Table 13. Mesh dependency study for a shell composite plate. Post-Buckling critical stress values

The amount of elements in the mesh have been increased in comparison with buckling study furthermore, the variation in the values from each parameter is higher in this case because, post-buckling analysis presents more complicated computations than linear buckling.

To show the tendency of those values in an illustrative manner, two graphs are represented below:
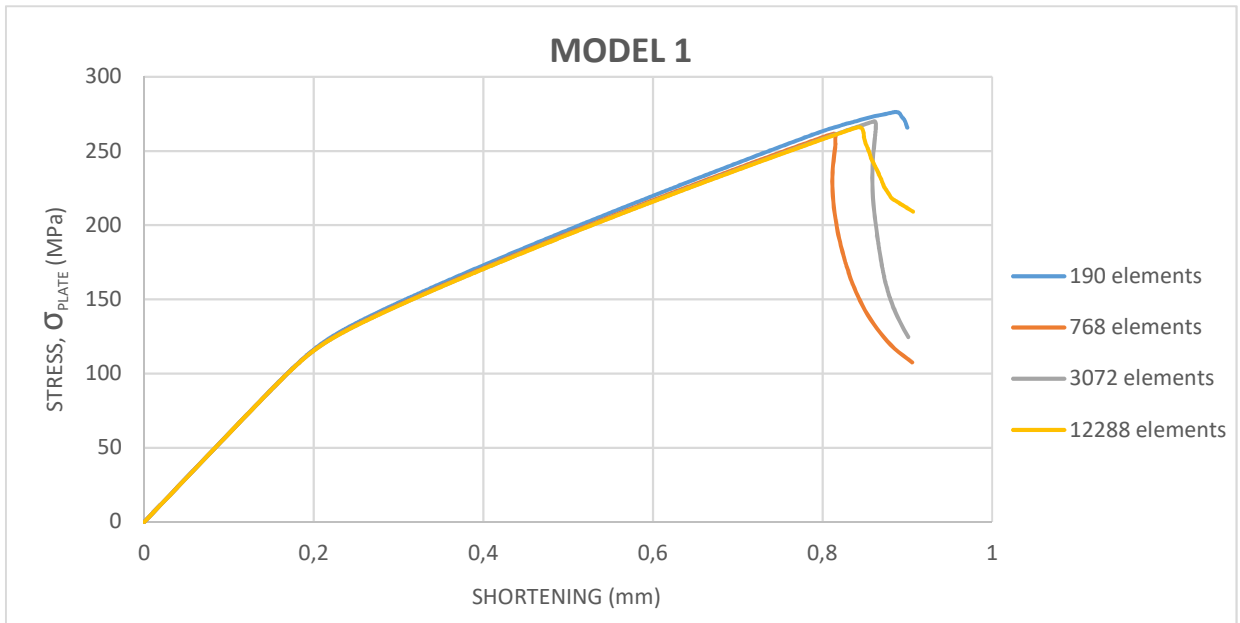

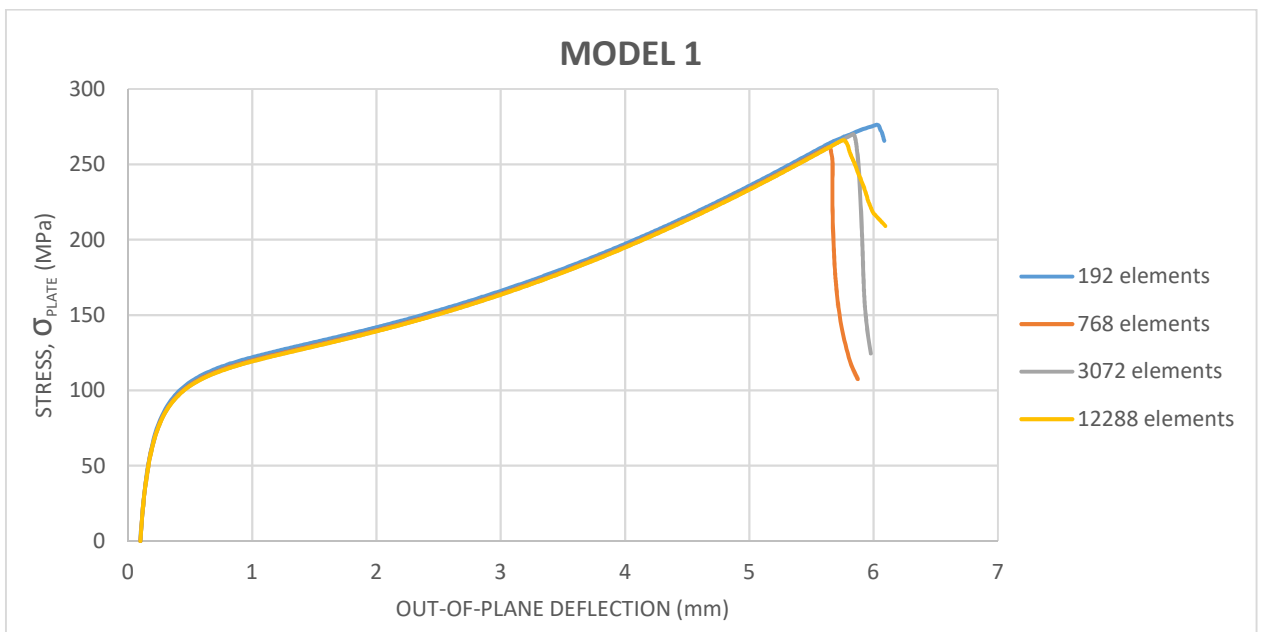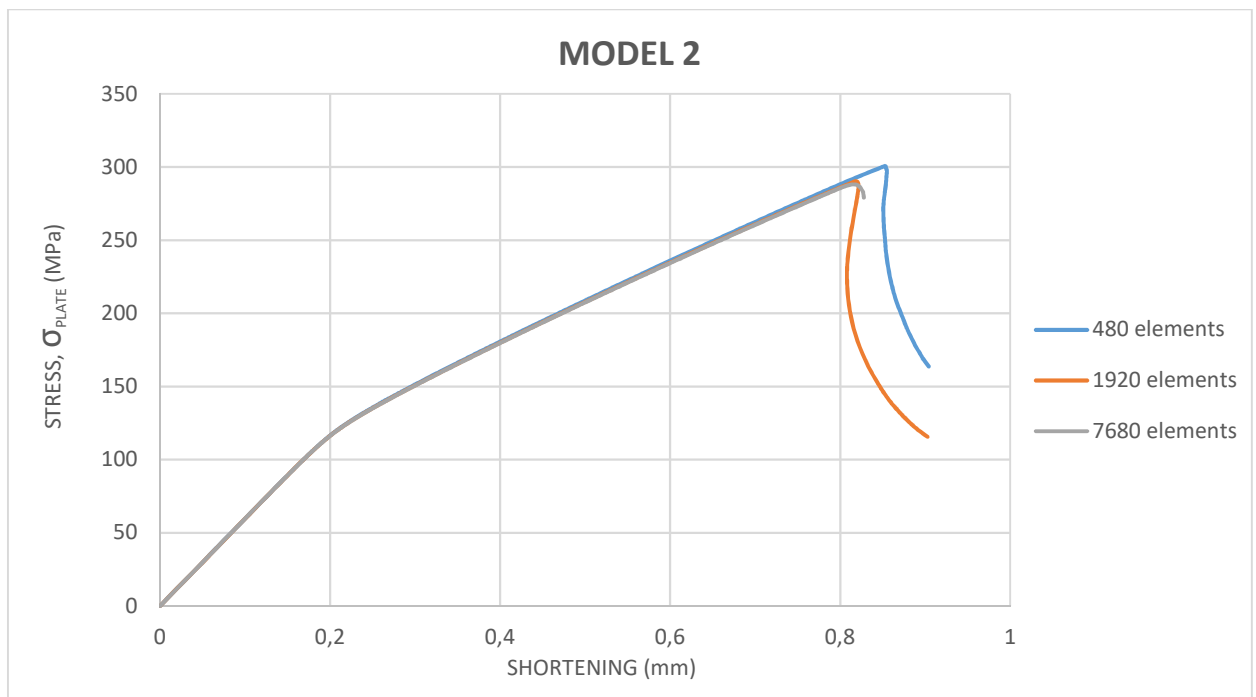Figure 34. Plate shortening for different amount of elements in the mesh
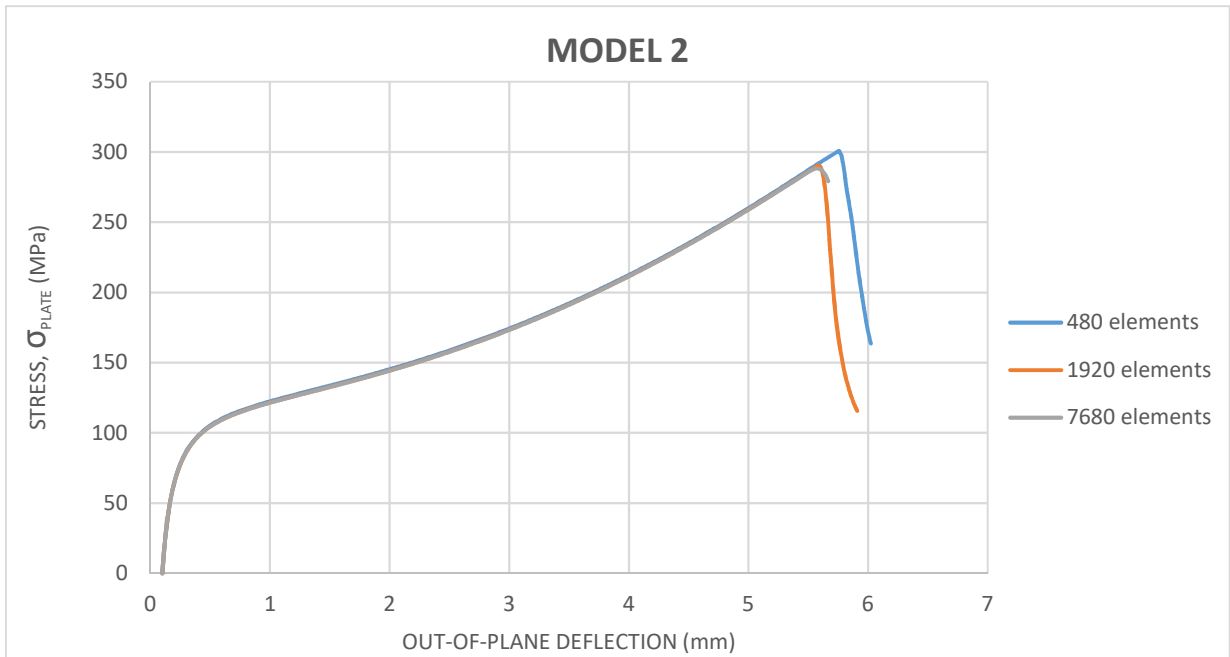

Figure 35. Out-of-plane deflection in the center of the plate for different amount of elements in the mesh

It is important to take into account that a calculation with lower amount of element has less computational cost, for this reason, and because of the similarity of the results between both element quantities, the best choice is compute the simulation with 3072 elements.

Composite Plate (Boundary Conditions: Old Test Device from HAW. Shell 2D Width: 100 mm)

In this case, the only different from the last model is in the width dimension, results are shown in *Table 14*:

N° Elements	Uniaxial compression [MPa]	Shortening [mm]	Out-of-plane deflection [mm]	Variation uniaxial compression [%]	Variation shortening values [%]	Variation Z deflection values [%]
480	300,702	0,853	5,656	-	-	-
1920	290,370	0,819	5,487	3,435	3,991	2,992
7680	288,168	0,816	5,477	0,758	0,267	0,183

Table 14. Mesh dependency study for a shell composite plate. Post-Buckling critical stress values

As it has been shown, uniaxial compression values are around 20 MPa higher than for 90 mm width plate. This aspect will be discussed in section "4.2.3.1. Uniaxial compression values justification".

Furthermore, to clarify how uniaxial compression values arise on the plate, *Figure 36* and *Figure 37* are created:

Figure 36. Plate shortening for different amount of elements in the mesh

Figure 37. Out-of-plane deflection in the center of the plate for different amount of elements in the mesh

Notice that in *Figure 47*, out of plane deflection starts in 0.1 mm, this occurs because to carry out a simulation about post-buckling analysis, is necessary to introduce an imperfection on the plate.

Results using 1920 elements are quite similar to the 7680's ones, therefore, the best choice is compute the simulation with **1920 elements**.

4.2.3. Composite plies analysis for 2D models

- **Justification of the uniaxial compression values**

The difference that it was shown in the last section was around 20-25 MPa between them, in order to figure out why that occurs, it is interesting to present several path graphs from different plies of the plate. Plies number 1 and 14 are the most critical ones, therefore, they are shown in the next figures:

Comparison characteristics:

- 90 mm width → 3072 mesh elements
- 100 mm width → 7680 mesh elements
- $\sigma_{plate} = 250\ MPa$
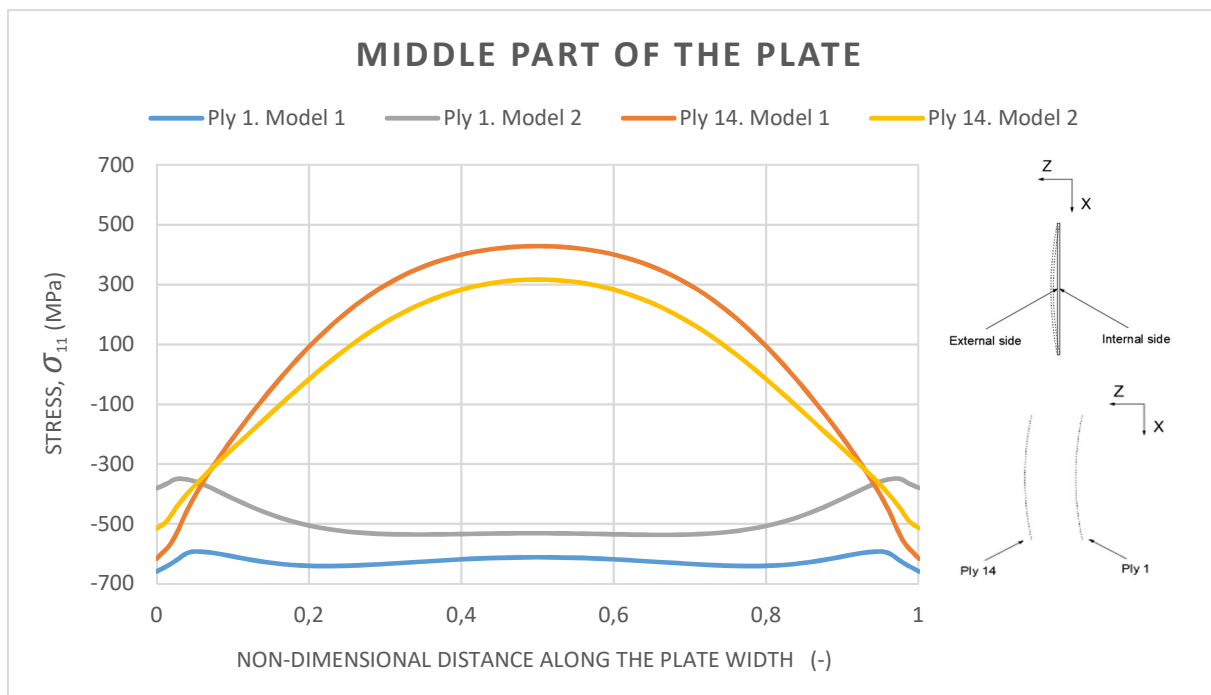
Figure 38. Stress curves comparison between Model 1 and Model 2 in fiber direction

Figure 38 shows in a clear manner that for the Model 2, the maximum compression stresses are lower than the ones from Model 1. That is to say, compression stresses from 100 mm need higher σ_{plate} values so that maximum σ_{11} values reach the material failure stresses.

- **Stress in the length direction plate (σ_{11})**

The middle section of the plate is the most critical because it is where the highest stress level is reached (when there is no friction behavior). Therefore, stresses in carbon fiber direction are only evaluated for this section.

- **Model 1** (3072 elements, $\sigma_{plate} = \mathbf{269,70\ MPa}$ – Plate rupture)
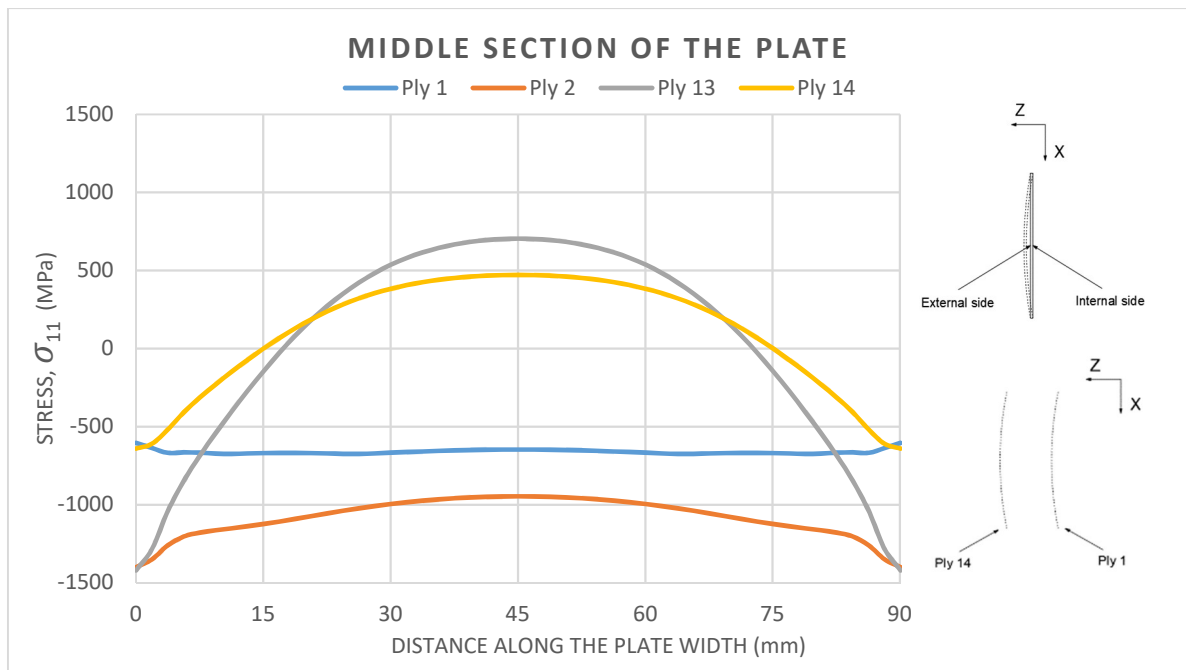
Figure 39. Stress comparison between the most critical plies from Model 1

Notice that plies 1 and 14 are composed by a woven distribution for the carbon fiber (orthotropic behavior). Therefore, as *Figure 39* shows, values reached are lower for those plies (they present less stiffness than the X-unidirectional fiber plies).

- **Model 2**. 100 mm width plate (7680 elements, $\sigma_{plate} = \mathbf{287,29\ MPa}$ – Plate rupture)
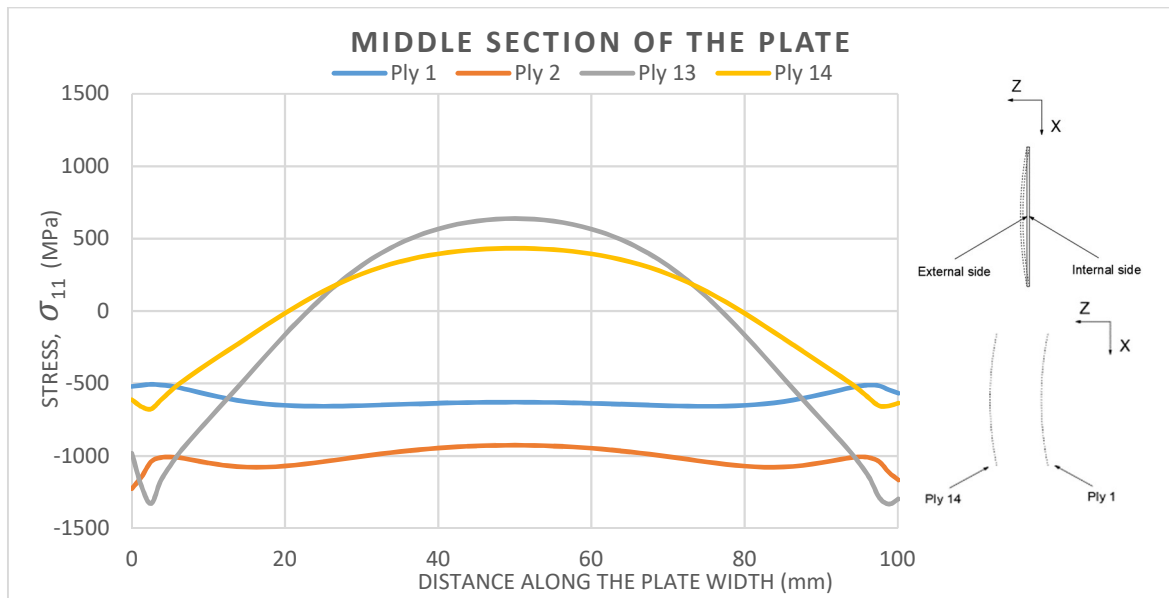
Figure 40. Stress comparison between the most critical plies from Model 2

In this case, as it can be observed in *Figure 39*, the stress values in the plate direction own a similar tendency as the values *Figure 40* have. Obviously, there are fixed edges

to 5 mm from each side of the plate, which create a local inclination change in the stress values. This appear because, those boundary conditions in the vertical edges (there is no displacement in out of plate deflection direction) introduce an additional stiffness in this area of the composite plate. It is not possible to know which ply is the first one to collapse, to observe that, Hashin's criteria has to be applied.

- **Hashin's criteria**

This point of the thesis has special interest because the first ply where the damage start can be predicted, as it was mentioned in section "2.3. Lamina failure criteria: Hashin". This criterion is computed for both widths of the composite plate in order to compare them.

- **Model 1**

For $\sigma_{plate} = 253,54\ MPa$ (First time Hashin's criteria = 1)
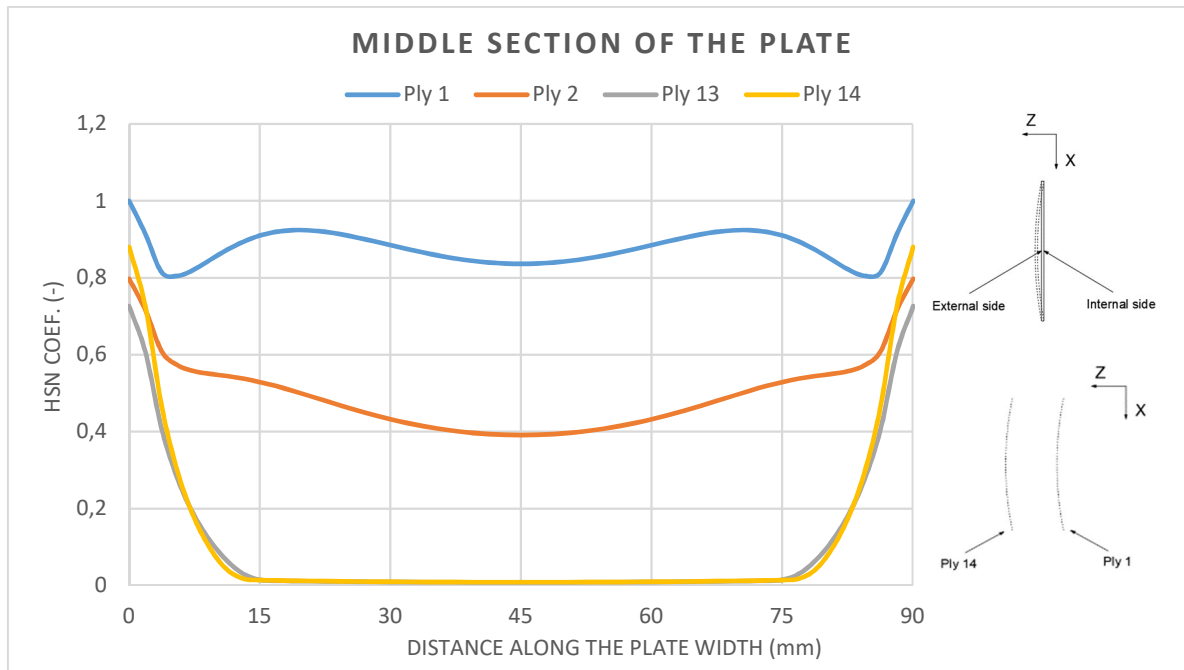
Figure 41. Hashin's criteria comparison between the most critical plies from Model 1

As it can be observed, ply number 1 is the first ply to reach the value of one when Hashin's criteria is applied, it means, ply 1 is where the damage starts in Model 1 laminate.

- **Model 2**

For $\sigma_{plate} = 262,66\ MPa$ (First time Hashin's criteria = 1)
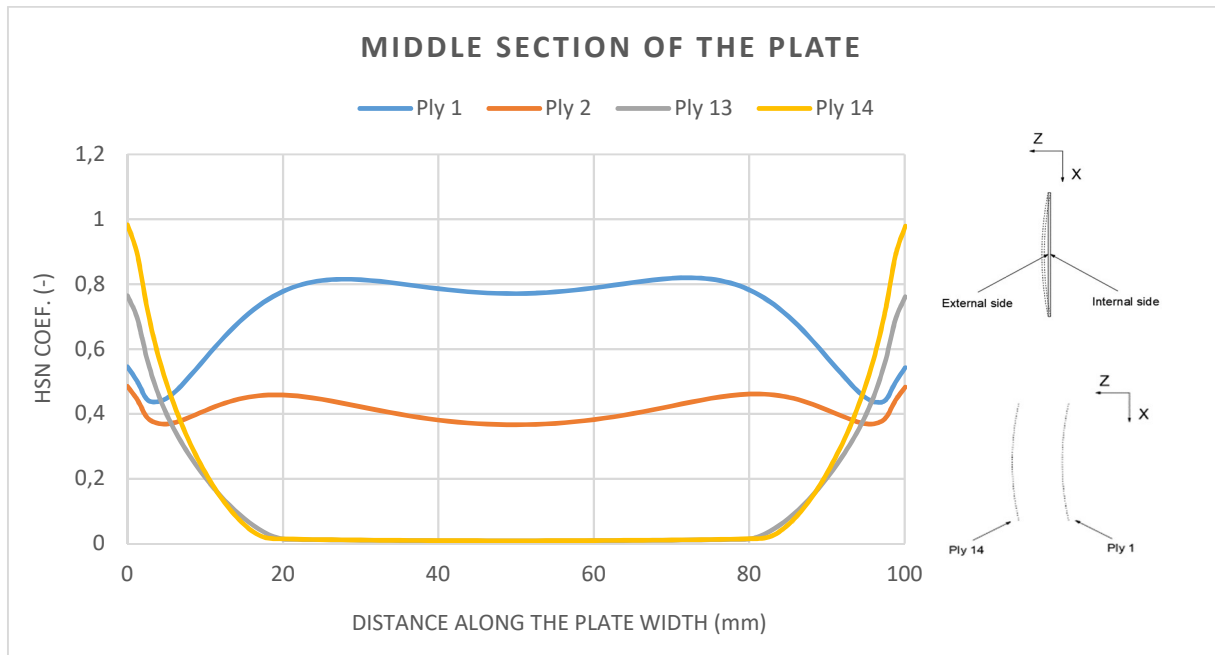
Figure 42. Hashin's criteria comparison between the most critical plies from Model 2

In contrast to Model 1, ply 14 is the first one to reach the unit value of Hashin's criteria; therefore, the damage starts in this ply.

To sum up, Table 15 is presented:

Plate Model	First ply damage initiation	Damage initiation	Failure values	Damage variation values	Failure variation values
[-]	[-]	[MPa]	[MPa]	[%]	[%]
Model 2	14	262,660	287,290	-	-
Model 1	1	253,540	269,700	3,472	6,123

Table 15. Damage and failure values comparison

- **Comparison models with different amount of elements in their mesh**

To observe the influence of the amount of mesh elements in Hashin's criteria coefficient, a graph for $\sigma_{plate} = 250$ MPa is given as follows:
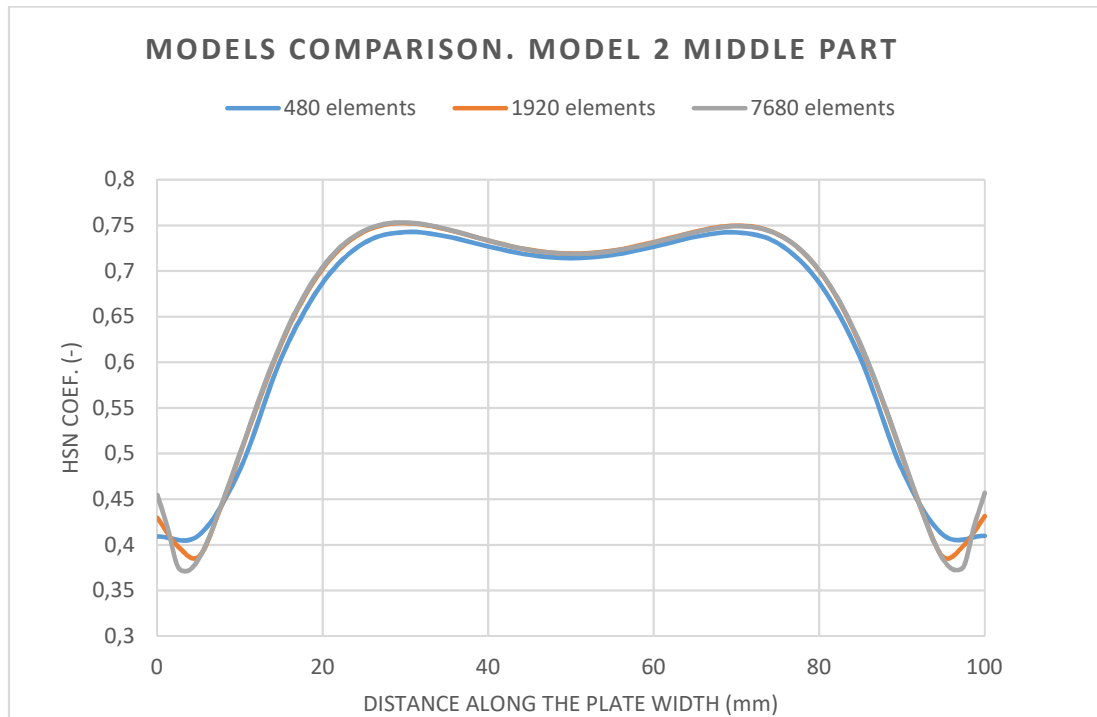
Figure 43. Hashin's criteria comparison between different meshes. Model 2

The amount of element selected describe (almost perfectly) the Hashin's criteria values reached by the green curve (7680 elements), this means that, in the case of HSN criteria, the mesh dependency study is also satisfied.

4.3.   Comparison between Model 2 and Model 4

After 2D models comparison, a thickness in the 2D shell model is applied (t = 2.132 mm) which means that 3D model are obtained. The main differences, as it is obvious, are caused by the thickness implementation in the plate because, the width distance is the same for both models (width = 100 mm). It is important to highlight that the 3D mesh stiffness is higher than the one from the 2D mesh.

4.3.1. Shortening and out-of-plane deflection

As follows, shortening and OoP deflection values are computed to illustrate the influence in these parameters when the thickness is applied in the sample:
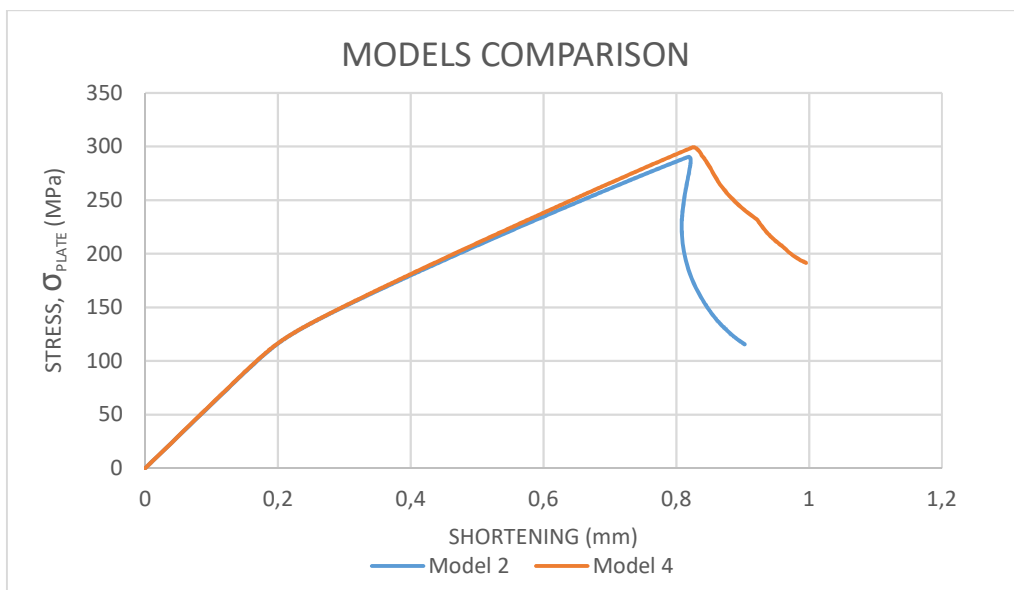
Figure 44. Plate shortening comparison between Model 2 and Model 4

Figure 45. Comparison of the out-of-plane deflection between Model 2 and Model 4

Shortening and OoP deflection that the plate suffers do not present a huge variation however; uniaxial compression value (applied on the upper part of the plate) is higher in the case of the 3D model, for both parameters visualized above. The values variation is mainly because of the higher thickness in the 3D mesh elements.

4.3.2. Hashin's criteria

Compression stress value, in which the graphs below are computed, is evaluated when Hashin's criteria coefficient reaches value 1 for Models 2 and 4, in plies 1 and 14.

- For $\sigma_{plate} = 262,66 \, MPa$ (First time Hashin's criteria = 1)
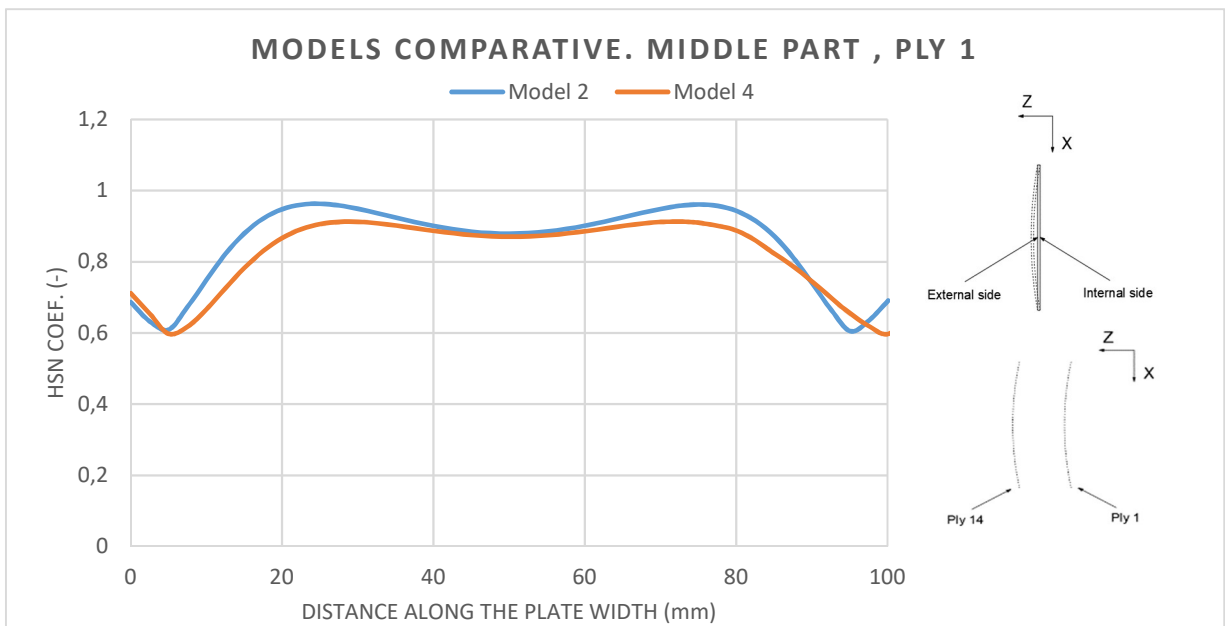
Figure 46. Hashin's criteria comparison between Model 2 and Model 4 for ply 1
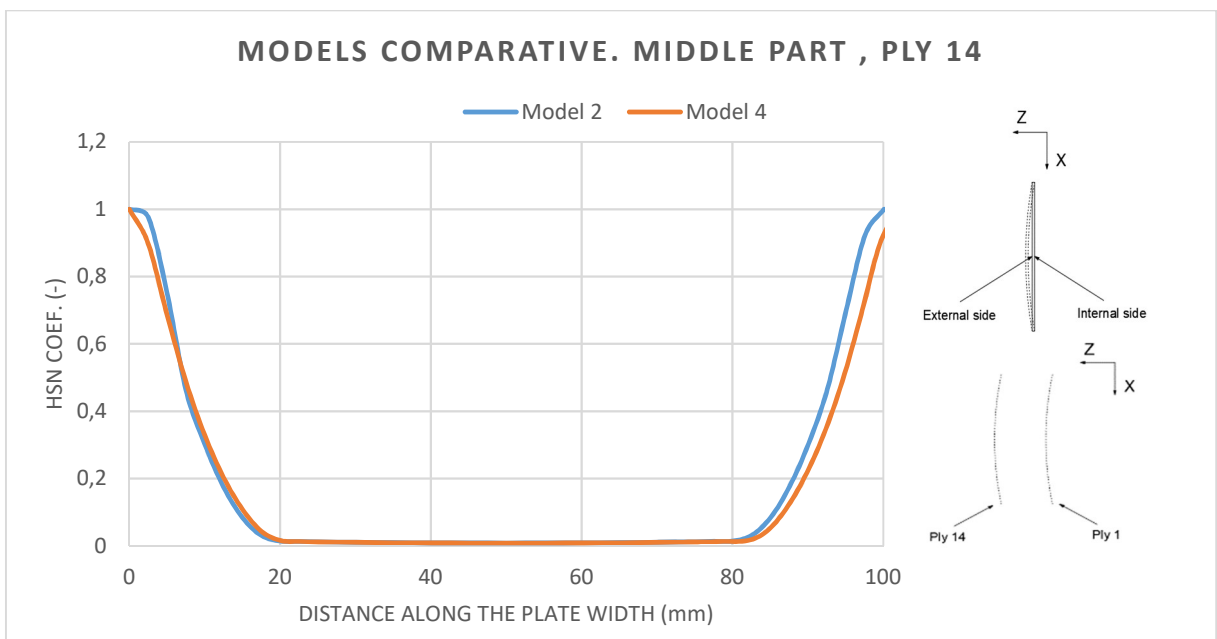
Figure 47. Hashin's criteria comparison between Model 2 and Model 4 for ply 14

Notice that in the case of Model 2, damage starts before the case of the Model 4 for both plies. It is because of the mechanical resistance from the 3D body, it is slightly higher than the shell model, as it was observed in *Figure 46* and *Figure 47*.

Concluding with this thesis section, a table with the main values is shown:

Model	Failure stress values [MPa]	Shortening [mm]	OoP Deflection [mm]	Variation Failure stress values [%]	Variation shortening values [%]	Variation Z deflection values [%]
2	290,370	0,819	5,487	-	-	-
4	299,370	0,828	5,721	3,099	1,099	4,265

Table 16. Summary table of the principal values for 2D and 3D models

4.4. Comparison between Model 4 and Model 5 (Mesh 1920 elements)

Several contact models between the plate and the lateral supports are compared. This analysis has been carried out for shortening and out of plane deflection parameters. The first figure for each parameter is about adaptation of different stiffness for the lateral support steel and, the second one, shows the variation between models with different mechanical properties and cross section shapes in their lateral supports.

4.4.1. Shortening and out-of-plane deflection

In *Figure 48* and *Figure 49*, the Young's modulus influence (from the lateral supports material) in the sample plate parameters is studied:
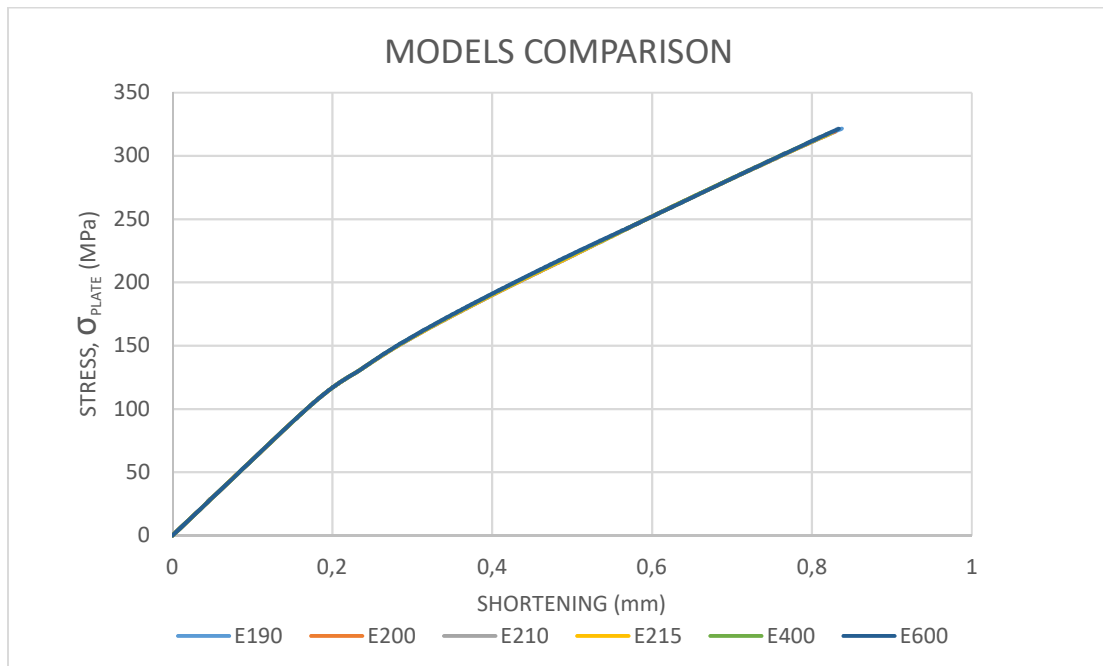

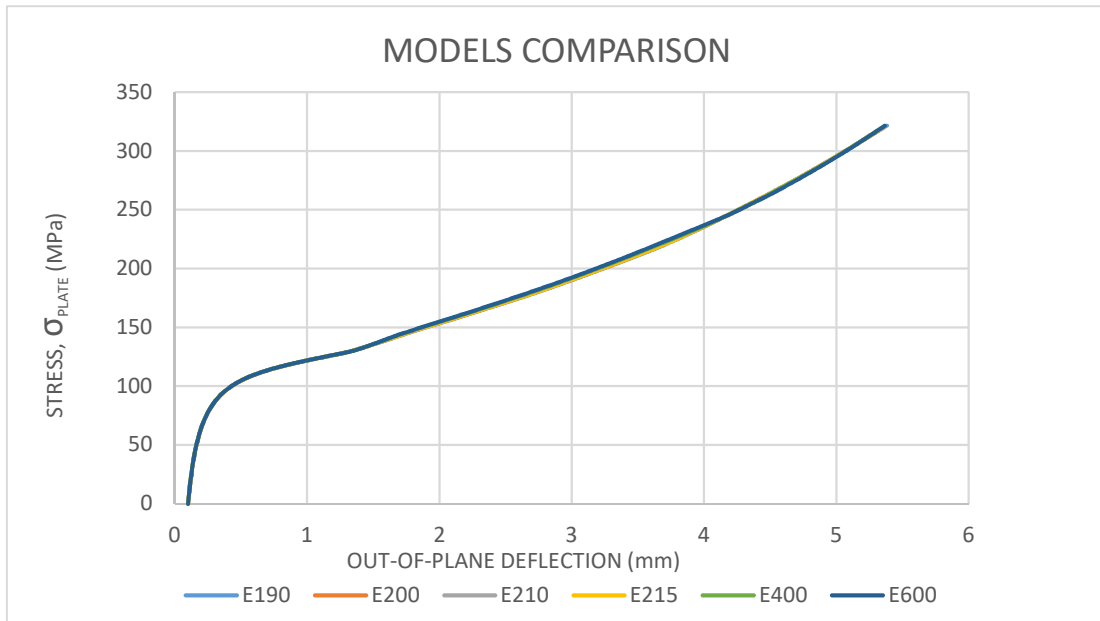*Figure 48. Shortening comparison between different Young's modulus values for the lateral supports*

Figure 49. OoP deflection comparison between different Young's modulus values for the lateral supports

Clearly, there is no a significant Young's modulus influence in the parameters analyzed. Therefore, if real Young's modulus value for the lateral supports is used (*E = 210 GPa*), results will be accurate. In addition, in order to select the most precise lateral support representation for the CAI device assembly, a comparison between several models is computed in the next graphs:
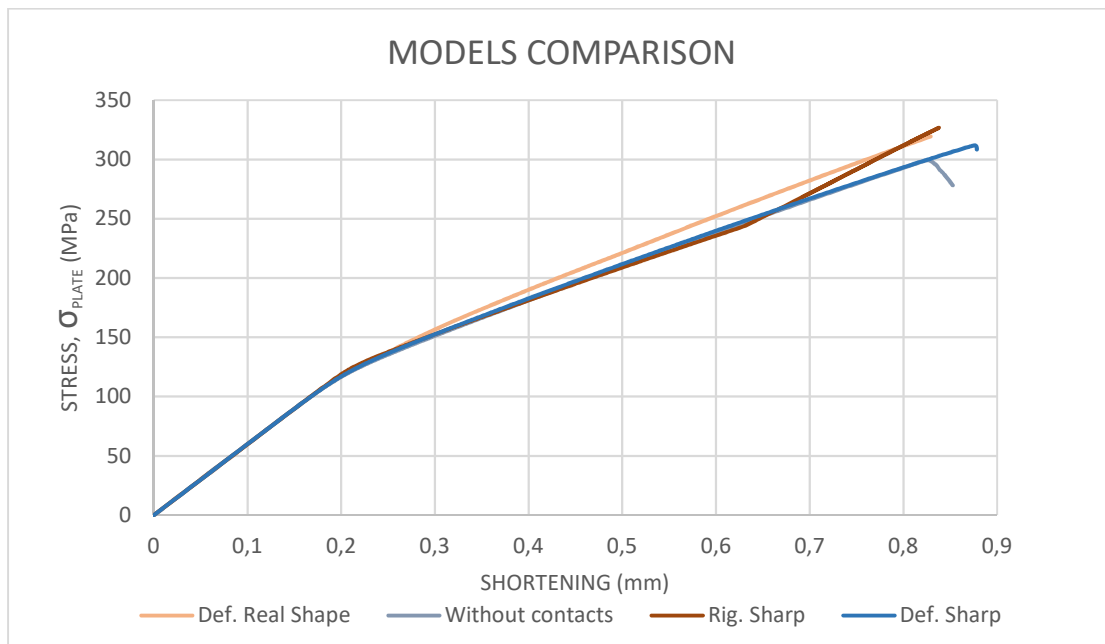

Figure 50. Shortening comparison between 3D models
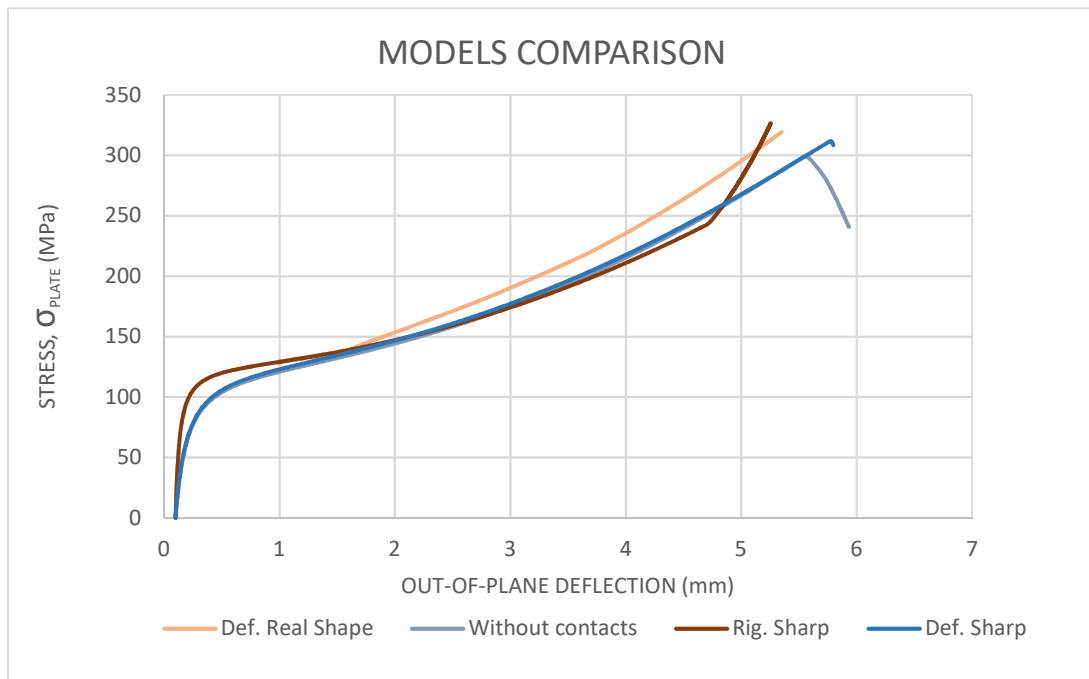
Figure 51. Comparison of the OoP deflection between 3D models

As it can be observed, the deformable sharp model has similarities in its values with the idealized model without contacts, for this reason, it will be consider as a lateral support model for the following simulations.

To sum up, a table is presented as a summary:

	Young's modulus, E [GPa]	Failure stress [MPa]	Shortening [mm]	Out-of-plane deflection [mm]	Variation Failure [%]	Variation shortening [%]	Variation Z deflection [%]
Non-Contact	-	**299,370**	**0,828**	**5,721**	-	-	-
Rigid sharp	-	250,445	0,638	4,699	16,343	22,947	17,864
Deformable sharp	**210**	**311,889**	**0,8750**	**5,6970**	**4,182**	**5,676**	**0,419**
Real deformable shape	210	318,228	0,8270	5,3330	6,299	0,121	6,782

Table 17. Summary table of the main values for 3D models of the CAI test device assembly

4.4.2. Distribution force on the section plate where the lateral supports are located

To ensure that, a proper lateral support model for the CAI device is developed, it is necessary to obtain the force distribution along the plate in the area where those are located (5 mm per each side). Moreover, to reproduce an accurate representation, the force distribution has to be similar for every model described in this section of the project.
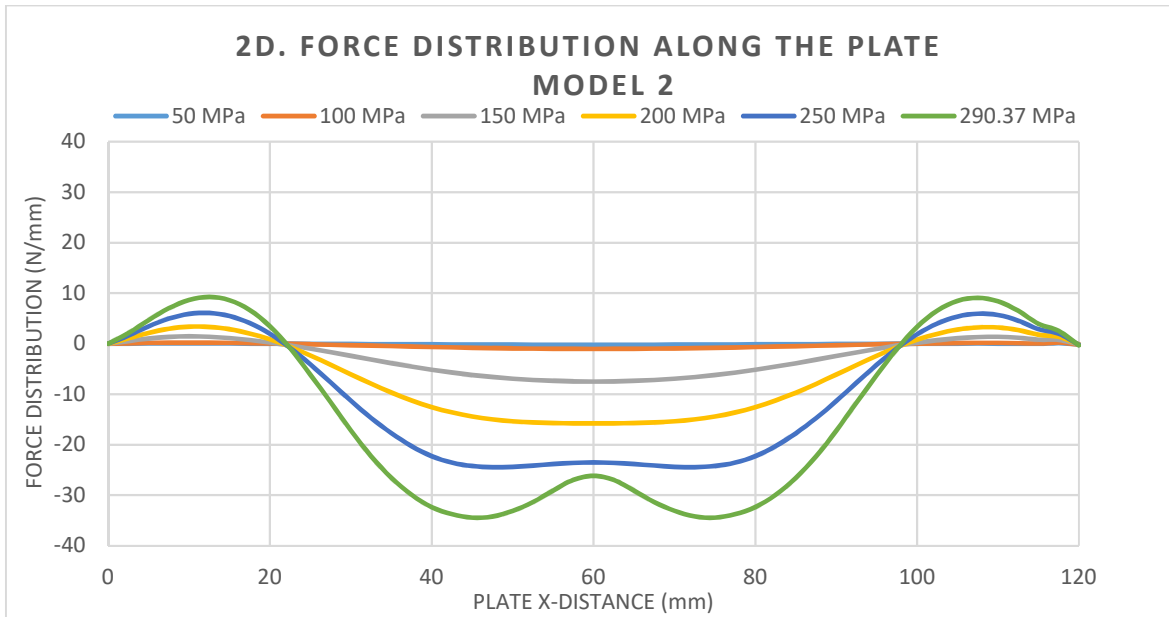
- 2D PLATE MODEL

Figure 52. Reaction force distribution along the X-distance in 2D model plate. Model 2
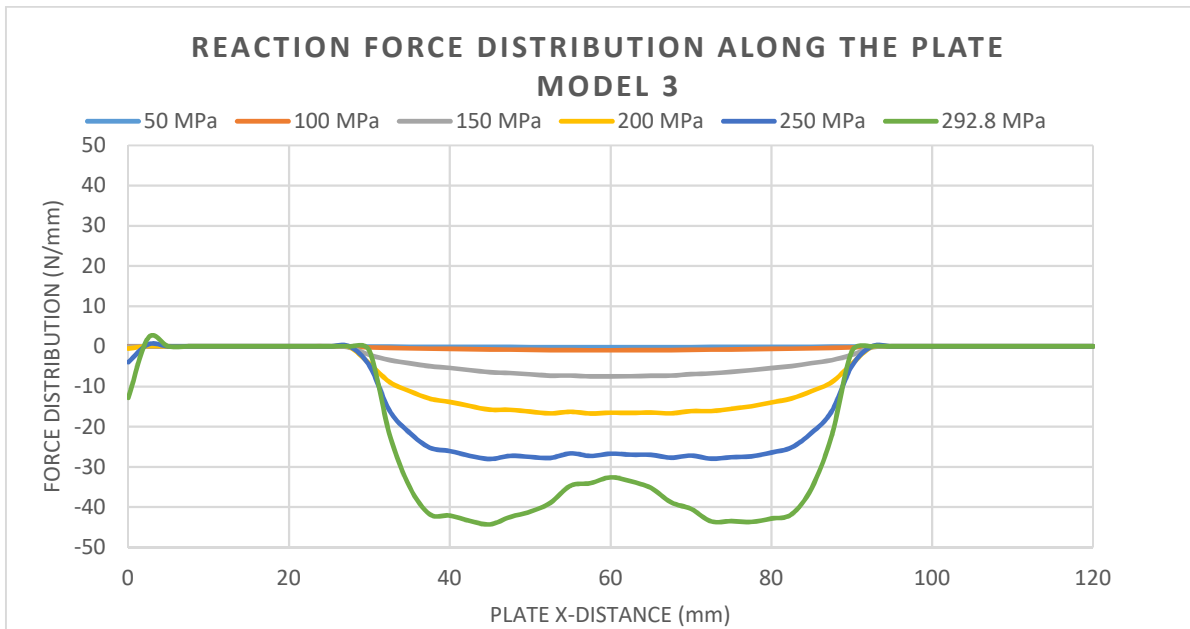
Figure 53. Reaction force distribution along the X-distance in 2D model plate. Model 3

In the *Figure 53*, the force distribution is reproduced for only the external side of the plate due to the difficulties found to define a proper contact between the plate and the lateral supports.

Comparing values for 200 and 250 MPa as reaction force (compression stress test) for both models:
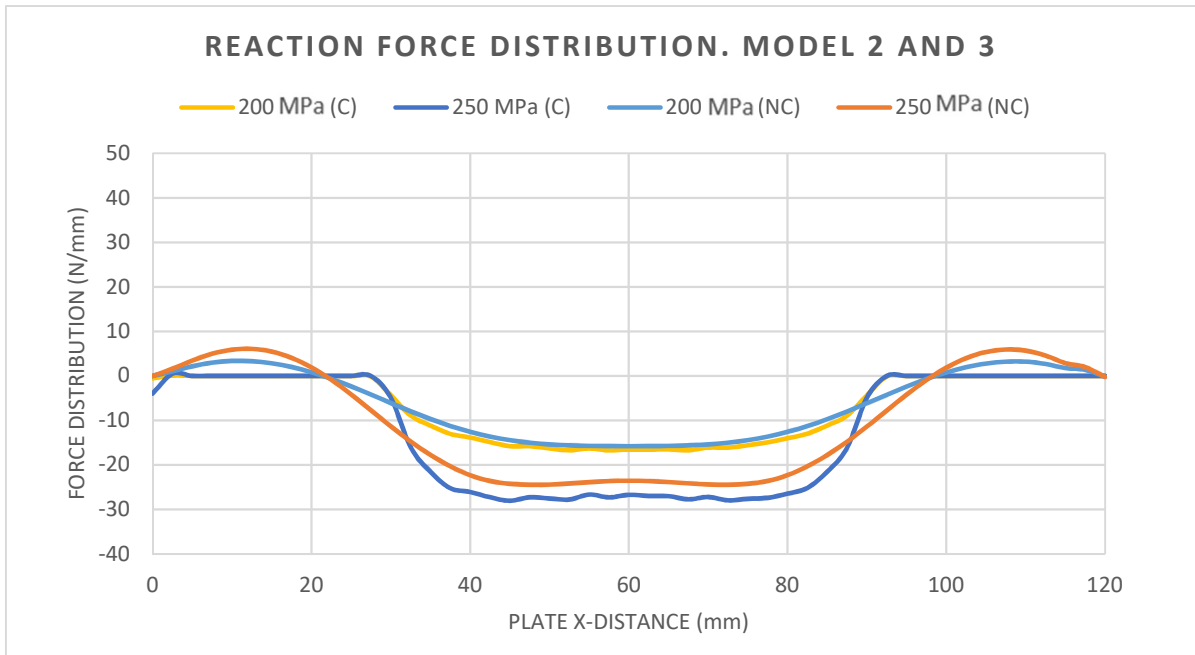
Figure 54. Reaction force distribution along the X-distance. 2D Models comparison.

- **Comparison models with different amount of elements in their mesh**

As in HSN criteria section, the influence of the amount of mesh elements is also analyzed for the force distribution along X-plate distance. Therefore a graph for $\sigma_{plate} =$ 250 MPa is given as follows:
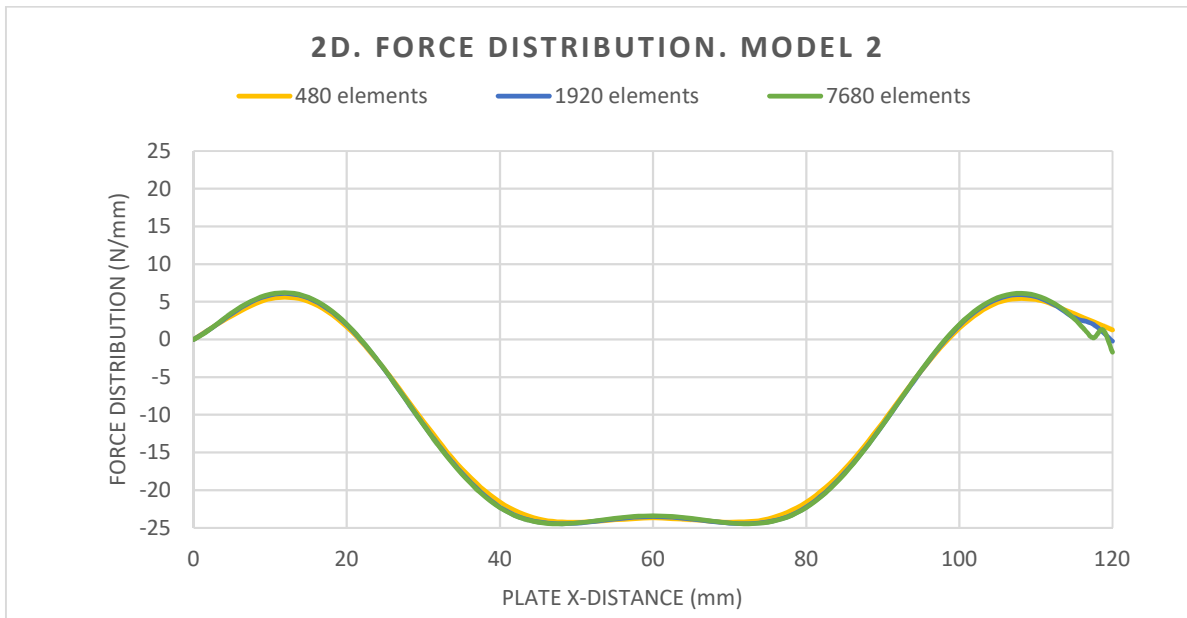

Figure 55. Force distribution comparison between different meshes. Model 2

As *Figure 55* shows, there is not a significant variation between the force distributions values when different meshes are used, complying with the mesh dependence study carried out at the beginning of this chapter.

- 3D PLATE MODEL (THICKNESS MODELED)

Force distribution analysis along the length plate distance are vitally important to ensure that, the designed model, meets the requirements for the future comparisons with the real model tested in the laboratory.

Figure 56 shows the different sections and sides of the plate. Those parts are going to be named throughout this point. Notice that each lateral support will be located 5 mm from the nearest corner of the plate.
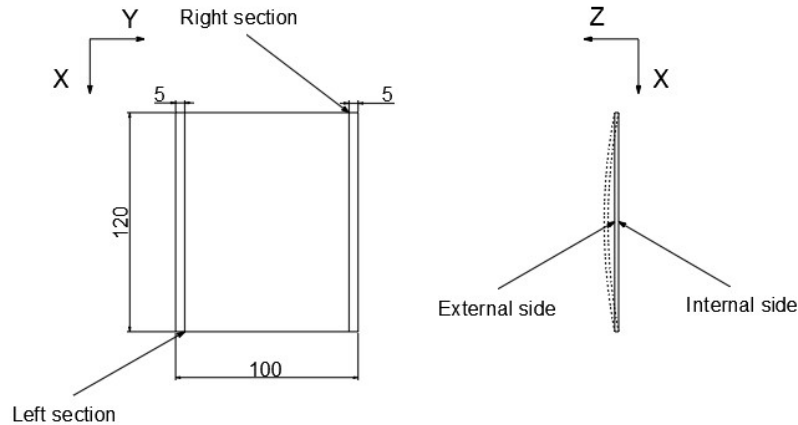

Figure 56. Sketches about location of each section and side on the sample plate (dimensions in mm)

Along this subchapter only the results from the right section of the plate will be computed, for this reason, it is essential to probe that there is symmetry in the values reached in both sections. This demonstration can be found along next subchapter.

- **Graphs from each side of the right section plate**

MODEL 4

First, a symmetry justification is needed because in the follow computation, only the results from the right side of the plate are going to be analyzed.
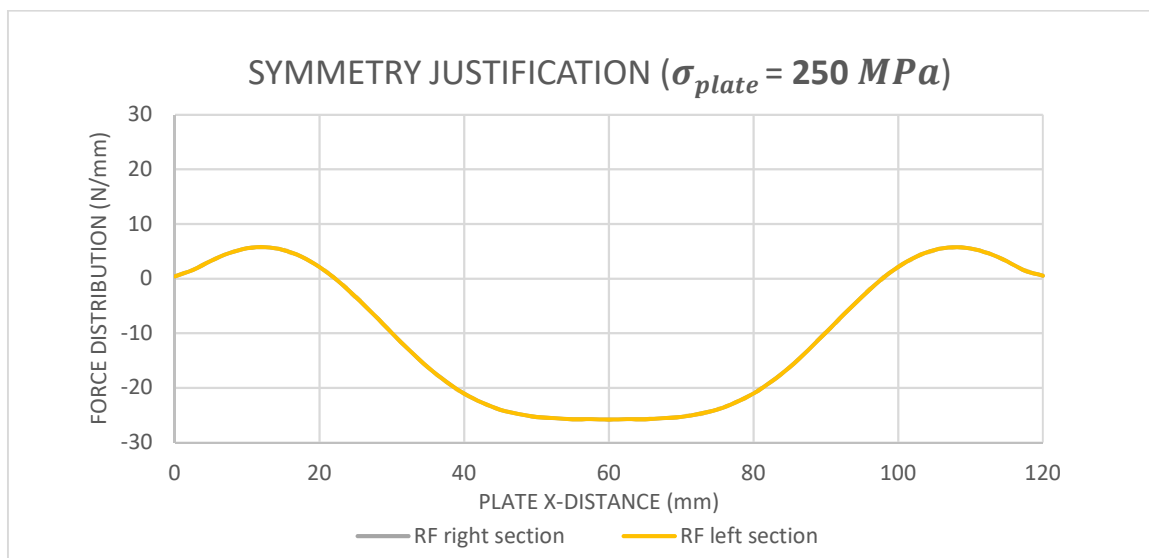

Figure 57. Symmetry justification. Force distribution, sum of external and internal side. Model 4

As *Figure 57* shows, the force distribution is identical for both section sides; therefore, symmetry in this model is verified.
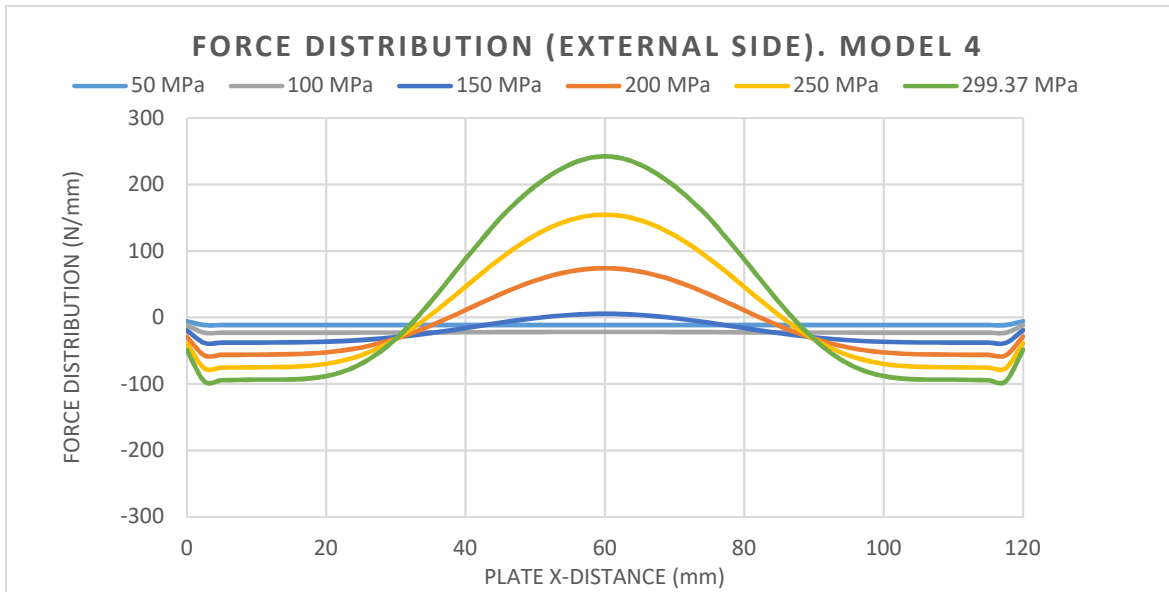

Figure 58. Reaction force distribution along the X-distance in the external side of the plate. Model 4
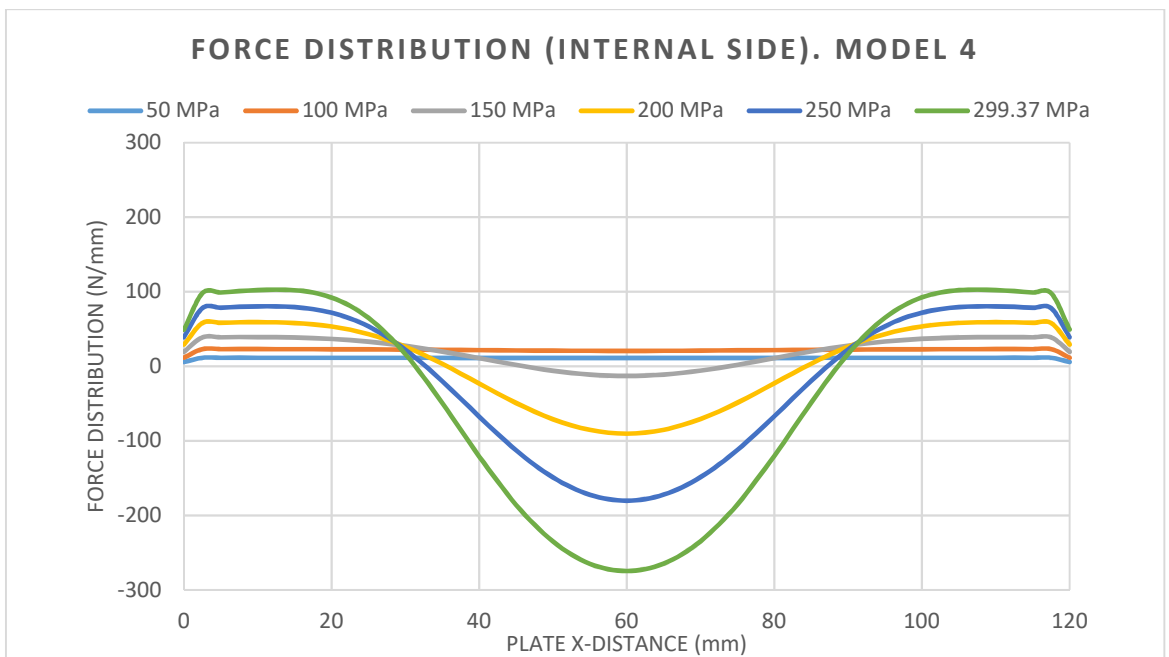

Figure 59. Reaction force distribution along the X-distance in the internal side of the plate. Model 4

As it can be seen on the two graphs above, there is a change in the force values sign along the X-distance plate. It is due to the tensile force appear in the lower and upper part of the plate when it is blending. The mesh nodes in the non-contact model has its displacement fixed in the force direction, that is the reason why the nodes produce a force in the opposite direction, in order to counter the tendency to displacement from those nodes. However, the maximum force value is reached in the middle of the sample where compression force appears.

MODEL 5

As in the case of Model 4, the force distribution is also the same for both section sides, as it can be observe in the figure below:
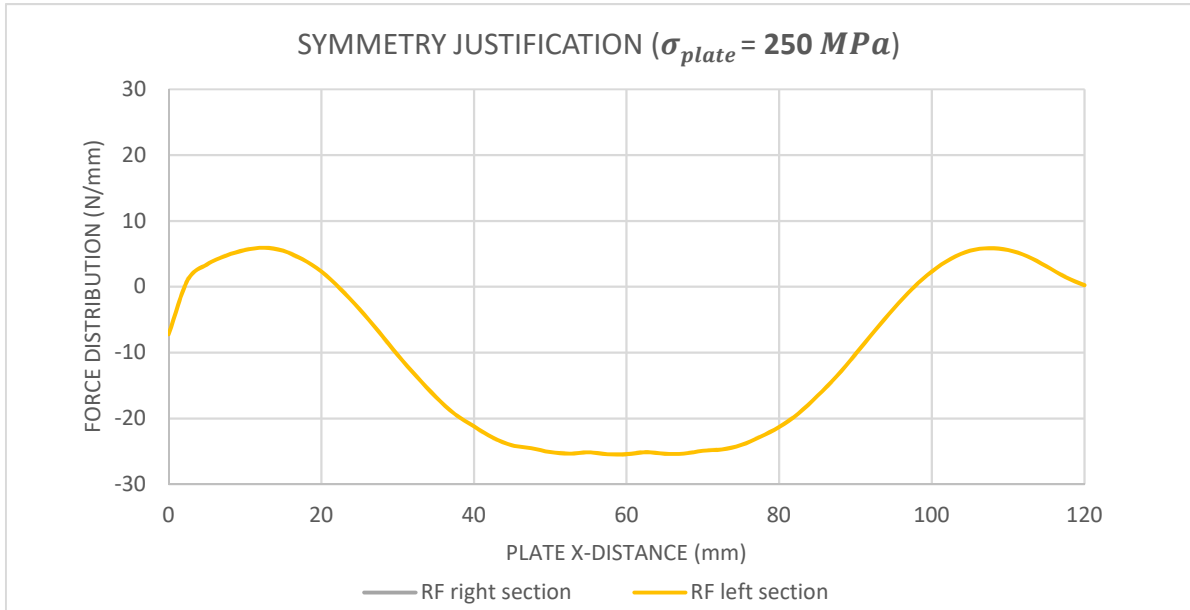

Figure 60. Symmetry justification. Force distribution, sum of external and internal side. Model 5
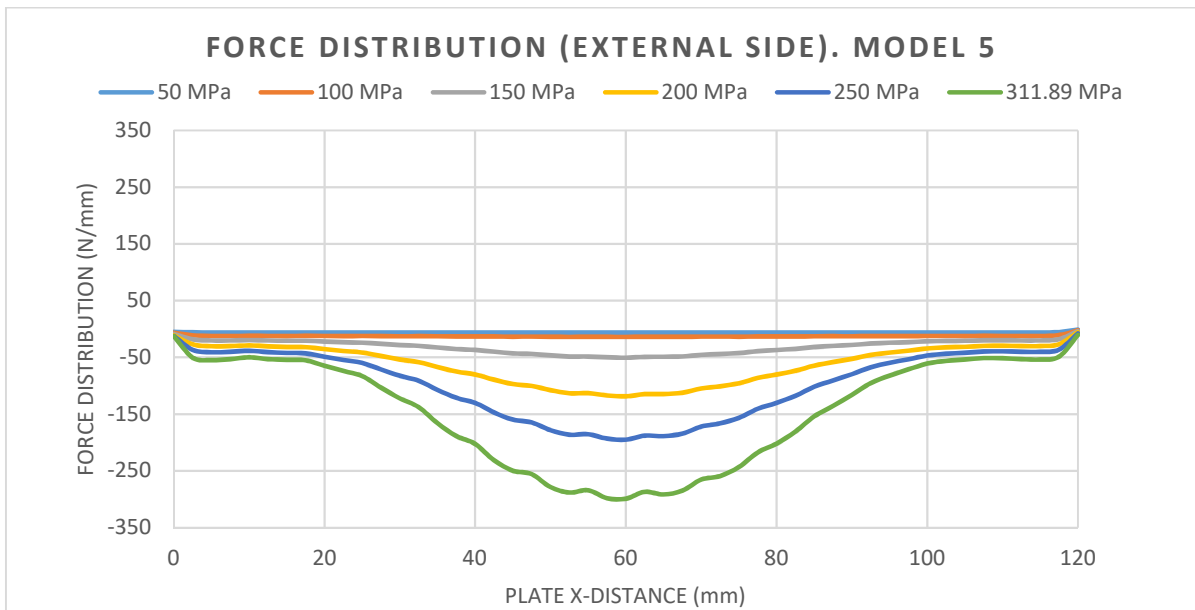

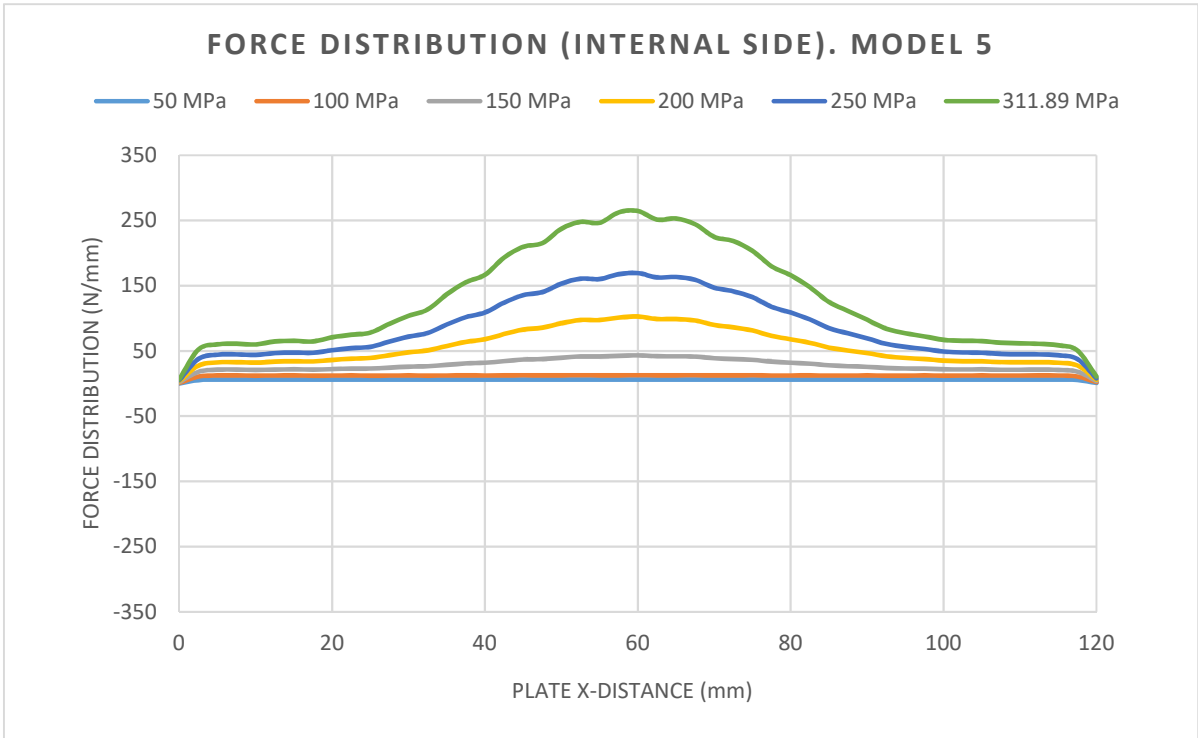*Figure 61. Reaction force distribution along the X-distance in the external side of the plate. Model 5*

Figure 62. Reaction force distribution along the X-distance in the internal side of the plate. Model 5

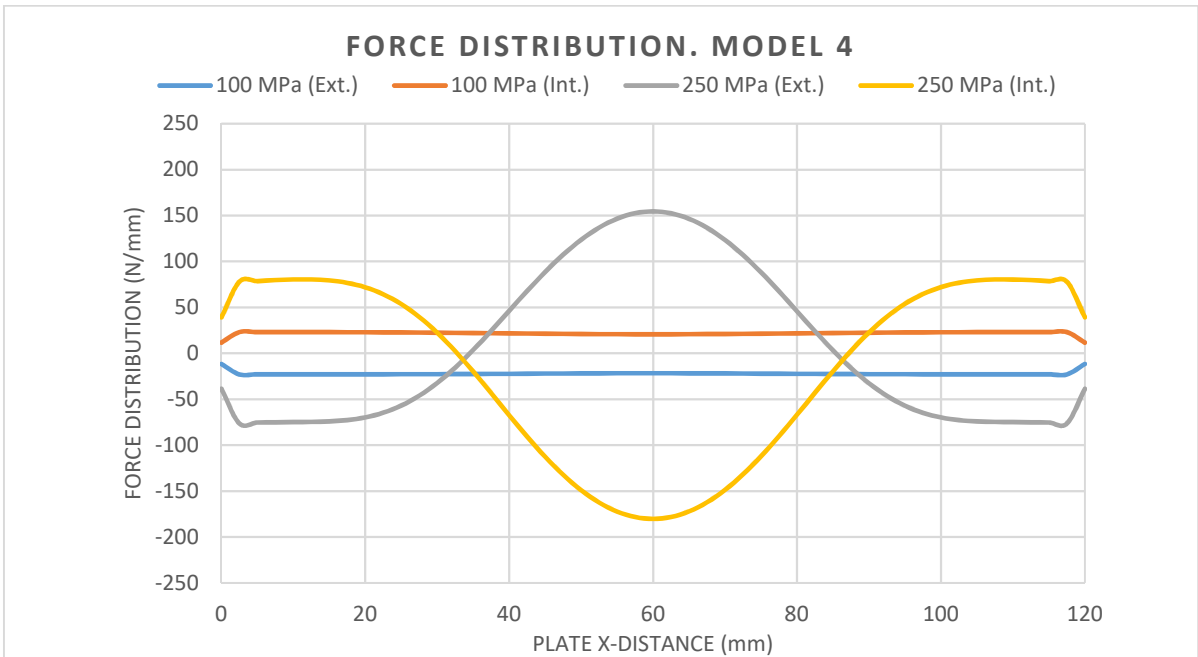- **Comparison between different plate sides**

Figure 63. Evolution of force distribution in both sides of the plate. Model 4
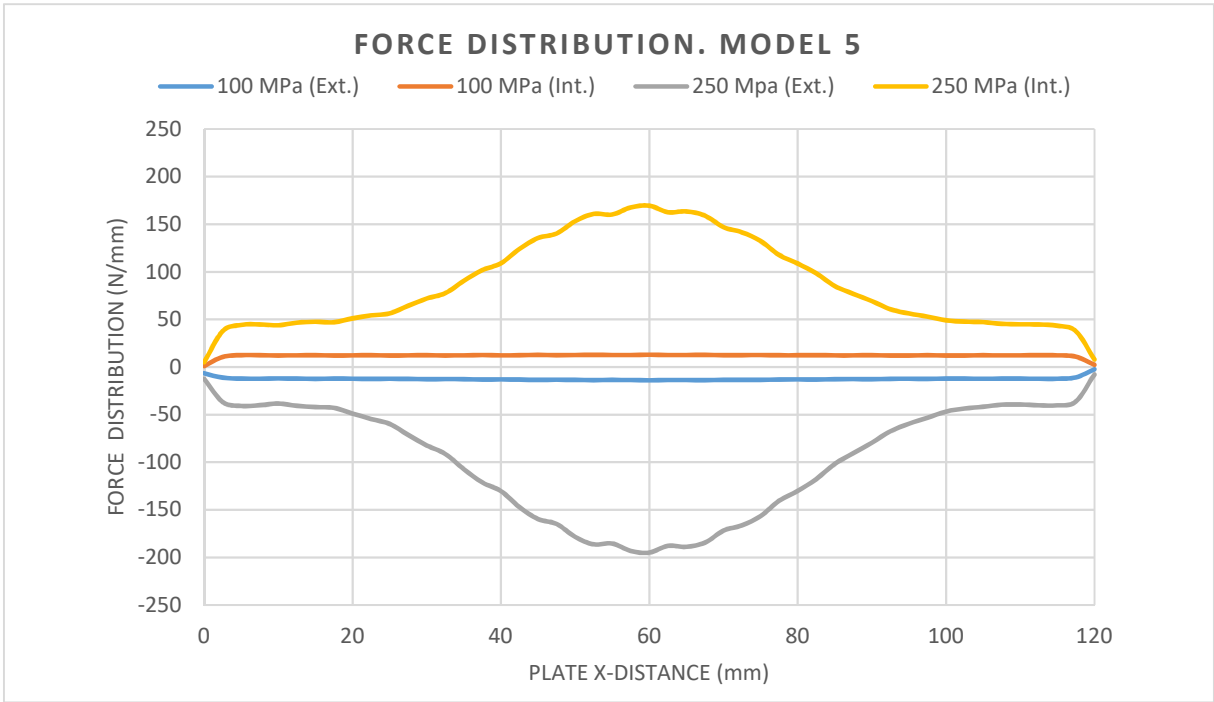
Figure 64. Evolution of force distribution in both sides of the plate. Model 5

Notice that both models reach similar values, however the ones from the contact models will always have the same sign, otherwise there is no contact between the plate and the LSs (compression behavior).

- **Graphs from the sum of both sides of the plate**

To come to the results from the graphs below, force distribution in the internal and the external side of the plate are taken into account, according to *expression 87*:

$$Force_{ext} + Force_{int} = Total\ Force \qquad [87]$$

This total force is computed for each X-plate-distance (different force values are reached):
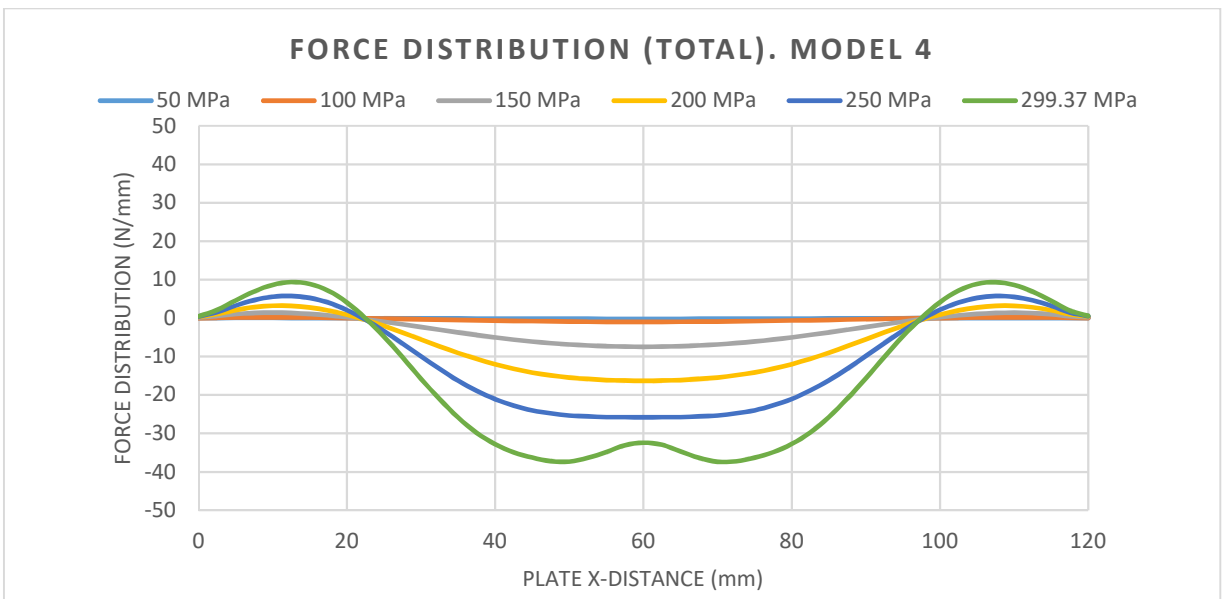

Figure 65. Sum of the force distribution from both sides of the plate. Model 4
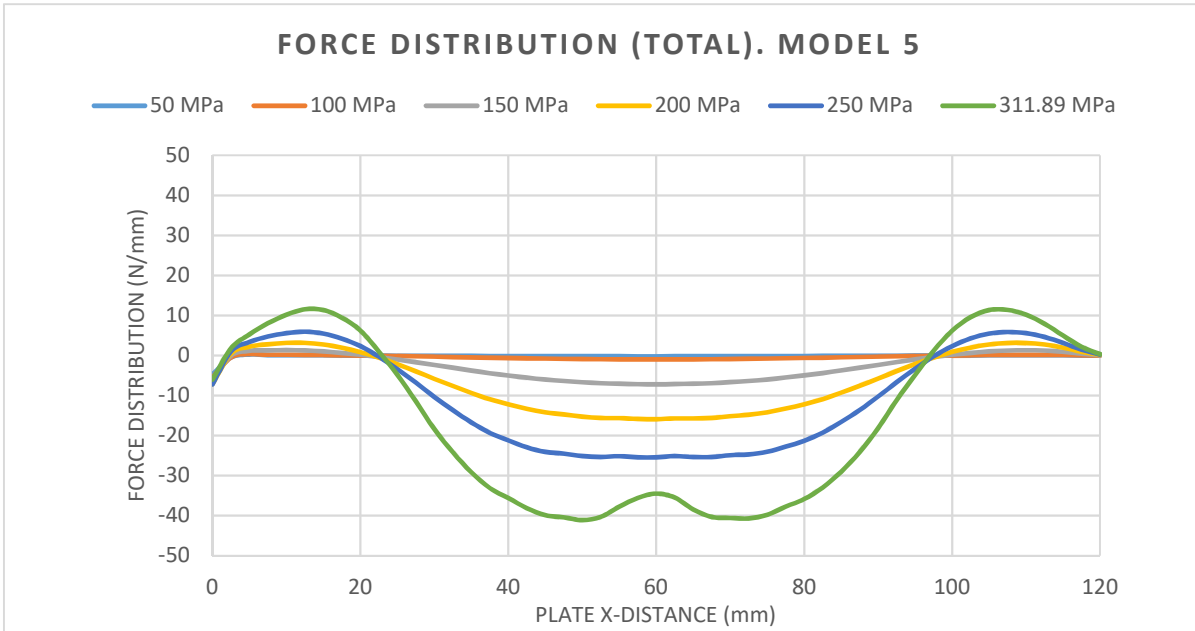
Figure 66. Sum of the force distribution from both sides of the plate. Model 5

Comparing values for 200 and 250 MPa as reaction force (compression stress test) for both models:
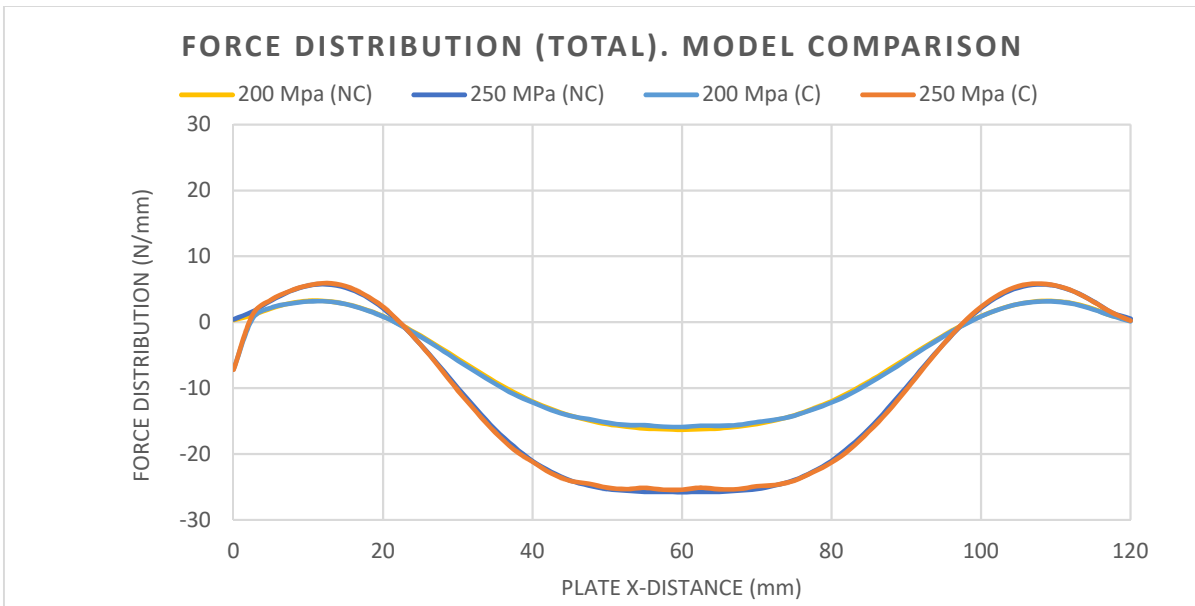

Figure 67. Force distribution comparison. Model 4 and 5

Where (C) means contact and (NC) non-contact model.

- COMPARISON BETWEEN THESE TWO 3D MODELS

As a summary, the table below shows the reaction force (only for the right section plate) when the sample starts the rupture:

Model	Reaction force (N)	Variation (%)
MODEL 4	35892,01	-
MODEL 5	33418,50	6,89

Table 18. Total reaction force produce by LSs. Model 4 and 5

It can be noticed that in *Table 18*, the variation between reaction values from both models is 6,89 %. It represents the accuracy that Abaqus has when the contacts between these bodies are considered.

- FORCE DISTRIBUTION. COMPARISON BETWEEN MODEL 2 AND 4
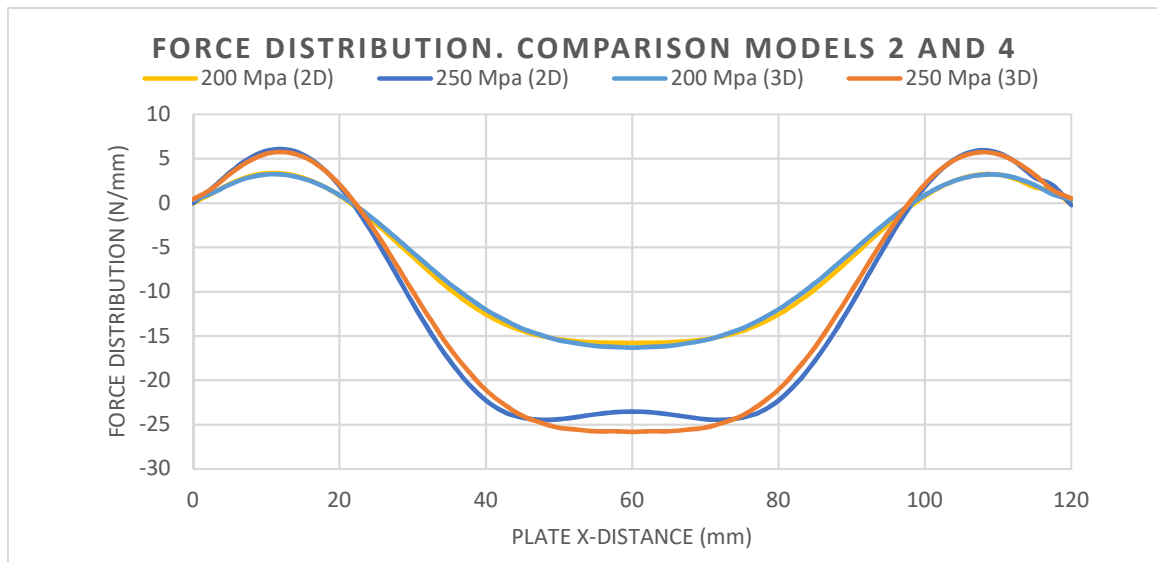
MODELS 2 AND 4

Figure 68. Distribution force. Comparison between models 2 and 4
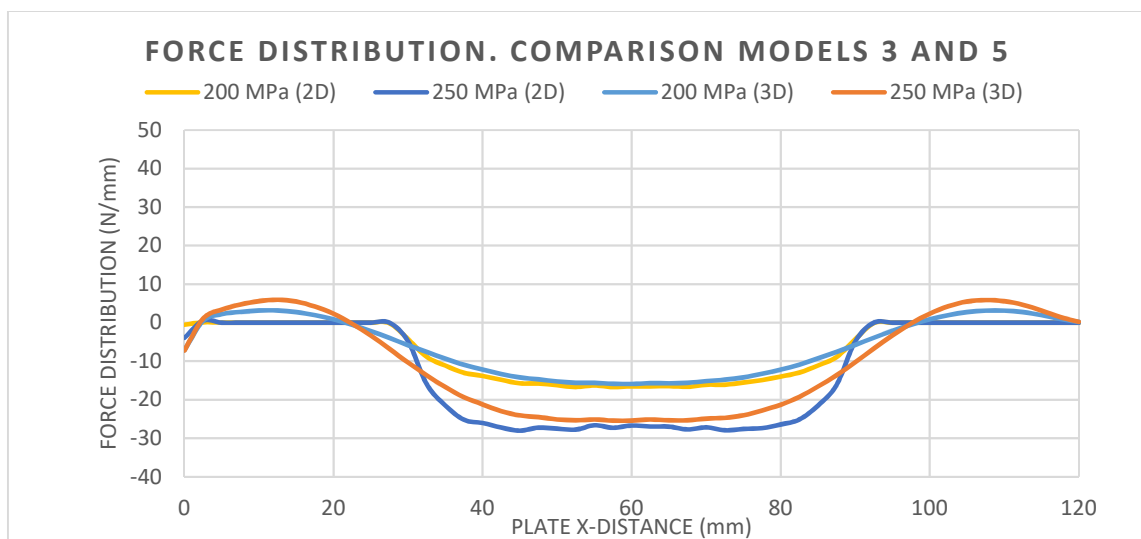
MODELS 3 AND 5

Figure 69. Distribution force. Comparison between models 3 and 5

4.5. Lateral support screws modeled as connector elements

Along this subchapter, a comparison between Model 5 and Models 6.1, 6.2, 6.3 is realized, in order to notice the influence in the assembly FE-model when screws are modeled as connector elements. As in subchapters above, characteristic parameters from CAI test are presented. Description of each model can be found in Chapter 3, however it is essential to mention that for Model 6.3 (connectors with a preload applied) satisfies *expression 88*:

$$F_B = 2{,}54 \; kN \qquad\qquad [88]$$

Where F_B is the absorbable operating force from screw (value taken from [7], see *Figure 70*)
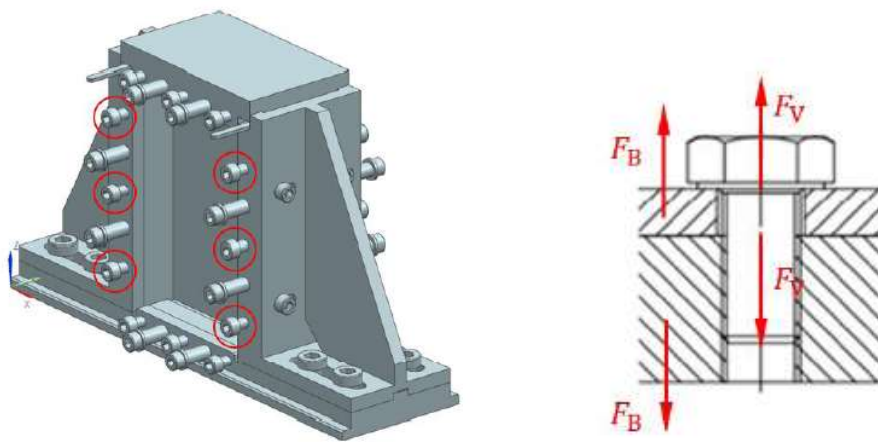

Figure 70. Location of the screws on the CAI device frame (left), acting loads on screw (right) [3]
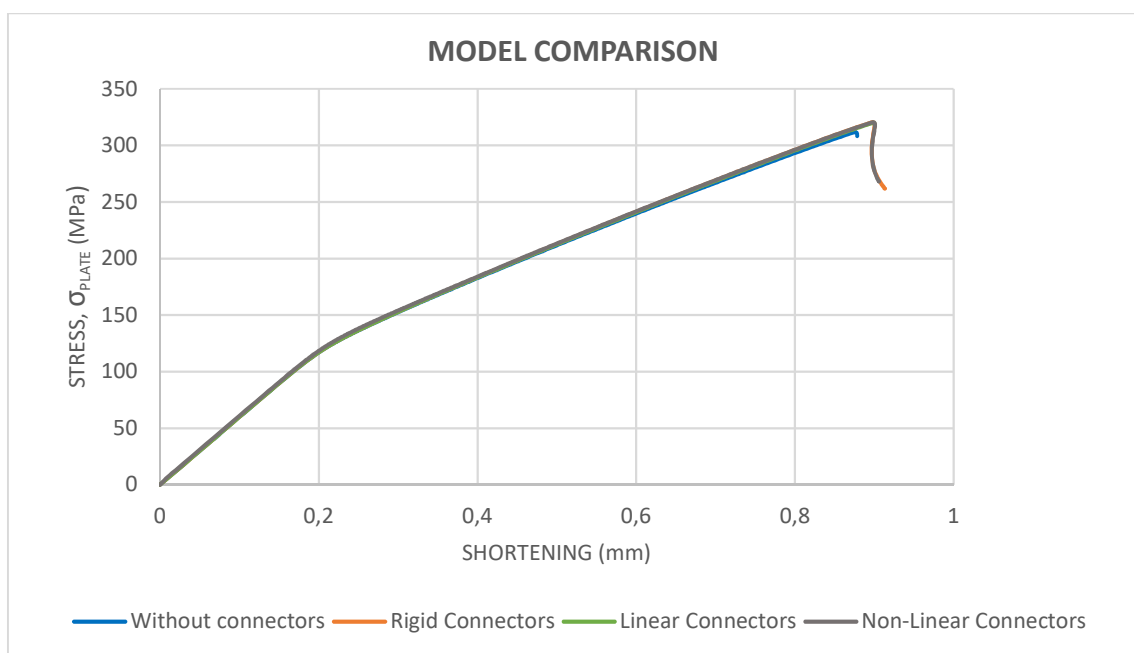
4.5.1. Shortening

Figure 71. Shortening values comparison between models with and without connectors

In the case of shortening of the plate, there is no a huge variation between all the models. Model without connectors presents the biggest value variation, however it is still close to the values from the models with connectors.

4.5.2. Out-of-plane deflection

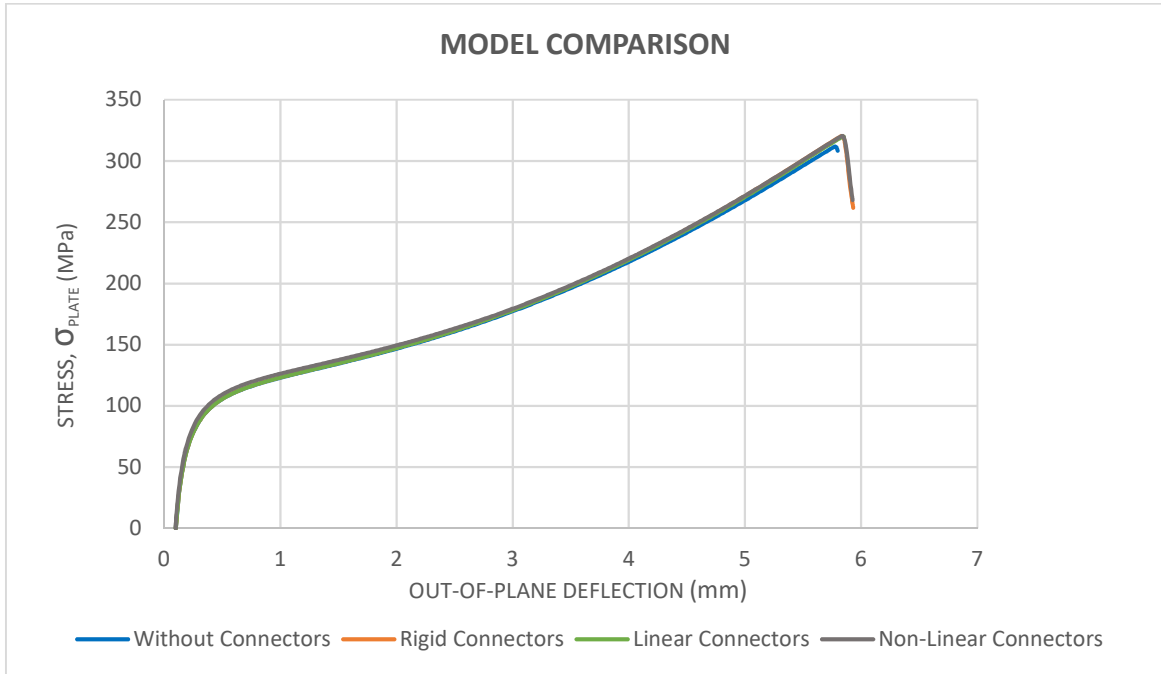*Figure 72. OoP values comparison between models with and without connectors*

OoP deflection values follow the same tendency than in the shortening case (there is no a considerable variation in the values between the models).

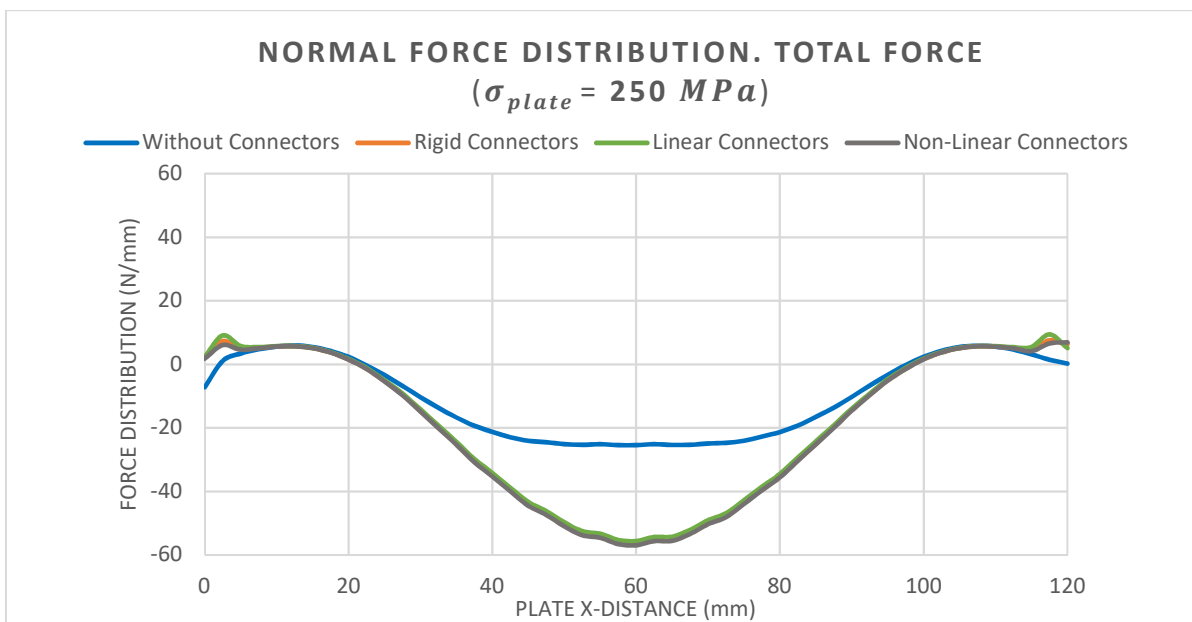### 4.5.3. Normal force distribution (OoP deflection direction)

Figure 73. Normal force distribution along the plate X-distance between models with and without connectors

Reaction force distribution (OoP deflection direction) is almost identical for connector models, however, there is a significant force values decreasing for the case of model without connectors. This occurs because Model 5 does not present any force applied on the LSs, however the Models with connectors present acting forces due to the screw connections.

4.6. Friction behavior modeling

In this subchapter, friction behavior is applied for Model 5, Model 6.1, Model 6.2 and Model 6.3. To observe the influence of friction while CAI test is carried out, it is essential to study the characteristic values from the specimen, as it has been made along this chapter. Shortening and OoP deflection of the sample plate can be found in all the sections below, however, due to friction coefficient between steel and CFRP is approximately 0.3, it is interesting to analyses in a deeply manner this subchapter in order to obtain realistic results. For this reason, a study of friction influence on the reaction force distribution (where sliding edge is located) will be carried out.

In addition, only reaction force from 3D plate models will be computed because, the differences between 2D and 3D models are already analyzed. The reaction force computed is evaluated for $\sigma_{PLATE} = 250 \; MPa$.

4.6.1. Friction Coefficient = 0.1

- **SHORTENING**

Figure 74. Shortening values comparison between models with and without connectors. Friction Coef.=0.1

- **OUT OF PLANE DEFLECTION**

Figure 75. OoP values comparison between models with and without connectors. Friction Coef.=0.1

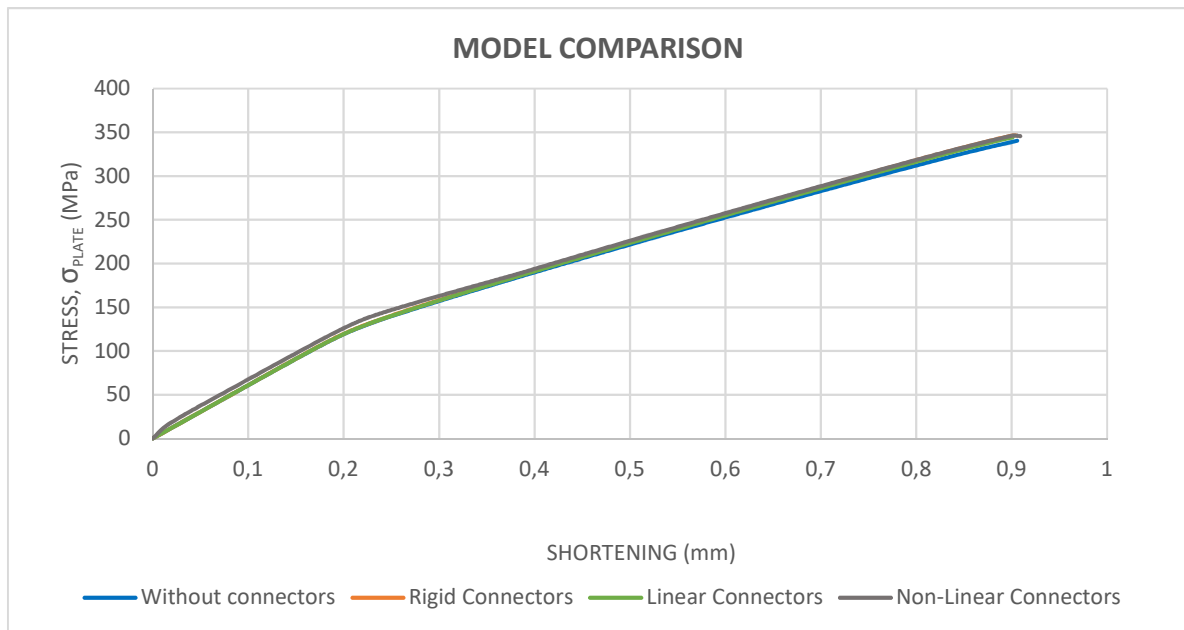## 4.6.2. Friction Coefficient = 0.3

- **SHORTENING**

Figure 76. Shortening values comparison between models with and without connectors. Friction Coef.=0.3

- **OUT OF PLANE DEFLECTION**
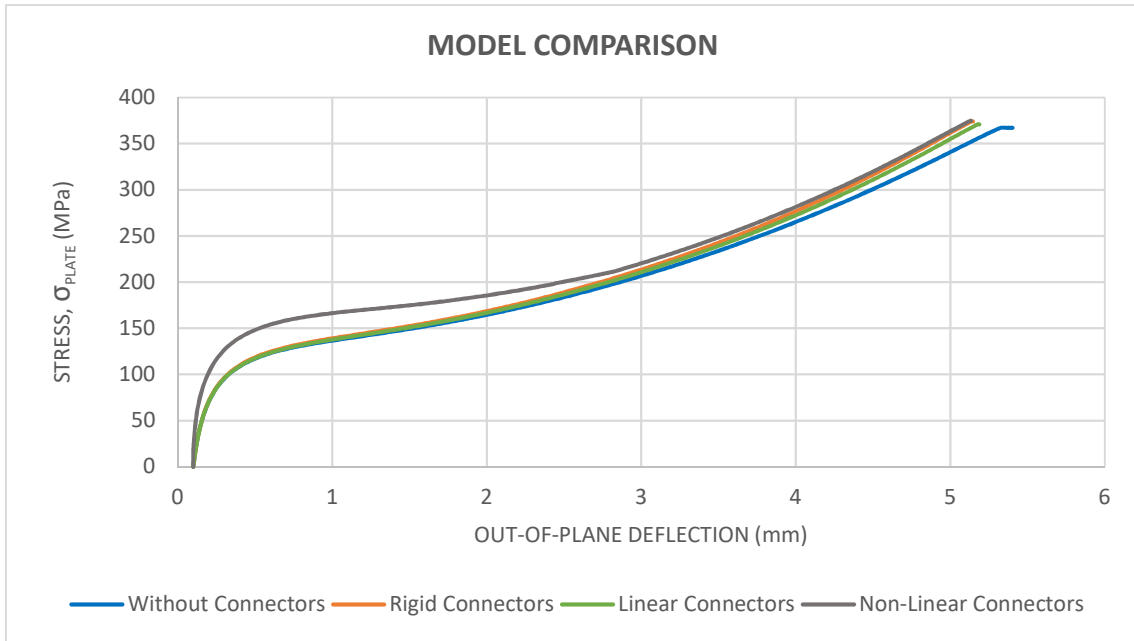
Figure 77. OoP values comparison between models with and without connectors. Friction Coef.=0.3

- **NORMAL FORCE DISTRIBUTION**
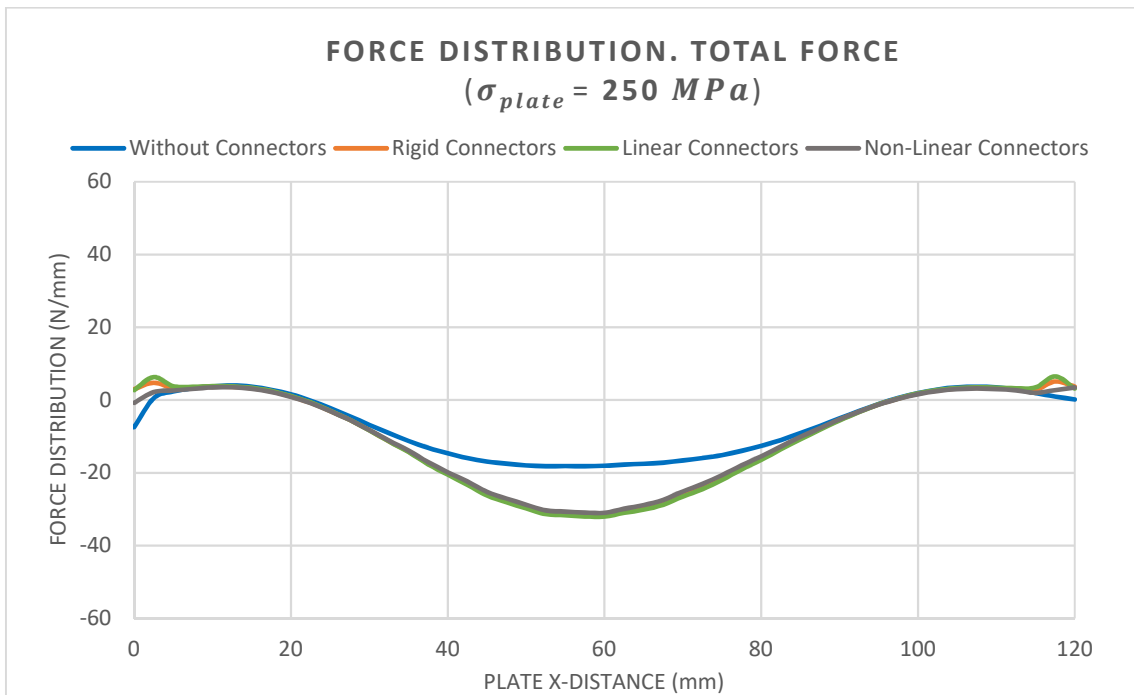
Figure 78. Comparison of normal force distribution between models with and without connectors. Friction Coeff.=0.3

- **SHEAR X-FORCE DISTRIBUTION**
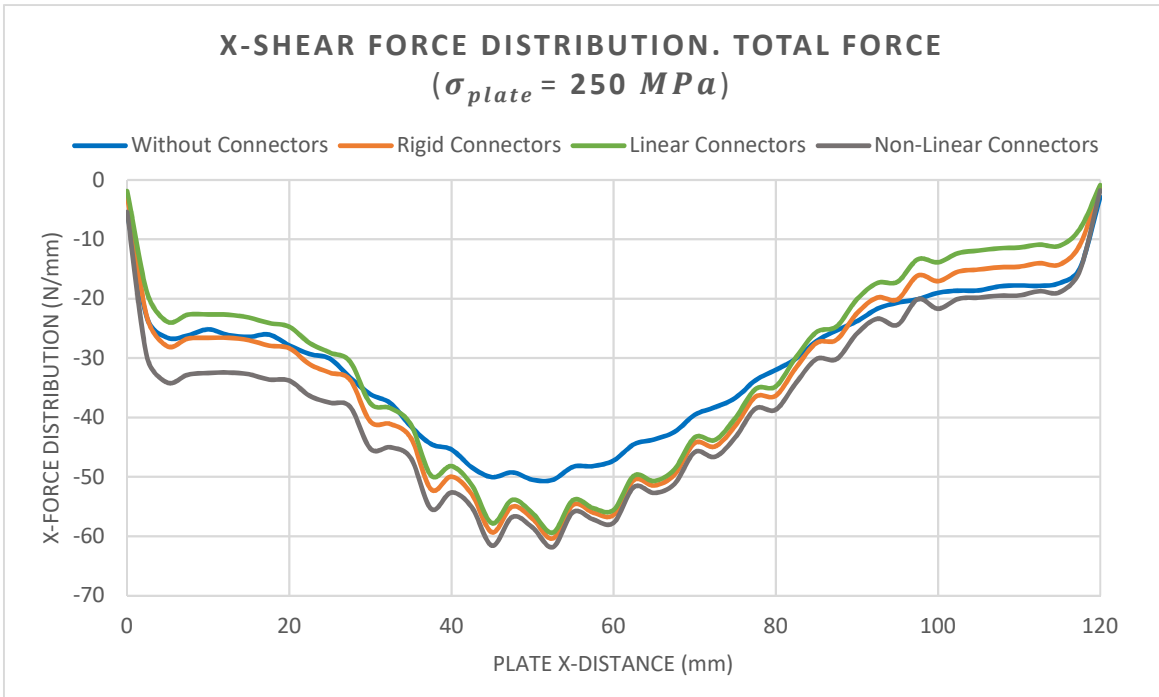
Figure 79. Comparison of X-shear force distribution between models with and without connectors. Friction Coeff.=0.3

- **SHEAR Y-FORCE DISTRIBUTION**

Figure 80. Comparison of Y-shear force distribution between models with and without connectors. Friction Coeff.=0.3

4.6.3. Friction Coefficient = 0.6

- **SHORTENING**

Figure 81. Shortening values comparison between models with and without connectors. Friction Coef.=0.6
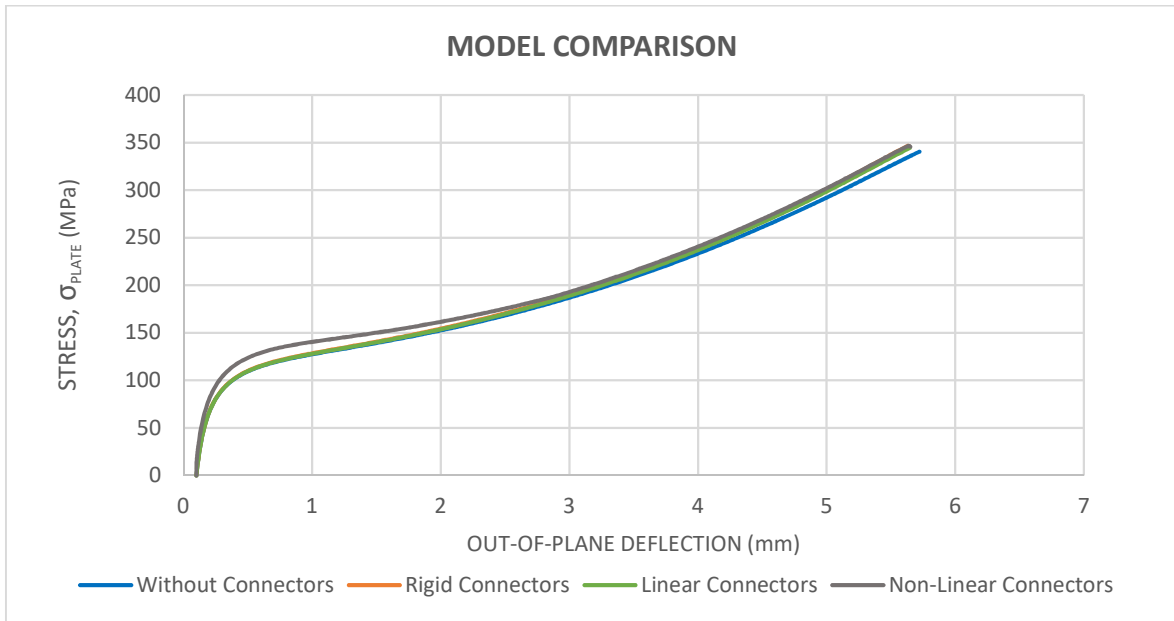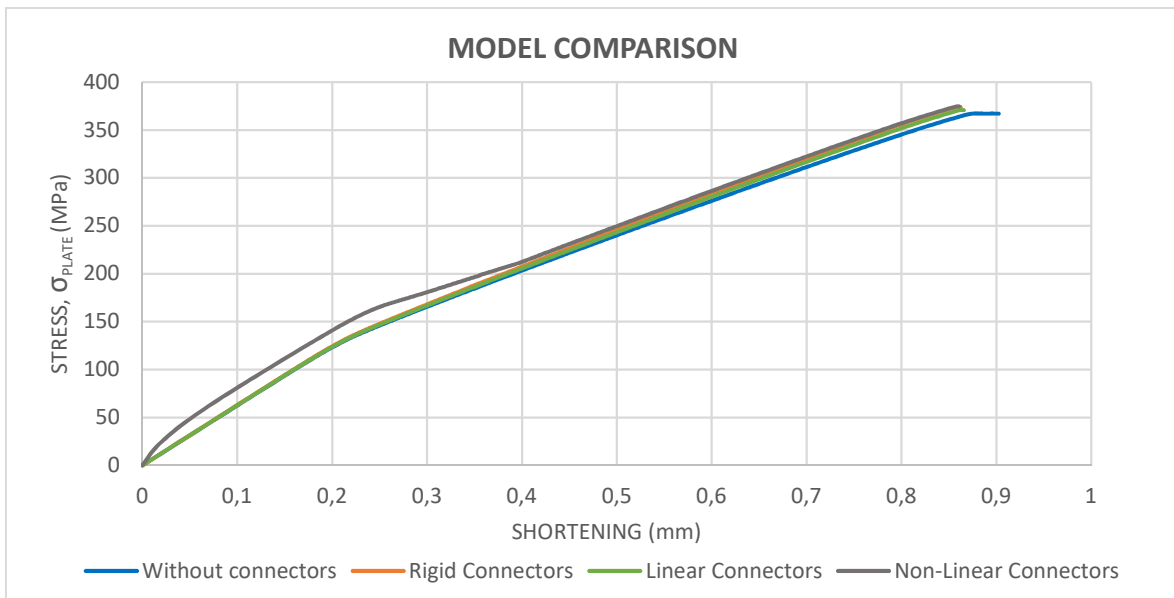
- **OUT OF PLANE DEFLECTION**
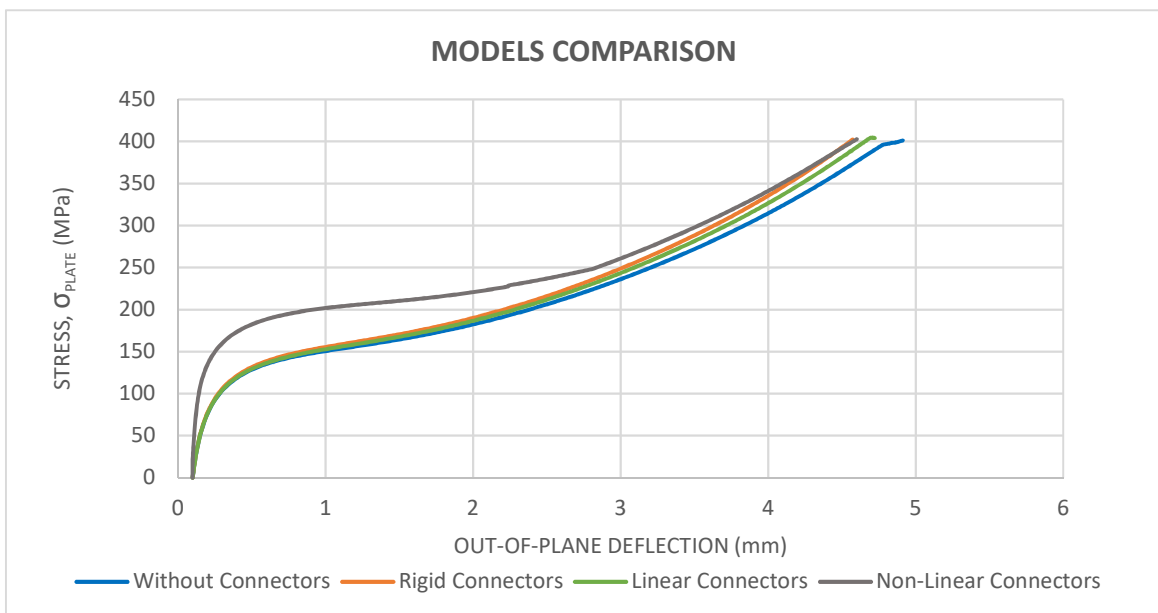
Figure 82. OoP values comparison between models with and without connectors. Friction Coef.=0.6

As it can be observed in the graphs above:
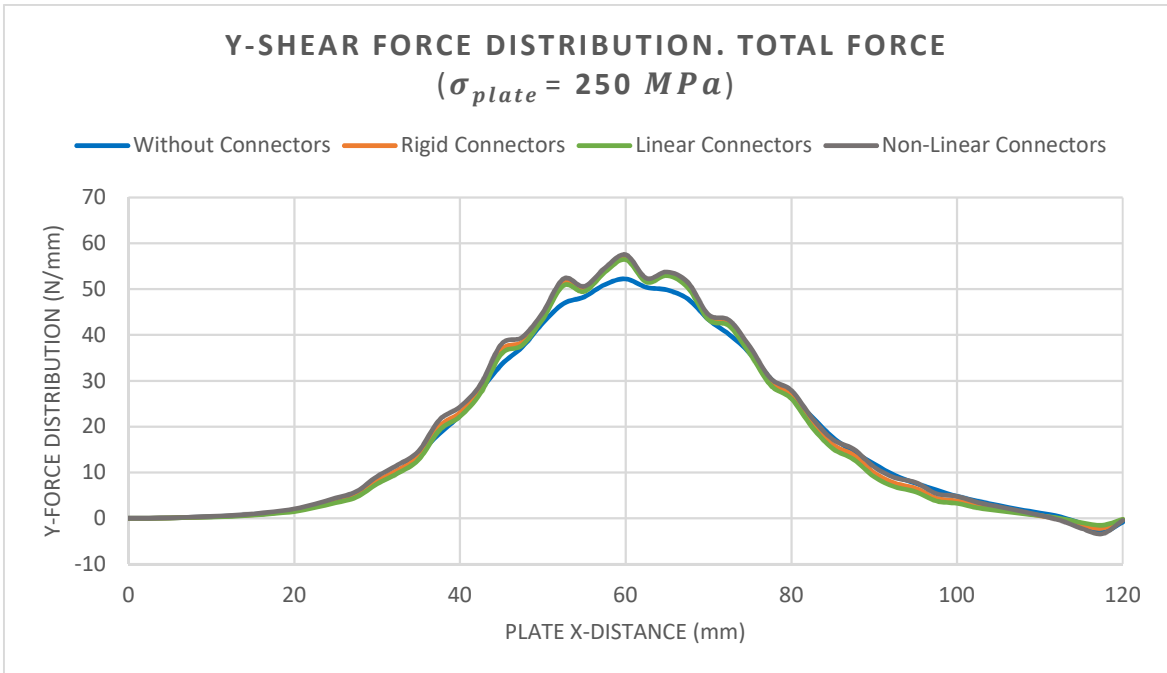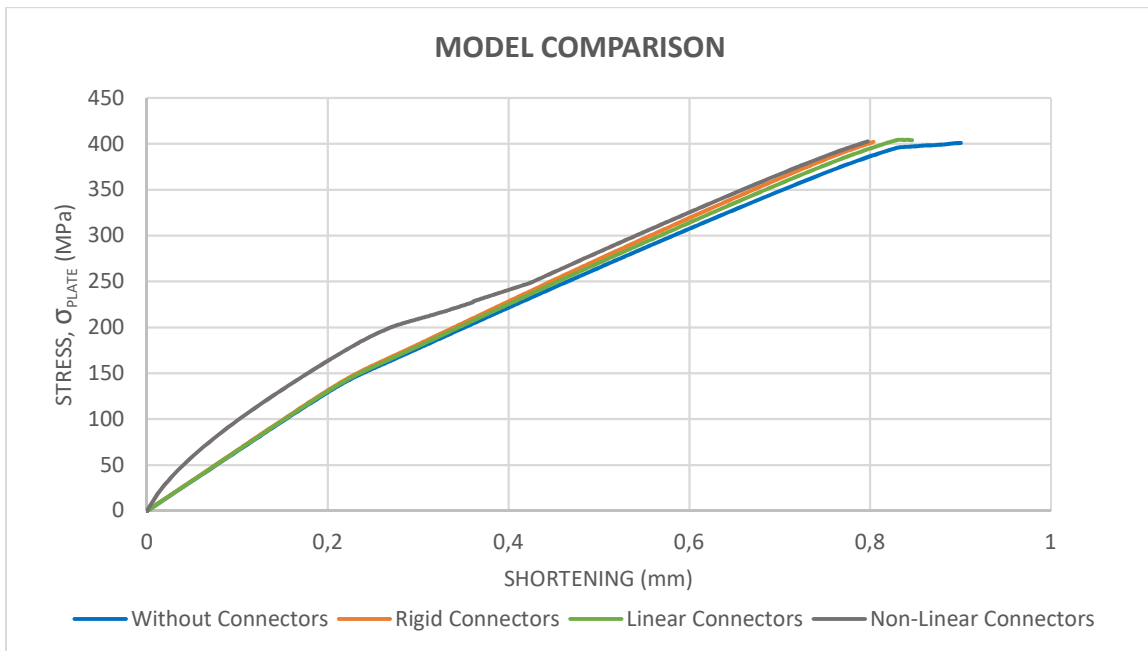
- Shortening and OoP deflection values from all the models follow the same tendendy, except for the Model 6.3 " Conectors with Non-Linear behavior" because they have a load applied before CAI test starts. Moreover, it is also noticed that this value variation rises when friction coefficient reaches a higher values (see *Figure 81* and *Figure 82* show).

- Normal distribution force is similar for Models 6.1, 6.2 and 6.3, in contrast to the model without connectors in its frame (it does not present stiffness in LSs-plate contact). In addition, notice that in *Figure 78*, the maximum force value is not reached in the middle of the plate, as it occurs in frictionless model (see *Figure 73*). In this case, maximum force value is located slightly in the upper part of the sample plate, which means 2 or 3 mm from its middle section.

- In the case of shear distribution force values, they also have the same behavior (with model without connectors in its frame reaching lower values than the other models). Finally, it is interesting to highlight that Model 6.3. has the higher value for X and Y shear forces but, this variation is not significant with regards to Models 5, 6.1 and 6.2. Therefore, FE-model verification has been shown.

5. Conclusion and future work

The goal of this thesis has been achieved reaching satisfactory results, described as follows:

- **2D plate modeled**

Mesh dependency was carried out with successful results and finally, a mesh composed by 1920 quads elements was adopted for 2D FE-models. In addition, theoretical buckling values from Classical Kirchhoff Shell Theory were also proved. With regards to the influence of the width plate for those models, parameters such as shortening, OoP deflection, uniaxial stress (σ_{11}), and failure stresses for plies 1 and 14 were analyzed. Failure stress value from Model 1 is lower than in the case of Model 2, and for this model (100 mm width), the first ply to present damage initiation corresponds to ply 14 (see *Table 15*).

However, it was not possible to find out how to create a contact between 2D surfaces along this thesis; therefore, there are no precise results of force distribution for 2D models.

- **3D plate modeled**

Thickness were applied to the sample plate. In this case (Model 4), FE-mesh is composed by elements 3D elements reaching higher value of stiffness. (see Failure stress values from *Table 16*). Once again, values variation between 2D and 3D plate model is not significantly high (less than 5%).

- **CAI Assembly modeled (LSs included)**

The most relevant study that was carried out in this subchapter was with regards to stablish a contact definition between sample plate and LSs from the CAI device frame. Conclude by LSs with sharp tip shape and ideal 3D plate model (Model 4) reach similar values in parameters such as shortening and OoP deflection as well as in failure stress. For this reason, sharp tip shape was adopted in order to carried out simulations from assembly models (Models 5, 6.1, 6.2 and 6.3)

- **Friction behavior**

Influence of friction behavior on the FE-model of the CAI device has been shown along subchapter 4.6. Shortening and OoP deflection values are higher when friction coefficient rises. Obviously, same occurs for shear forces (they depend directly on friction coefficient). In addition, it is interesting to mention that rupture is located slightly on the upper part of the sample plate (see Appendix).

For a future work, it would be important to consider the following points:

- Create a more accurate contact between in a 2D shell surface to improve FE-model verification process.

- Develop a CAD model of the new version of the framework from the CAI test device (not only LSs), which has been development in the lightweight laboratory at HAW. It would be is possible making several modifications in FE-model version already created, in order to predict experimental test results in a future.

References

[1]   Armstrong, K., Cole, W., & Bevan, G. (2005). Care and repair of advanced composites (pp. i-xxviii). SAE.

[2]   Giner, E.; Albelda, J. (2001). Análisis y diseño de materiales compuestos. Lecture notes. Universitat Politècnica de València.

[3]   Gholizadeh, S.(2018). A review of impact behavior in composite materials. Mechanical and Manufacturing Engineering Department. University Putra Malaysia.

[4]   Heimbs, S., Heller, S., & Middendorf, P. (2008, September). Simulation of low velocity impact on composite plates with compressive preload. In 7th German LS-DYNA Forum, Bamberg, Germany, September.

[5]   Li, Z., Haigh, A. D., Saleh, M. N., McCarthy, E. D., Soutis, C., Gibson, A. A., & Sloan, R. (2018). Detection of impact damage in carbon fiber composites using an electromagnetic sensor. Research in Nondestructive Evaluation, 29(3), 123-142.

[6]   American Society for Testing and Materials (Filadelfia). (2005). Standard test method for compressive residual strength properties of damaged polymer matrix composite plates. ASTM.

[7]   Flügge, F. Konstruktion und Validierung einer modifizierten Compression-After-Impact Prüfvorrichtung für dünnwandige Compositplatten. (2019). Master's Thesis. Hamburg University of Applied Sciences.

[8]   Linke, M., & García-Manrique, J. (2018). Contribution to Reduce the Influence of the Free Sliding Edge on Compression-After-Impact Testing of Thin-Walled Undamaged Composites Plates. Materials, 11(9), 1708.

[9]   Kersemans, M., Verboven, E., Segers, J., Hedayatrasa, S., & Paepegem, W. V. (2018). Non-Destructive Testing of Composites by Ultrasound, Local Defect Resonance and Thermography. In Multidisciplinary Digital Publishing Institute Proceedings (Vol. 2, No. 8, p. 554).

[10]   Olivares Ferrer, A. J. (2018). Finite element modeling of Compression After Impact test for laminated composite thin plates with initial delaminations. Master's Thesis. Hamburg University of Applied Sciences.

[11]   ABAQUS. Analysis User's Manual, Version 6.11, 2011

[12]   ABAQUS/CAE. User's Manual, Version 6.11, 2011

[13]   ABAQUS: Abaqus Keywords Reference Manual, Version 6.11, 2011

[14]   Sanchez-Saez, S., Barbero, E., Zaera, R., & Navarro, C. (2005). Compression after impact of thin composite laminates. Composites Science and Technology, 65(13), 1911-1919.

[15]   Jones, R. M. (2014). Mechanics of composite materials. CRC press.

[16]   Reddy, J. N. (2003). Mechanics of laminated composite plates and shells: theory and analysis. CRC press.

[17]   Sanga, R. P. L., Garnier, C., & Pantalé, O. (2016). Finite element simulation of low velocity impact damage on an aeronautical carbon composite structure. Applied Composite Materials, 23(6), 1195-1208.

[18]   Hashin, Z. (1980). Failure criteria for unidirectional fiber composites. Journal of applied mechanics, 47(2), 329-334.

[19]   Mendes, P. A. A. E., & Donadon, M. V. (2014). Numerical prediction of compression after impact behavior of woven composite laminates. Composite Structures, 113, 476-491.

[20]   Aymerich, F., & Priolo, P. (2008). Characterization of fracture modes in stitched and unstitched cross-ply laminates subjected to low-velocity impact and compression after impact loading. International Journal of Impact Engineering, 35(7), 591-608.

[21]   Abir, M. R., Tay, T. E., Ridha, M., & Lee, H. P. (2017). Modelling damage growth in composites subjected to impact and compression after impact. Composite Structures, 168, 13-25.

[22]   Bull, D. J., Helfen, L., Sinclair, I., Spearing, S. M., & Baumbach, T. (2013). A comparison of multi-scale 3D X-ray tomographic inspection techniques for assessing carbon fibre composite impact damage. Composites Science and Technology, 75, 55-61.

[23]   Gibson, R. F. (2016). Principles of composite material mechanics. CRC press.

[24]   Timoshenko, S. P., Gere, J. M., & Prager, W. (1962). Theory of elastic stability.

[25]   Airbus S.A.S. (2005) Airbus Test Method: Fibre Reinforced Plastics. Determination of Compression Strength after Impact; AITM1-0010. Blagnac, France.

[26]   Suppliers of Advance Composite Materials Association. (1988). SACMA recommended test method for compression after impact properties of oriented fiber-resin composites. SRM.

[27]   Sanchez-Saez, S., Barbero, E., Zaera, R., & Navarro, C. (2005). Compression after impact of thin composite laminates. Composites Science and Technology, 65(13), 1911-1919.

[28]   Liv, Y., Guillamet, G., Costa, J., González, E. V., Marín, L., & Mayugo, J. A. (2017). Experimental study into compression after impact strength of laminates with conventional and nonconventional ply orientations. Composites Part B: Engineering, 126, 133-142.

[29]   Turon Travesa, A. (2006). Simulation of delamination in composites under quasi-static and fatigue loading using cohesive zone models. Universitat de Girona.

[30]   Cook, R. D. (2007). Concepts and applications of finite element analysis. John Wiley & Sons.

[31]   Wang, Y., & Huang, Z. (2018). Analytical micromechanics models for elastoplastic behavior of long fibrous composites: A critical review and comparative study. Materials, 11(10), 1919.

[32]   AWARE, W. T. A., & DOCUMENTATION, T. P. S. (2009). Carbon-fibre-reinforced plastics—Determination of compression-after-impact properties at a specified impact-energy level.

[33]   Aerospace series (2015). Fibre reinforced plastics - Test method – "Determination of the compression strength after impact" standard, Aerospace and Defence Industries Association of Europe - Standardization (ASD-STAN).

[34]   Deutsches Institut für Normung (1989). Luft- und Raumfahrt. Faserverstärkte Kunststoffe. Prüfung von multidirektionalen Laminaten. Bestimmung der Druckfestigkeit nach Schlagbeanspruchung, standard.

[35]   Zwick / Roell GmbH & Co. KG (2018). Search online: https://www.zwick.de/-/media/files/sharepoint/vertriebsdoku_pi/10_805_cai-vorrichtungen_pi_d.pdf, Seitenzugriff.

[36]   Instron GmbH (2018). Search online: http://www.instron.de/de-de/testing-solutions/by-test-type/compression/aitm-airbus-test-method, Seitenzugriff.

[37]   Williams, A. John; Dwyer-Joyce, S. Rob. (1985). Contact between solid surfaces. Cambridge University Press and University of Sheffield, 1985

[38]   Coulomb, C. A. (1821). Theorie des machines simple (Theory of simple machines). Bachelier, Paris.

[39]   Vnučec, Z. (2005, January). Analysis of the laminated composite plate under combined loads. In RIM 2005: 5th International Scientific Conference on Production Engineering.

[40]   Sun, J. S., Lee, K. H., & Lee, H. P. (2000). Comparison of implicit and explicit finite element methods for dynamic problems. Journal of Materials Processing Technology, 105(1-2), 110-118.

[41]   Bolotin, V. V. (1996). Delaminations in composite structures: its origin, buckling, growth and stability. Composites Part B: Engineering, 27(2), 129-145.

[42]   The Boeing Company. (1988). Advanced Composite Compression Test. Standard, Seattle, WA.

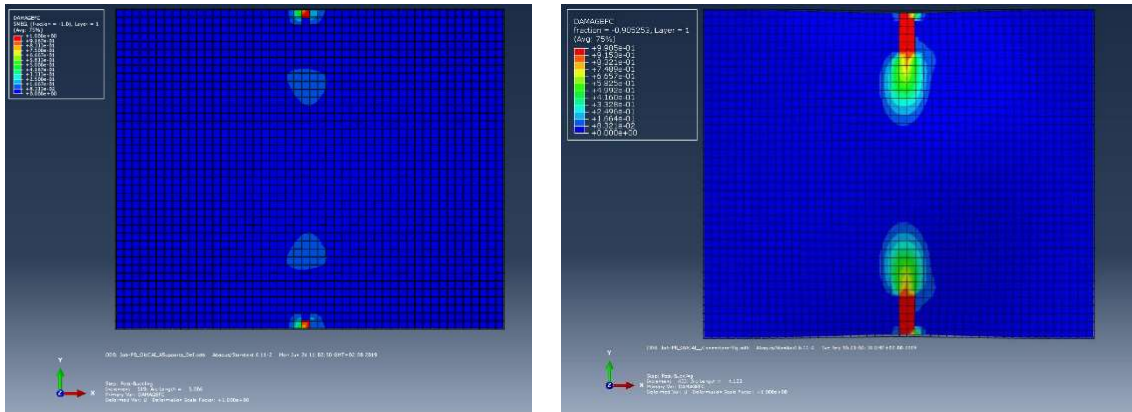# Appendix

- **FRICTIONLESS**

Figure 83. Damage plate developed. Model 4 (left) and Model 6.1. (right). Frictionless behavior
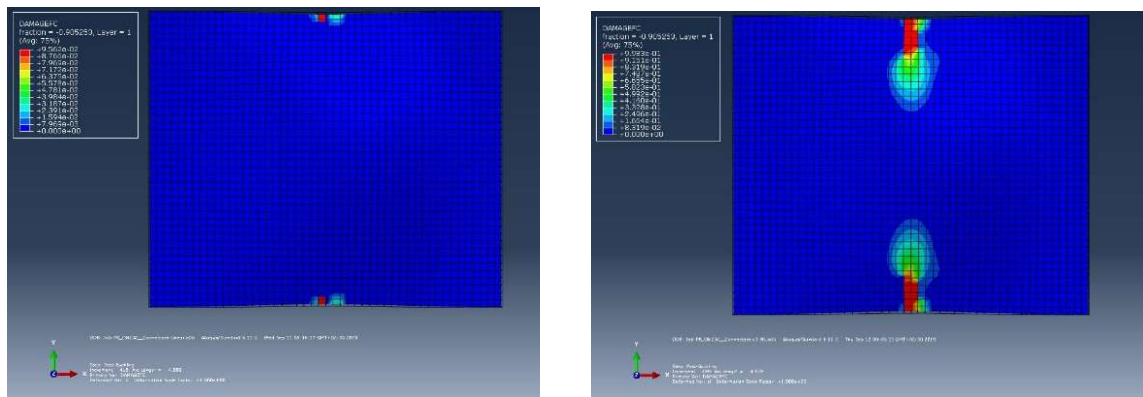

Figure 84. Damage plate developed. Model 6.2 (left) and Model 6.3 (right). Frictionless behavior
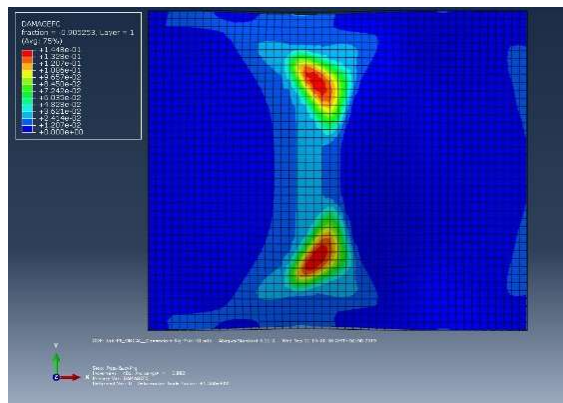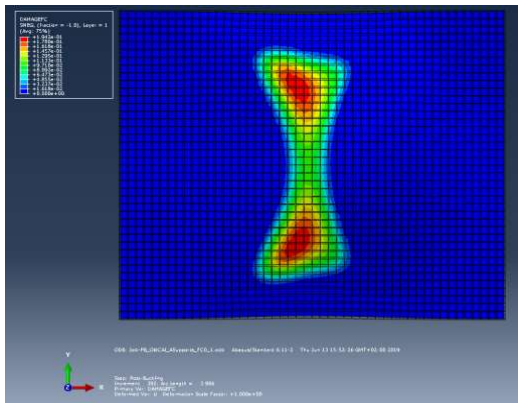
- **FRICTION COEFFICIENT = 0.1**

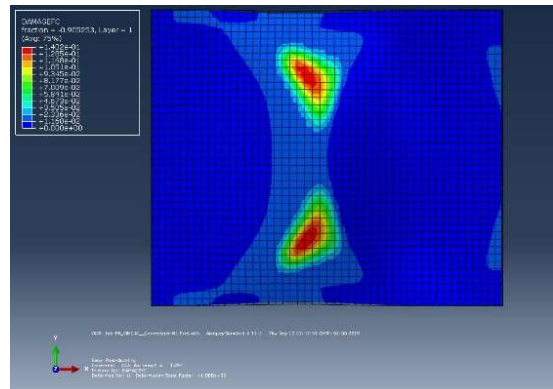*Figure 85. Damage plate developed. Model 4 (left) and Model 6.1. (right). With µ = 0.1*

Figure 86. Damage plate developed. Model 6.2. (left) and Model 6.3. (right). With µ = 0.1

- **FRICTION COEFFICIENT = 0.3**

Figure 87. Damage plate developed. Model 4 (left) and Model 6.1. (right). With µ = 0.3

Figure 88. Damage plate developed. Model 6.2. (left) and Model 6.3. (right). With µ = 0.3

- **FRICTION COEFFICIENT = 0.6**

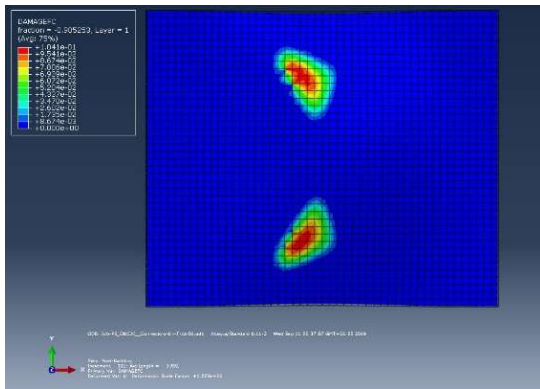*Figure 89. Damage plate developed. Model 4 (left) and Model 6.1. (right). With µ = 0.6*

Figure 90. Damage plate developed. Model 6.2. (left) and Model 6.3. (right). With µ = 0.6